BEAMING AND LOCALIZATION OF ELECTROMAGNETIC WAVES IN PERIODIC STRUCTURES

A DISSERTATION
SUBMITTED TO THE DEPARTMENT OF PHYSICS
AND THE INSTITUTE OF ENGINEERING AND SCIENCE
OF BILKENT UNIVERSITY
IN PARTIAL FULFILLMENT OF THE REQUIREMENTS
FOR THE DEGREE OF
DOCTOR OF PHILOSOPHY

By

Hümeyra Çağlayan

June, 2010

I certify that I have read this thesis and that in my opinion it is fully adequate, in scope and in quality, as a dissertation for the degree of Doctor of Philosophy.

_____

Prof. Dr. Ekmel Özbay (Supervisor)

I certify that I have read this thesis and that in my opinion it is fully adequate, in scope and in quality, as a dissertation for the degree of Doctor of Philosophy.

_____

Prof. Dr. Atilla Erçelebi

I certify that I have read this thesis and that in my opinion it is fully adequate, in scope and in quality, as a dissertation for the degree of Doctor of Philosophy.

_____

Assoc. Prof. Dr. Ceyhun Bulutay

I certify that I have read this thesis and that in my opinion it is fully adequate, in scope and in quality, as a dissertation for the degree of Doctor of Philosophy.

_____

Assoc. Prof. Dr. Vakur B. Ertürk

I certify that I have read this thesis and that in my opinion it is fully adequate, in scope and in quality, as a dissertation for the degree of Doctor of Philosophy.

_____

Assist. Prof. Dr. Hamza Kurt

Approved for the Institute of Engineering and Science:

_____

Prof. Dr. Mehmet Baray,
Director of the Institute of Engineering and Science

ABSTRACT

BEAMING AND LOCALIZATION OF ELECTROMAGNETIC WAVES IN PERIODIC STRUCTURES

Hümeyra Çağlayan
PhD in Physics
Supervisor: Prof. Dr. Ekmel Özbay
June, 2010

We want to manipulate light for several applications: microscopy, data storage, leds, lasers, modulators, sensor and solarcells to make our life healthier, easier or more comfortable. However, especially in small scales manipulating light have many difficulties. We could not focus or localize light into subwavelength dimensions easily, which is the key solution to beat today's devices both in performance and cost. Achievements in three key research fields may provide the answer to these problems. These emerging research fields are metamaterials, photonic crystals and surface plasmons. In this thesis, we investigated beaming and localization of electromagnetic waves in periodic structures such as: subwavelength metallic gratings, photonic crystals and metamaterials. We studied off-axis beaming from both a metallic subwavelength aperture and photonic crystal waveguide at microwave regime. The output surfaces are designed asymmetrically to change the beaming angle. Furthermore, we studied frequency dependent beam steering with a photonic crystal with a surface defect layer made of dimmers. The dispersion diagram reveals that the dimer-layer supports a surface mode with negative slope. Thus, a photonic crystal based surface wave structure that acts as a frequency dependent leaky wave antenna was presented. Additionally, we investigated metamaterial based cavity systems. Since the unit cells of

metamaterials are much smaller than the operation wavelength, we observed subwavelength localization within these metamaterial cavity structures. Moreover, we introduced coupled-cavity structures and presented the transmission spectrum of metamaterial based coupled-cavity structures. Finally, we demonstrated an ultrafast bioassay preparation method that overcomes the today's bioassay limitations using a combination of low power microwave heating and split ring resonator structures.

***Keywords**:* Surface Plasmons, Off-Axis Beaming, Photonic Crystal, Surface Mode, Beam Steering, Backward Leaky Wave, Metamaterial, Split Ring Resonator, Composite Metamaterial, Negative Permittivity, Negative Permeability, Metamaterial based Cavity, Subwavelength Localization, Ultrafast Bioassay.

ÖZET

PERİYODİK YAPILARDA ELEKTROMAGNETİK DALGALARIN YÖNLENDİRİLMESİ VE LOKALİZASYONU

Hümeyra Çağlayan
Fizik, Doktora
Tez Yöneticisi: Prof. Dr. Ekmel Özbay
Haziran 2010

Hayatımızı daha kolay, konforlu ve sıhhatli yapmak için mikroskop, veri saklama, LED, lazer, modulator, sensor ve güneş pilleri gibi çok çeşitleri araçlarda elektromanyetik dalgaların isteğimize uygun biçimde yönlendirmek istiyoruz. Fakat, özellikle çok küçük boyutlarda elektromanyetik dalgaları isteğimize uygun şekilde yönlendirmek çok zordur. Bugünkü kullandığımız pek çok cihazı performans ve maliyet açısından daha iyileriyle değiştirmek içinse gerekli olan en önemli çözüm olan elektromanyetik dalgaları dalgaboyu-altı boyutta odaklamak ve yönlendirmektir işlemini kolayca yapamıyoruz. Üç önemli çalışma alanlarındaki başarılar bu soruna çözüm olabilir. Bu gelişmekte olan çalışma alanları: metamalzemeler, fotonik kristallar ve yüzey plazmonlarıdır. Bu tezde, dalgaboyu-altı metalik ızgaralı yapılar, fotonik kristaller ve metamalzemeler gibi periyodik yapılarda elektroanyetik dalgaların yönlendirilmesi ve lokalizasyonu incelendi. Hem metalik dagaboyu-altı yapıları hem de fotonik kristaldalga kılavuzu ile eksenden sapmış yönledirme mikrodalga boyutunda araştırıldı. Çıkış yüzeyi yönlendirme açısını değiştirmek amacıyla asimetrik olarak tasarlandı. Ayrıca, yüzey yapısı değiştirilmiş fotonik kristal yapıları ile frekansa bağlı yönlendirme çalışıldı. Dispersiyon diyagramı ile değiştirilmiş olan yüzey yapısının negatif

eğime sahip yüzey modu ortaya çıkarıldı. Bu nedenle, fotonik kristal bazlı yüzey dalgaları ile frekansa bağlı sızan dalga antenlerinin çalışma sisteminin aynı olduğu gösterildi. Bütün bunlara ek olarak, metamalzeme bazlı kavite yapıları araştırıldı. Metamazelme yapılarının birim hücreleri çalışma dalga boyundan çok küçük olduğu için, dalgaboyu-altı lokalizasyon gözlendi. Ayrıca bağlı-kavite yapıları incelendi. Son olarak, günümüzde kullanılan biyolojik tahlil metodlarının limitlerini aşabilen çok hızlı biyolojik tahlil metodu düşük güçlü mikrodalga ısınma ve yarıklı halka rezönatötleri kullanılarak gösterildi.

Anahtar Kelimeler: Yüzey Plazmonları, Eksenden sapmış yönlendirme, Fotonik Kristal, Yüzey Modu, Işın yönlendirme, Ters sızan dalga, Metamalzeme, Yarıklı halka rezonatörü, Kompozit Metamalzeme, Negatif Permeabilite, Negatif Permitivite, Metamalzeme bazlı Kavite, Dalgaboyu-altı lokalizasyon, Çok hızlı Biyolojik tahlil.

Acknowledgements

It is my pleasure to express my deepest gratitude and respect to Prof. Dr. Ekmel Ozbay for his invaluable guidance, helpful suggestions and endless support. His personal and academic virtue shaped my academic personality and changed my approach to scientific study.

I would like to thank to the members of my thesis committee, Prof. Dr. Atilla Erçelebi, Assoc. Prof. Dr. Ceyhun Bulutay, Assoc. Prof. Dr. Vakur B. Ertürk, and Assit. Prof. Dr. Hamza Kurt, for reading the manuscript and commenting on the thesis.

I would like to express my special thanks and gratitude to Dr. İrfan Bulu for his continues support, encouragement and valuable ideas towards the realization of this thesis work.

I am very fortunate to have been a member of the Özbay group. This thesis would never been succesful with the endless help of the Özbay group members. I had a chance to collaborate with Dr. Koray Aydın, Evrim Çolak, Atilla Özgür Çakmak, Dr. Zhaofeng Li, Kamil Boratay Alıcı and Semih Çakmakyapan. Indeed, all of the people with whom I've overlapped in the Özbay group have contributed to my academic life. Thank you all.

I would like to thank the members of Nanotechnology Research Center and Advanced Research Laboratory for making my life easier. I am also thankful to my professors and friends in the Department of Physics.

I am grateful to all of our collaborators for sharing our enthusiasm for the projects, and giving their time and best effort to contribute to our joint work.

I would also like to thank my close friend Evren Karakaya for her help, understanding and friendship.

Special thanks go to my mom, father and sisters for their love, encouragement and care. I cannot imagine finishing all my achievements without their endless moral support.

Finally, thanks to my husband and to my son, **Engin Yahya**, for shining a different color onto my life. I dedicate this labor to my mom and my son.

Contents

List of Figures

List of Tables

Chapter 1

Introduction

Electronic circuits provide us the ability to control the transport and storage of electrons. However, the performance of electronic circuits is now becoming rather limited when digital information needs to be sent from one point to another. Photonics offers an effective solution to this problem. Hence, we need to manipulate light for several photonic applications including communication, imaging, sensing and devices like microscopy, data storage, leds, lasers, modulators, sensor, solarcells, etc to make our life healthier, easier or more comfortable. However, especially in small scales, manipulating electromagnetic waves has many difficulties. We could not focus or localize light into subwavelength dimensions easily, which is the key solution to beat today's devices both in performance and cost. Three research fields are attracting a great deal of attention in these recent years: photonic crystals, metamaterials and surface plasmon phenomenon. The basic reason behind this interest is the fact that these structures provide means to control the propagation of electromagnetic waves.

Photonic crystals are usually viewed as an optical analog of semiconductors that modify the properties of light similarly to a microscopic atomic lattice that creates a semiconductor bandgap for electrons [1]. One of the most promising applications of photonic crystals is the possibility of creating

compact integrated optical devices, [2, 3] which would be analogous to the integrated circuits in electronics but would operate entirely with light. Replacing relatively slow electrons with photons as the carriers of information can dramatically increase the speed and the bandwidth of advanced communication systems, thus revolutionizing the telecommunication industry.

Surface plasmons are waves that propagate along the surface of a conductor. These are essentially light waves that are trapped on the surface because of their interaction with the free electrons of the conductor. In this interaction, the free electrons respond collectively by oscillating in resonance with the lightwave. The resonant interaction between the surface charge oscillation and the electromagnetic field of the light constitutes the surface plasmon and gives rise to its unique
properties [4-6].

Surface plasmons are of interest to a wide class of scientists, ranging from physicists to chemists, from material scientists to biologists. Increased interest in surface plasmons stems from the recent advances that allow metals to be structured and characterized at nanometer scale. This enables us to control the surface plasmon properties in order to study the new aspects of their science and use them for specific applications. For instance, surface plasmons are currently being explored for their potential in optics [6], magneto-optic data storage [7], microscopy [8] and solar cells [9], as well as being used to construct sensors for detecting biologically interesting molecules [10]. For researchers in the field of optics, one of the most attractive aspects of surface plasmons is the way in which they help us to concentrate and channel light using subwavelength structures.

On the other hand, the field of metamaterials is a relatively new research area; however, it is attracting a great deal of attention. The fundamental reason for this interest in metamaterials is that these structures can be designed to have permittivities and permeabilities with almost any values including negative ones. Ordinary materials usually have positive values of permittivity and permeability.

The response from the ordinary materials is only a small fraction that one can access theoretically. Material responses could be extended to the values that are not readily available by designing artificial structures, so called metamaterials. The phrase “Meta” is borrowed from Greek meaning “beyond”. This possibility of negative permittivities and permeabilities leads to some exciting conclusions such as the negative refraction, inverse Doppler shift, Cerenkov radiation and many more. In addition, the ability to design a medium with desired permittivity and permeability values leads to some interesting applications such as superlens [11], (b) magnifying hyperlens [12], (c) cloaking device [13].

In this thesis, we investigate beaming and localization of electromagnetic waves in periodic structures such as: subwavelength metallic gratings, photonic crystals and metamaterials. Although this thesis is based on the experimental measurements, numerical simulations are also utilized to understand the physical mechanisms and to verify the measured results.

In chapter 2, off-axis directional beaming from subwavelength aperture with metallic gratings is studied. We changed the periods of the grooves on different sides of the aperture. One of the sides has a smaller period while the other side has a longer period than the input side. Moreover, we investigated the origin of the off-axis beaming by simulating 3 different cases with different output grating periods.

In chapter 3, we used the similarity between a photonic crystal and a metallic grating structure. We investigated theoretically and experimentally the possibility of off-axis beaming from Photonic Crystal waveguide using asymmetric periodic surface layer.

In chapter 4, we studied frequency dependent beam steering with a PC with a surface defect layer made of dimmers. The dispersion diagram was obtained with the Plane Wave Expansion Method. The dispersion diagram reveals that the dimer-layer supports a surface mode with negative slope. Thus, a Photonic Crystal based surface wave structure that acts as a frequency dependent leaky wave antenna was

presented. Finally, the backward radiation characteristics that in turn suggest the existence of a backward leaky mode in the dimer-layer were experimentally verified.

Chapter 5 is devoted to metamaterial based cavities. First of all, we introduce a cavity to the split ring resonator and composite metamaterial systems. Since the unit cells of metamaterials are much smaller than the operation wavelength, we investigate the possibility of the subwavelength localization within these metamaterial cavity structures. Subsequently, in taking full advantage of the effective medium theory, we modeled composite metamaterial based cavities as one dimensional Fabry-Perot resonators with a subwavelength cavity at the center. We calculated the transmission from the Fabry-Perot resonator model using the one dimensional transfer matrix method. Moreover, we introduced coupled-cavity structures and presented the transmission spectrum of split ring resonator and composite metamaterial based coupled-cavity structures. The dispersion relation and normalized group velocity of the coupled-cavity structures were calculated.

In chapter 6, we report an ultrafast bioassay preparation method that overcomes the today's bioassay limitations using a combination of low power microwave heating and split ring resonator structures. The proof-of-principle demonstration of the ultrafast bioassays was accomplished by using a model biotin-avidin bioassay.

Finally, chapter 7 summarizes the achievements in the thesis.

Chapter 2

Off-Axis beaming from metallic gratings

2.1. Introduction

The transmission of electromagnetic (EM) waves through a single subwavelength aperture has been studied for many years. As defined in the standard diffraction theory by Bethe [14] in 1944, EM waves that transmit through a subwavelength aperture are fully diffracted in all directions. This disadvantage is the main problem in controlling light. Hence, there are many studies aimed at solving this problem. In 2002, Lezec *et al*. [15] showed that it is possible to obtain directional beaming from subwavelength apertures via the excitation of surface plasmons (SPs) on corrugated metallic surfaces. Since the reporting of directional beaming through subwavelength apertures, this phenomenon has been intensively researched in the theoretical and experimental aspects [16-21]. Control of directional beaming is not limited to metallic gratings and there are several research activities on the beaming of light using photonic crystals [22-24]. However, all of these studies specifically investigated on-axis beaming.

Changing the beaming angle is another important issue. Therefore, only if we can control both the beaming and beaming angle can we in turn fully solve the problem of diffraction from a subwavelength aperture. Recently, Kim *et al.* [25] proposed a method for changing the beaming angle, and Lin *et al.* [26] showed that it is possible to obtain off-axis directional beaming at optical frequencies using asymmetric dielectric gratings. However, to our knowledge, there has not been any scientific work that demonstrates off-axis directional beaming by using metallic gratings in the microwave regime.

In this chapter, we investigate the steering of beaming via a subwavelength metallic aperture with asymmetric surface gratings. By using this new structure, we were able to change the beaming angle and attain off-axis directional beaming.

2.2. Surface Plasmon Polaritons

A polariton is an EM mode related to the oscillation of polarization charge density. At the interface between two media with frequency dependent complex dielectric functions ε_1 and ε_2, surface polaritons with EM field exponentially decaying into both media may occur according to the well-known dispersion relation:

$$k_{sp} = (\omega/c)\sqrt{(\varepsilon_1\varepsilon_2)/(\varepsilon_1 + \varepsilon_2)} \tag{2.1}$$

(where k_{sp}, ω and c are respectively the in-plane wave-vector of the surface polariton, the angular frequency and the speed of light) provided the real part of the dielectric functions in the two media are of opposite sign. If the material with the negative real part dielectric function is a metal, the polarization charge density oscillation corresponds to the oscillation of the electron gas, and then the surface polariton is called a Surface Plasmon Polariton (SPP) [5, 6, 27, 28].

SPPs are quasi-two-dimensional EM excitations, propagating along a dielectric-metal interface and having the field components decaying exponentially into both neighboring media. The field of a plane SPP comprises a magnetic field component, which is parallel to the interface plane and perpendicular to the SPP

propagation direction, and two electric field components, of which the main one is perpendicular to the interface (Fig. 2.1). SPPs can be tightly bound to the metal surface, penetrating on the order of 100 nm into the dielectric and ~10 nm into the metal. This feature implies the possibility of using SPPs for miniature photonic circuits and optical interconnects and has attracted a great deal of attention to SPPs.

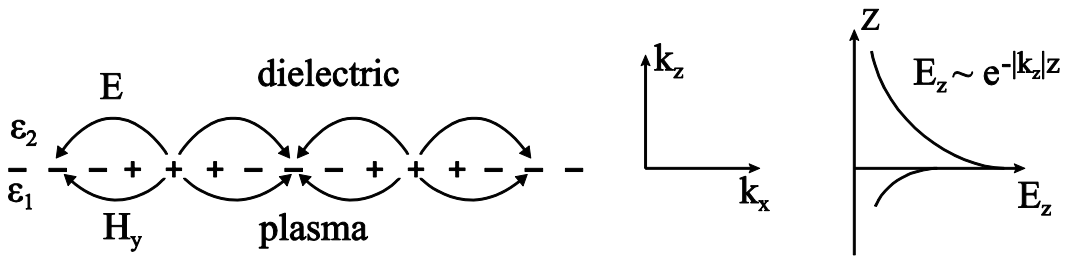

Figure 2.1: The charges and the EM field of SPs propagating on a surface in the x direction are shown schematically. The exponential dependence of the field E_z is seen on the right. H_y shows the magnetic field in the y direction of the p-polarized wave.

In recent years, we have witnessed a flurry of activity in the fundamental research and development of SP based structures and devices. They can take various forms, ranging from freely propagating electron density waves along metal surfaces to localized electron oscillations on metal nanoparticles. Their unique properties enable a wide range of practical applications, including light guiding and manipulation at the nanoscale, biodetection at the single molecule level, enhanced optical transmission through subwavelength apertures, and high resolution optical imaging below the diffraction limit.

For the visible region, the degree of trapping of the mode at the metal surface and the usefulness of the SP depend strongly on the metal used. However, at microwave wavelengths, metals have skin depth approaching to zero and thus behave as perfect electric conductor. All metals may be treated as almost perfect

conductors that completely screen out the EM field. Perfect electric conductors do not support SPs anyhow.

Recently John Pendry and his coworkers proposed that, "Although a flat perfectly conducting surface supports no bound states, the presence of holes, however small, produces a surface-plasmon polariton-like bound surface state." The existence of SPs at corrugated perfect metal surfaces is due to the corrugation, and therefore, they are frequently referred to as "spoof" SPs or "designer" SPs [29]. The ability to design even perfect conducting surfaces with specific spoof SP properties essentially means that one can design, in any metal, a particular response dictated not by the choice of metal but by the specific patterning chosen [30].

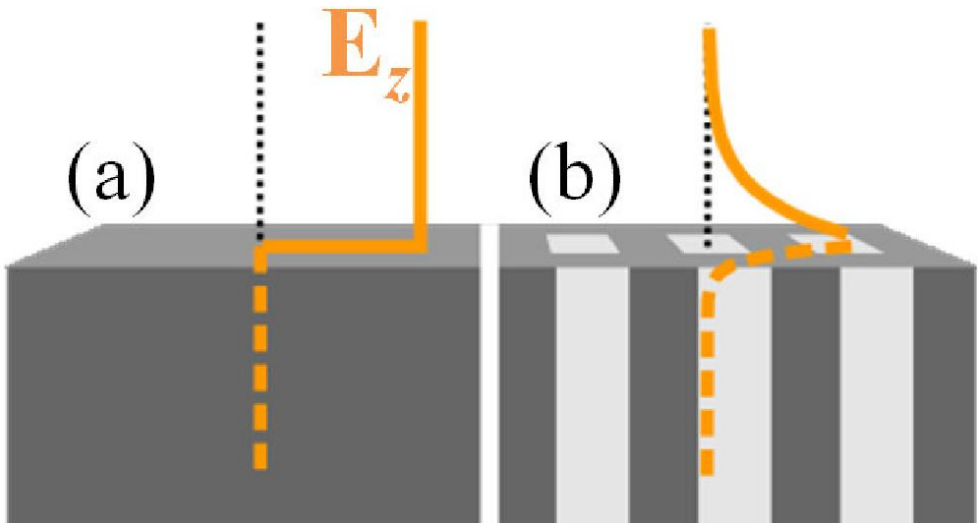

Figure 2.2: Schematic representation of electric fields associated with a mode propagating along the surface of a metal. (a) At microwave frequencies, the metal is almost perfectly conducting and the field (E_z) extends far beyond the metal. (b) By perforating the substrate with an array of subwavelength holes, the field is localized near the interface.

2.3. Directional beaming from a subwavelength metallic aperture

SPs are well known for their capabilities of concentrating light in subwavelength volumes and also for guiding light along the surface of a metal. But this does not exhaust the phenomena related to SPs. Even the scientific community working on this subject was greatly surprised in 1998 by the suggestion that SPs could enhance the transmission of light through subwavelength holes [31]. That seminal paper reported that, when subwavelength holes are disposed on a metallic film forming a two-dimensional (2D) array, the transmission of light through this structure is greatly enhanced at some particular wavelengths. The locations of the transmission peaks appearing in the experimental spectra could be approximately found from the dispersion relation of SPs modes running on the metal surface. Then, from the beginning of the history of this subject, it was clear that there was a close connection between extraordinary optical transmission (EOT) and the excitation of SPs. Since 1998, several experimental and theoretical groups around the world have reproduced the main features found in the first set of experiments. The dependence of this phenomenon with the type of metal (noble metals show larger enhancements), type of lattice (square or triangular), shape of the holes (circular, elliptical, square or rectangular) and frequency regime (optical, THz or microwave) have been thoroughly analyzed [32-40]. Four years after the discovery of EOT in 2D hole arrays, it was also reported that EOT phenomenon also appears in a single aperture (hole or slit) flanked by periodic corrugations in the side of the metal film the light is impinging on [15].

Moreover, it was also found that very strong directional emission (beaming) is possible through single apertures if the corrugation is placed on the exit side. In this section, we investigate the directional beaming from a subwavelength aperture at microwave frequencies.

For directional beaming measurements we designed two structures: 1) the reference sample (a metal plate with a subwavelength slit in it), 2) a subwavelength slit surrounded by periodic gratings as shown in Fig. 2.3. These samples were metallic and made of aluminum (Al). The samples were fabricated using a CNC machine with a process resolution of 0.1 mm. Slit width was 2 mm. Metal thickness is defined as the thickness that light passes through, which is 8 mm. Period of the grating was 16 mm, groove depth was 4 mm.

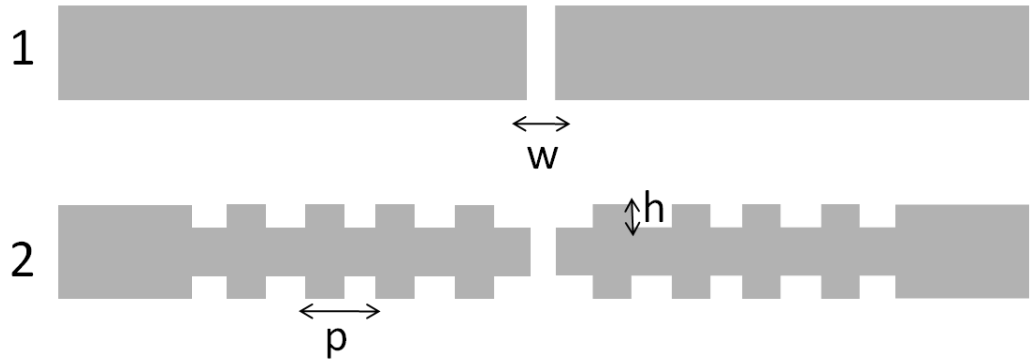

Figure 2.3: (a) The reference sample (a metal plate with a subwavelength slit in it), (b) a subwavelength slit surrounded by periodic gratings where w=2 mm, h=4 mm and p= 16 mm.

According to the coupling formula:

$$k_{sp} \pm N k_g = k_o sin\theta \tag{2.2}$$

where $k_g = 2\pi/\lambda_g$, period of the grating is important in coupling. It should not be greater or smaller than our study range (8mm-30mm). We chose 16 mm for grating periodicity (λ_g). According to the previous studies by grating structures [41] deeper groove depths (h) for grating produce better results.

2.3.1. Simulation

Theoretical calculations were done using the finite-difference-time-domain (FDTD) method-based simulations. FDTD is a direct space-time approach. The basic algorithm of FDTD method depends on Maxwell's equations. When Maxwell's differential form equations are examined, it can be seen that the time derivative of the E field is dependent on the Curl of the H field. Thus, the change in the E field (the time derivative) is dependent on the change in the H field across space (the Curl). This results in the basic FDTD equation that the new value of the E field is dependent on the old value of the E field (hence the difference in time) and the difference in the old value of the H field on either side of the E field point in space. The H field is found in the same manner. The new value of the H field is dependent on the old value of the H field (hence the difference in time), as well as dependent on the difference in the E field on either side of the H field point.

In this method, an oscillating wave source is introduced into the grid and "directed" at the structure to be analyzed. The entire grid is then time-stepped until steady state response oscillations are obtained at all points on the grid. In order to use FDTD, a computational domain where the simulation will be performed must be established. The E and H fields will be determined at every point within the computational domain. The material (air, metal or dielectric) of each cell within the computational domain must be specified. Once the computational domain and the grid material are established, a source is specified. It is suitable to introduce a Gaussian pulse, to calculate the spectral response.

Since the E and H fields are determined directly, the output of the simulation is usually the E or H field at a point or a series of points within the computational domain.

To define structures, permittivity should be specified. Permittivity of free-space (air) is 1. The permittivity of metal depends on the frequency of the incident radiation. So, we modeled our structure by using the Drude dispersion model,

which is one of the models to determine the frequency dependent permittivity of metals. Drude model assumes that, all of the conduction electrons can freely move around inside the metal to form a gas of non-interacting particles. The permittivity is given by the relation:

$$\varepsilon(\omega) = 1 - \frac{\omega_p^2}{\omega(\omega - i\omega_\tau)} \tag{2.3}$$

where ω_p=3570 THz is the plasma frequency, and ω_τ=19.4 THz is the absorption coefficient for aluminum [42].

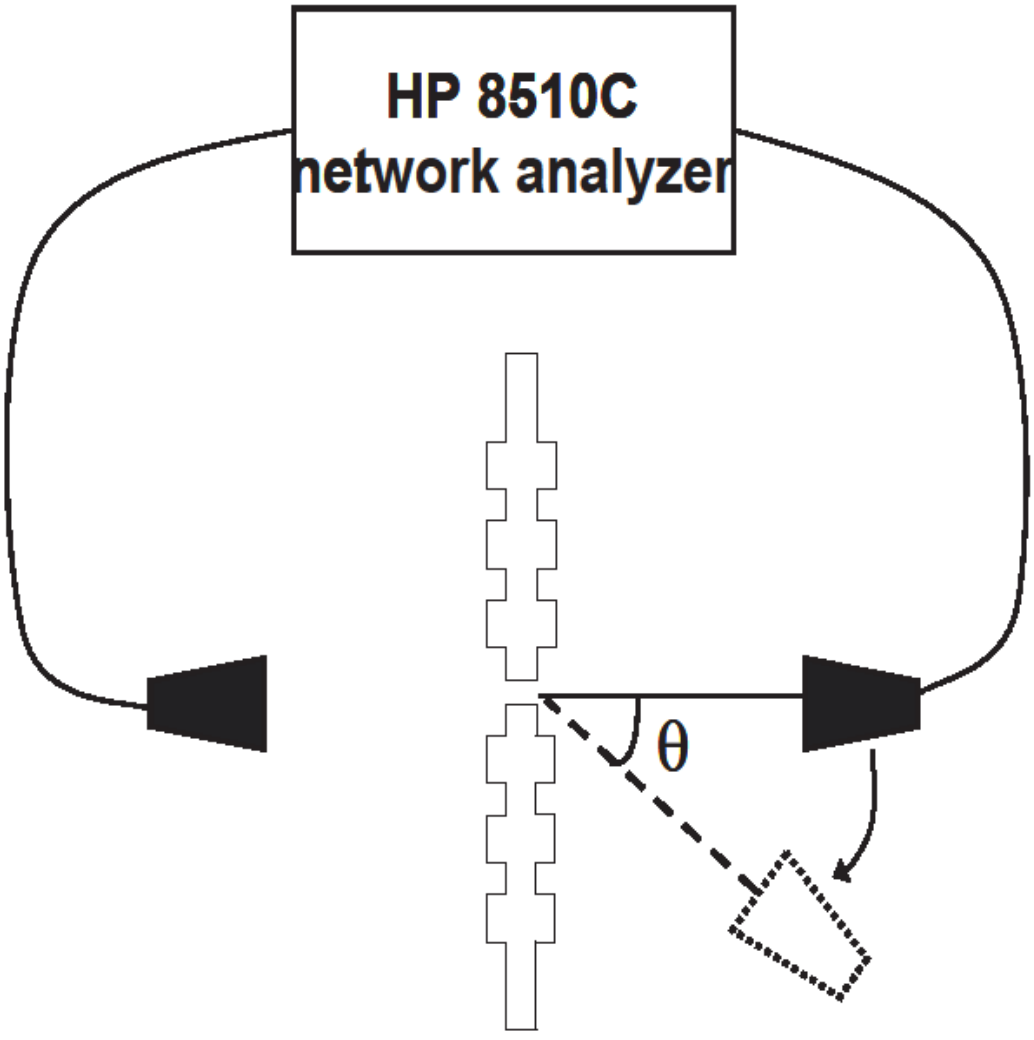

Figure 2.4: Experiment set up for angular distribution measurements.

2.3.2. Measurements

The experimental setup consisted of an HP 8510C network analyzer and two standard gain horn antennae in order to measure the transmission amplitude. Radiation was normally incident upon the sample from 15 cm by a source antenna. The receiver antenna was 100 cm away from the sample (Fig. 2.4). The receiver antenna is connected to a rotating arm to measure the angular dependence of the radiation. We change the angle of the receiver antenna with the help of rotating arm. We have 1^0 resolution in this experimental setup. Measurements were performed in the microwave spectrum of 10-18 GHz, corresponding to a wavelength region of 16.7-30 mm. Both transmitter and receiver antennas were in TM mode, so that the electric field was perpendicular to the groove direction.

Figure 2.5 presents the normalized measured and calculated angular transmission distribution at the resonance frequency (14 GHz) for reference sample and slit surrounded by periodic gratings. Angular divergence of the transmitted beam from reference sample is $\pm 12^o$, whereas the transmitted beam that emerges from slit surrounded by periodic gratings is $\pm 3^o$. The angular divergence of the beam reduced four times.

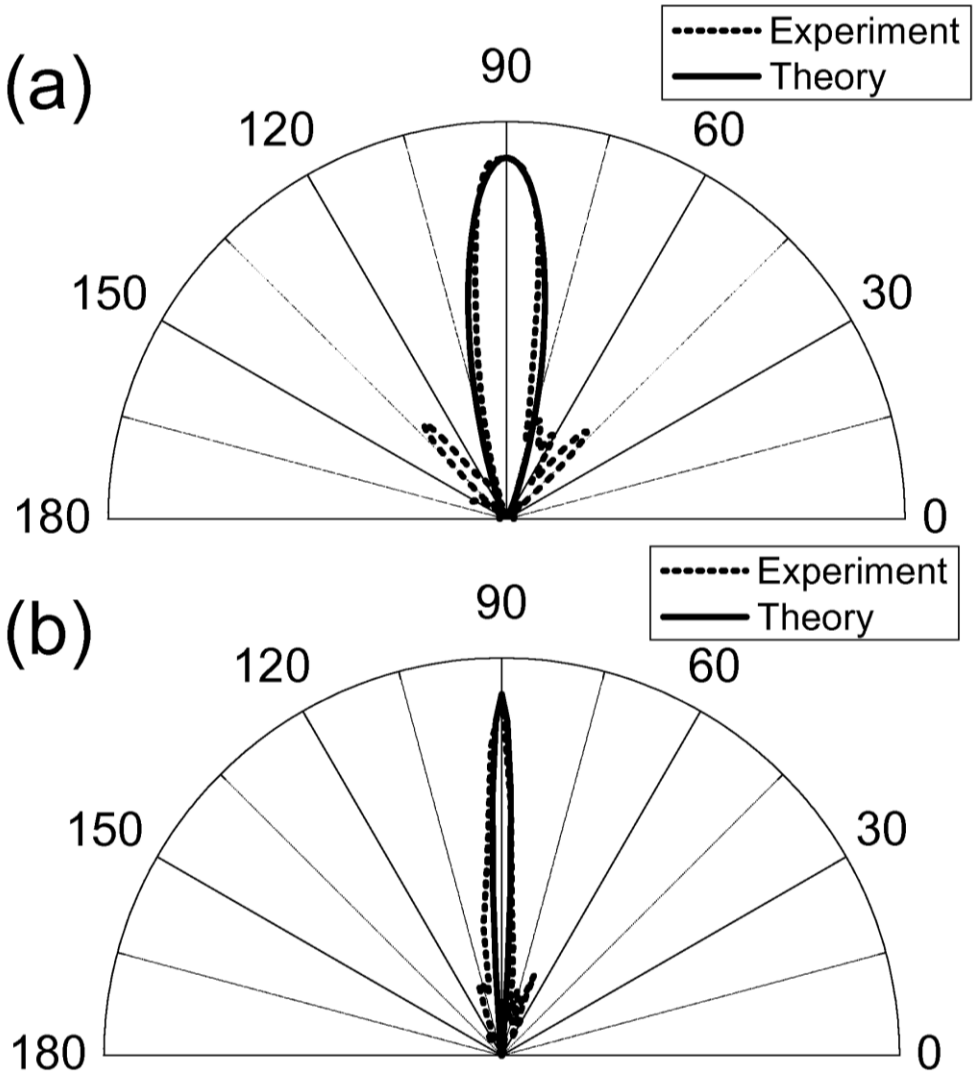

Figure 2.5: The normalized measured and calculated angular transmission distribution at the resonance frequency (14 GHz) in linear scale for (a) reference sample and (b) slit surrounded by periodic gratings.

2.4. Off-axis beaming

The emitted EM waves are confined to a narrow spatial region when the exit surface of the subwavelength aperture was surrounded by periodic gratings since the surface-wave momentum and the momentum of the corrugation around the subwavelength aperture limit the allowed range of momentum of the reradiated EM waves.

The beam is directed on the axis of the propagation direction, if the subwavelength aperture has symmetric grating periods on different sides of the output surface [15-17, 43]. However, it is possible to steer the beaming angle by using asymmetric grating periods. In order to optimize the grating periods, we firstly investigated the structures with gratings only on one side. The structures used in this study are shown in Fig.2.6.

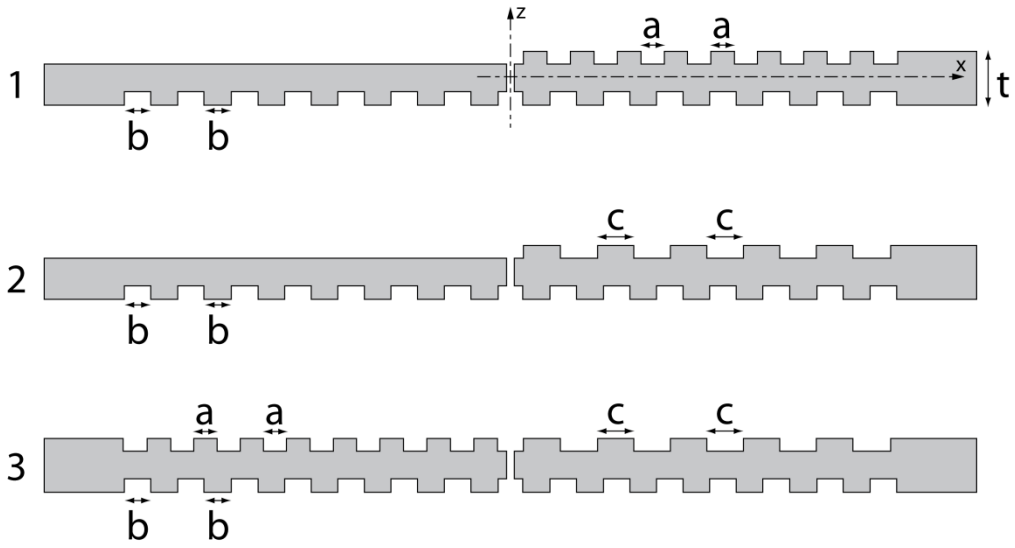

Figure 2.6: The structures used in this work where a=7 mm, b=8 mm, c=11 mm, and t=16 mm. The slit widths were 2 mm and the grating heights were 4 mm. All of them have the same input surface grating period of 16 mm in order to couple the SPs.

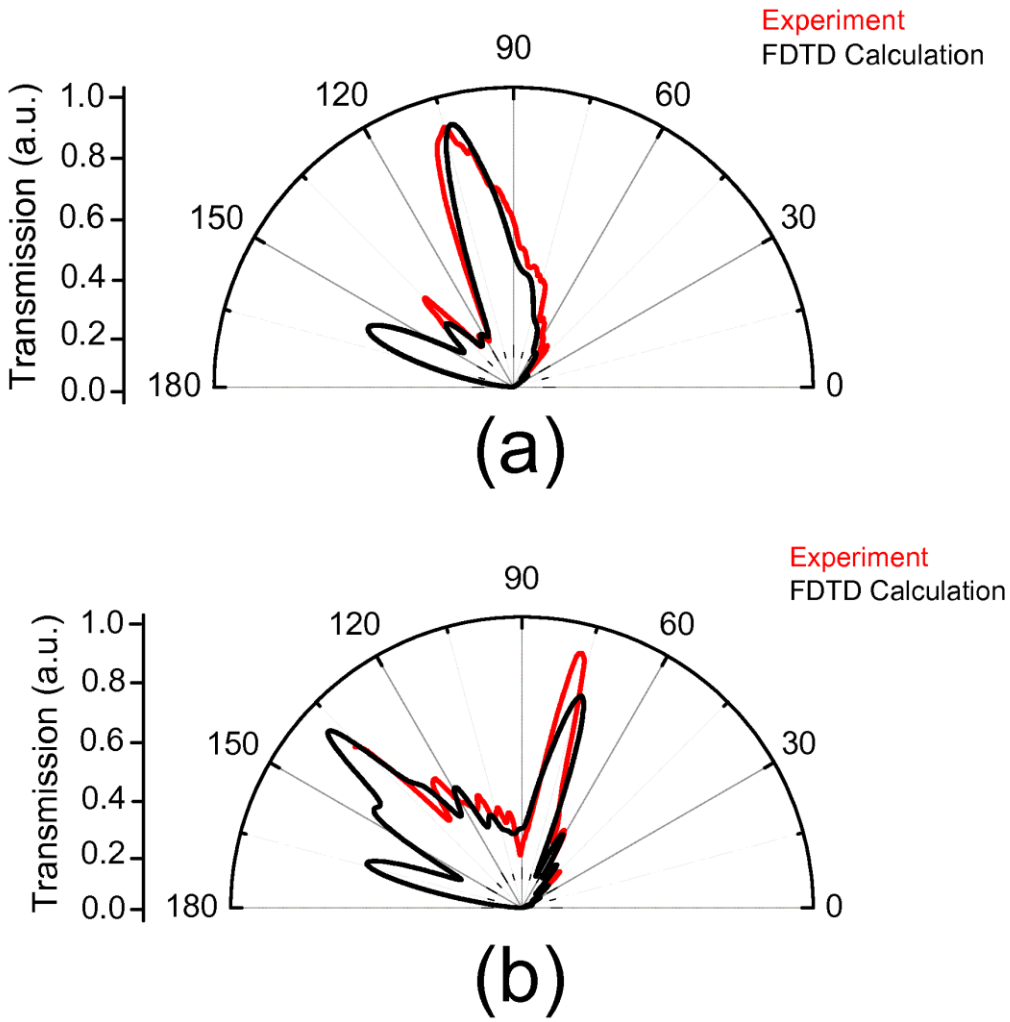

Figure 2.7: The beaming angle is steered for structures with grating periods only on one side of the output surface. The beam is mostly directed to the negative side for (a) Sample 1 and positive side for (b) Sample 2 at 14.5 GHz (20.7 mm).

We calculated the angular distribution of the transmission for a structure with a grating period 14 mm on one side of the output surface (Sample 1). In the simulation, an EM wave with an E field that was polarized in the x direction is

incident from the bottom. After the field passes through the aperture, it emits in the +z direction. The EM waves throughout Sample 1 are mostly directed to the negative side (we defined the right side of the 90^o as positive and the left side as negative) at 14.5 GHz (Fig. 2.7 (a)).

Although the EM waves throughout Sample 1 were mostly directed towards -15^o, the beam was not collimated to the narrow range. In order to obtain off-axis directional beaming we need to arrange the other side of the sample with a period that is different than 14 mm. We optimized this period by FDTD calculations to where the structure emits EM waves to the positive side. The calculated transmission for structure with a grating period 22 mm (Sample 2) shows that most of the emitted EM waves were directed towards the positive side. In the measurements of our second sample, we observed a beam at 15^o on the positive side (Fig. 2.7(b)). This case is the exact opposite of Sample1.

It is possible to steer the beam by only using Sample 1 or 2. However, the beaming is not as clear for them. In order to obtain off-axis as well as directional beaming, we combined these two structures (Sample 3). The combination of these gratings will provide a directional yet off-axis beam through the positive side. The calculated transmission between 10-20 GHz from Sample 3 shows that at the SP resonance frequency (14.5 GHz) the emitted EM waves were directed towards the positive side (Fig. 2.8).

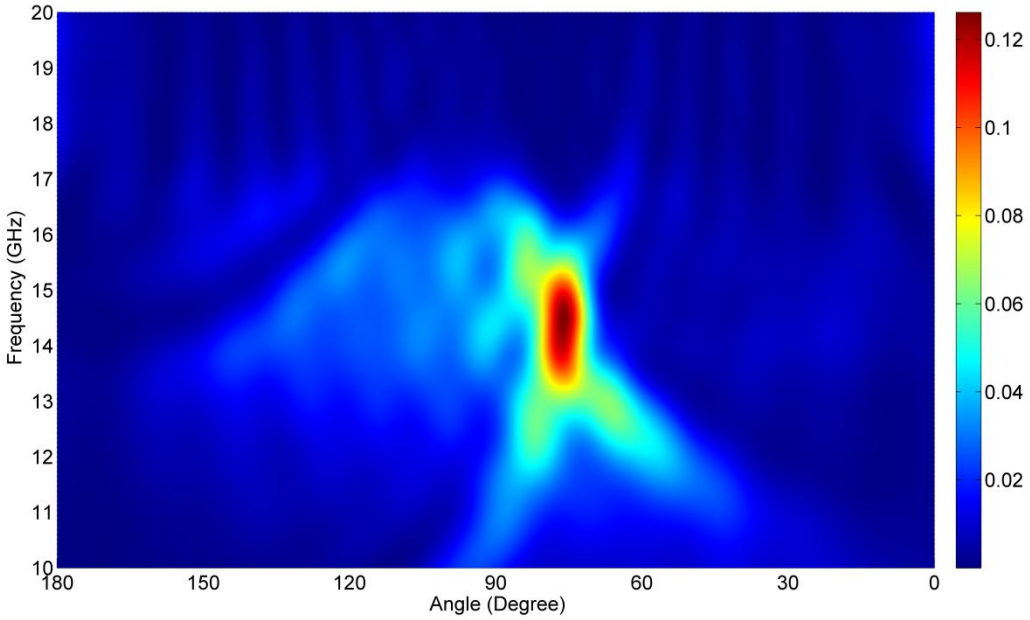

Figure 2.8: The calculated transmission throughout Sample 3 shows that off-axis and directional beaming is possible by using metallic asymmetric gratings on the output surface at SP resonance (14.5 GHz).

Meanwhile, we measured the angular distribution of the EM waves that were transmitted through Sample 3 with asymmetric grating periods on different sides. We observed off-axis directional beaming with a beaming angle of 15 degrees and a FWHM (Full-Width Half-Maximum) of 10 degrees (Fig. 2.9). This result is in good agreement with the FDTD calculations. We have also presented the FDTD mode pattern showing the coupling between the top and bottom surface at the resonance frequency (Fig. 2.10).

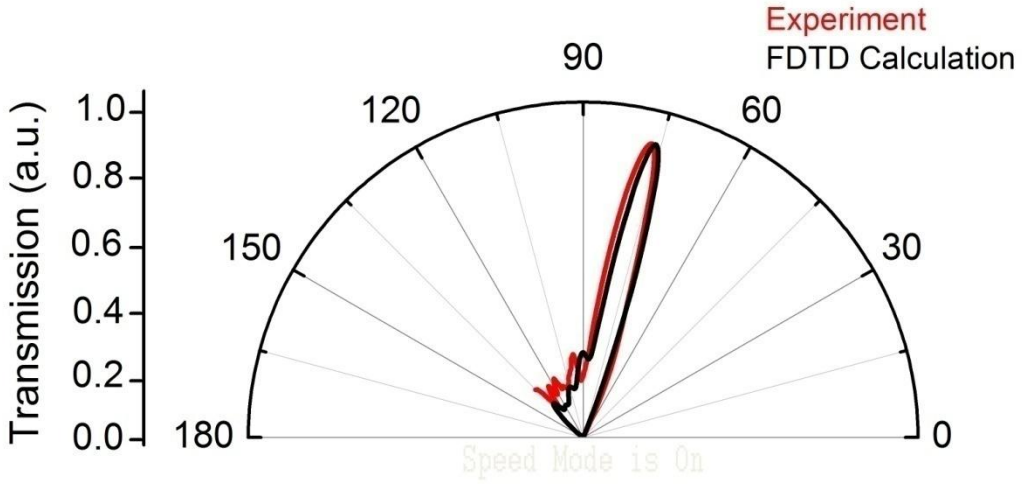

Figure 2.9: By use of a metallic structure with a subwavelength aperture at the center and the grating periods of 14 mm and 22 mm on the different sides of the output surface, we observed off-axis directional beaming with an FWHM of 10^{o} and the beaming angle of 15^{o}. It is possible to steer the beaming angle by arranging the grating periods of the output surface of the metallic structure.

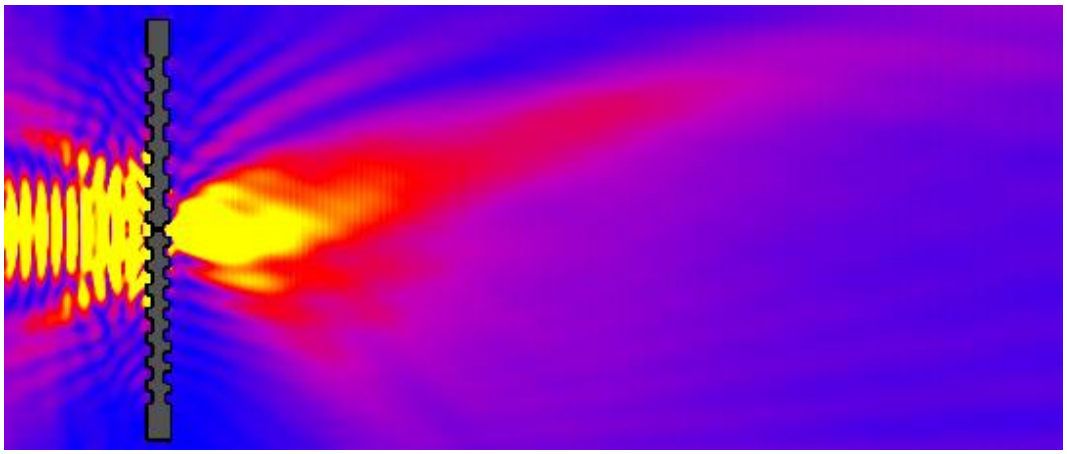

Figure 2.10: FDTD mode pattern showing the coupling between the top and bottom surface at the resonance frequency.

2.4.1. Origin of the off-axis beaming

When a p-polarized EM wave, which is incident to the metallic surface induced surface waves, flows though the aperture, and via grating, diffraction beaming phenomena occur. The SP dispersion relation and grating equation states that:

$$k_{sp} \pm N k_g = k_o sin\theta = k_{o//} \tag{2.4}$$

where k_{sp} is the wave vector of SP, $k_{o//}$ is the portion of the incident wave vector that is in the plane of the metal, N is an integer, and $k_g = 2\pi/\lambda_g$ is the grating wave vector where λ_g is the grating period.

The possibility to have steered beaming is a combinatory result of the generalized form for the conservation of the parallel component of the wave vector at the interface of a periodic medium, and the finite angle span of the source. Finite width sources can never be perfectly collimated. Thus, the input beam has a small angular span that gives $k_{in//} = \pm k_{o//}$, which is small yet non-zero. The existence of this small $k_{o//}$ is necessary to obtain the steered beaming phenomenon. This is because, that if $k_{in//} = 0$, it would be impossible to satisfy $k_{o//}(\neq 0) = k_{sp} + k_g = k_{in//} = 0$. At the interface of a homogeneous medium the parallel component of the wave vector is conserved ($k_{in//} = k_{out//}$). At the interface of a periodic medium the parallel component of the wave vector is conserved within a reciprocal lattice vector corresponding to the periodicity of the surface ($k_{in//} = k_{out//} + N k_g$). The demonstrated steered beaming (beaming angle different than zero) is always an umklapp process, i.e. a process with, and in particular an umklapp process with N=±1. The beaming angle would be restricted by the angle span of the source.

In order to understand the origin of the off-axis beaming we first revisited the symmetric case. The grating vector k_g is equal to k_{sp}. Therefore, the projected direction of the diffracted beam is on-axis (Fig. 2.11). The subwavelength aperture has an input and output side grating period of 16 mm.

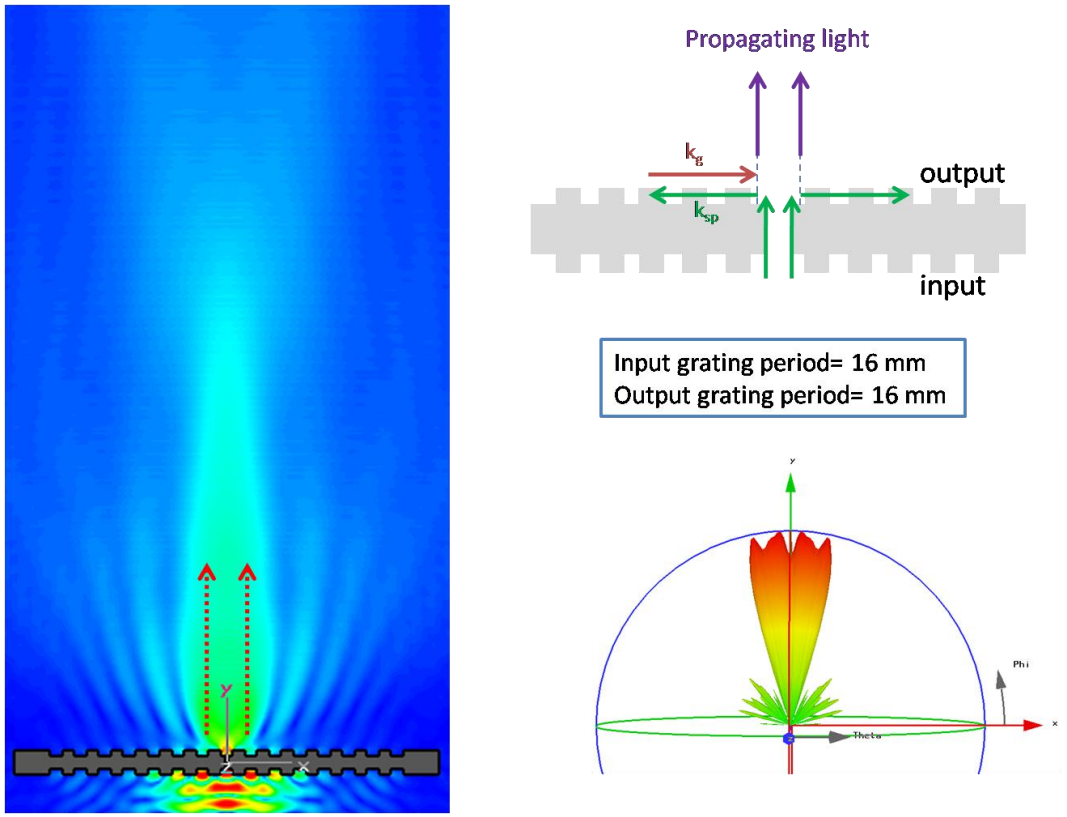

Figure 2.11: Calculated E-field and far field for subwavelength apertures with an input and output side grating period of 16 mm.

Hence, we investigate 3 different cases: 1) When the grating vector k_g is larger than k_{sp}, the in-plane component $k_{o//}$ is negative. Therefore, the projected direction of the diffracted beam is toward the waveguide channel (Fig. 2.12). The subwavelength aperture has an input side grating period of 16 mm and an output surface grating period of 14 mm.

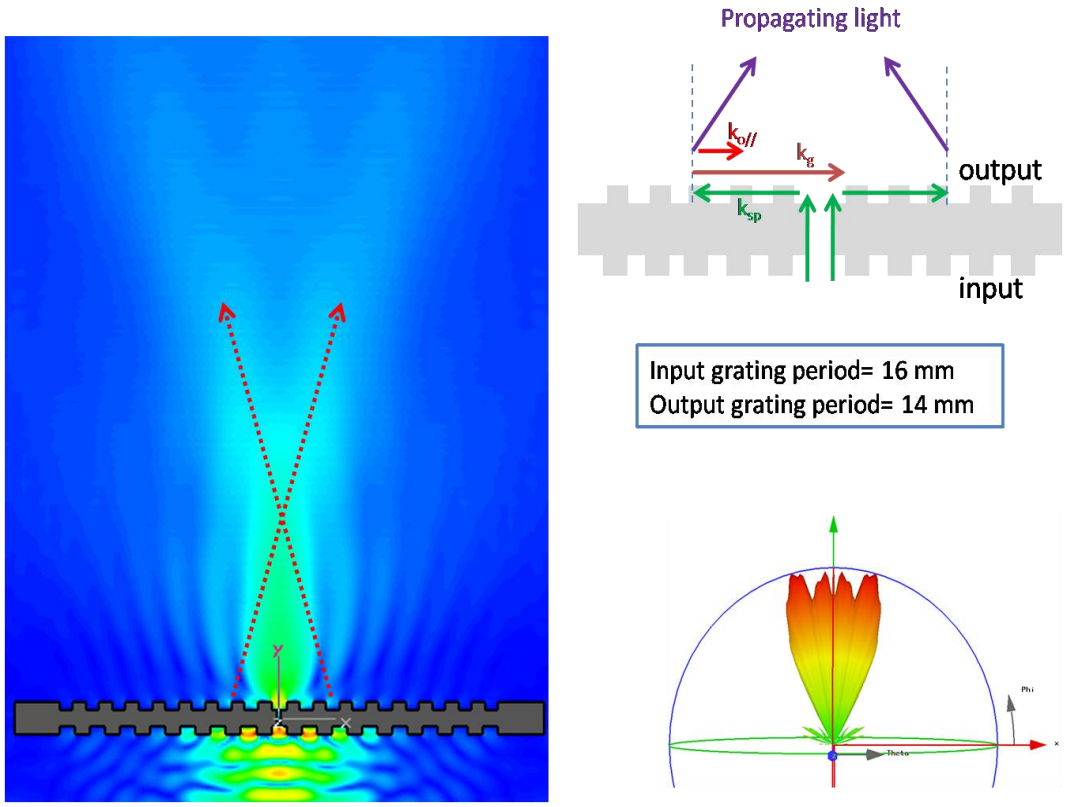

Figure 2.12: Calculated E-field and far field for subwavelength apertures with an input side grating period of 16 mm. The projected direction of the diffracted beam is toward the waveguide channel for a structure with an output surface grating period of 14 mm.

In the second case, the grating vector k_g is smaller than k_{sp}, the in-plane component $k_{o//}$ is positive. Therefore, the projected direction of the diffracted beam is away from the waveguide channel (Fig. 2.13). The subwavelength aperture has an input side grating period of 16 mm and an output surface grating period of 22 mm.

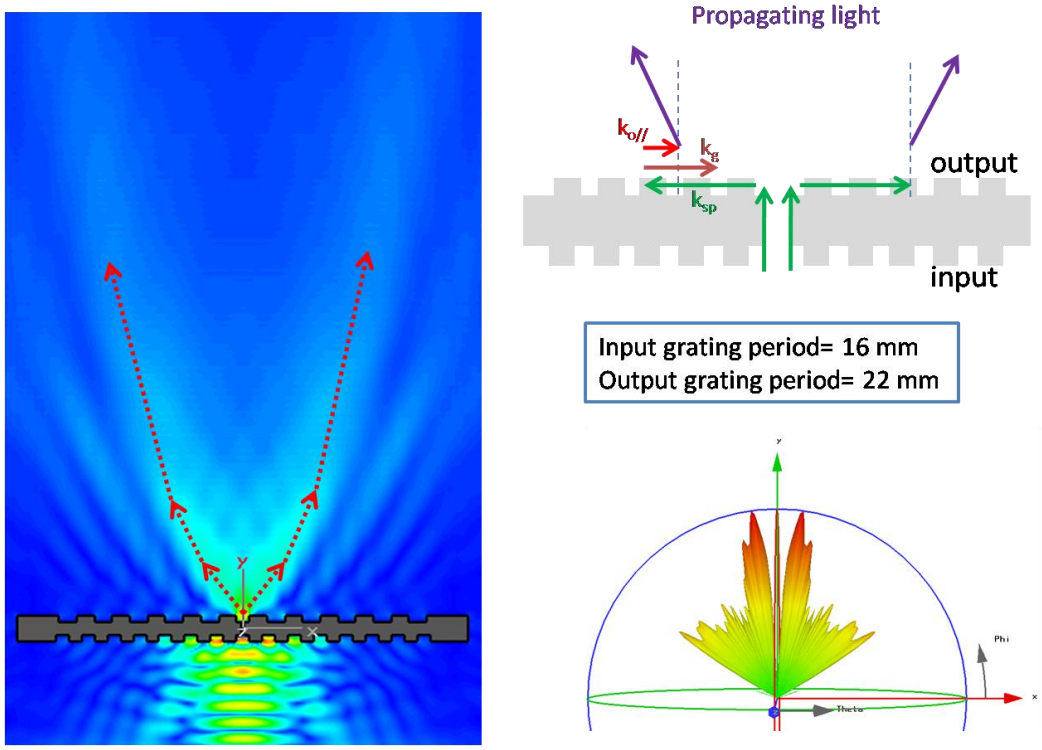

Figure 2.13: Calculated E-field and far field for subwavelength apertures with an input side grating period of 16 mm. The projected direction of the diffracted beam is away from the waveguide channel for a structure with an output surface grating period of 22 mm.

In the last case, we combined first two cases and obtained and asymmetric grating structure. The combinations of these grating vectors on the different sides of the subwavelength aperture will posses off-axis beaming (Fig. 2.14).

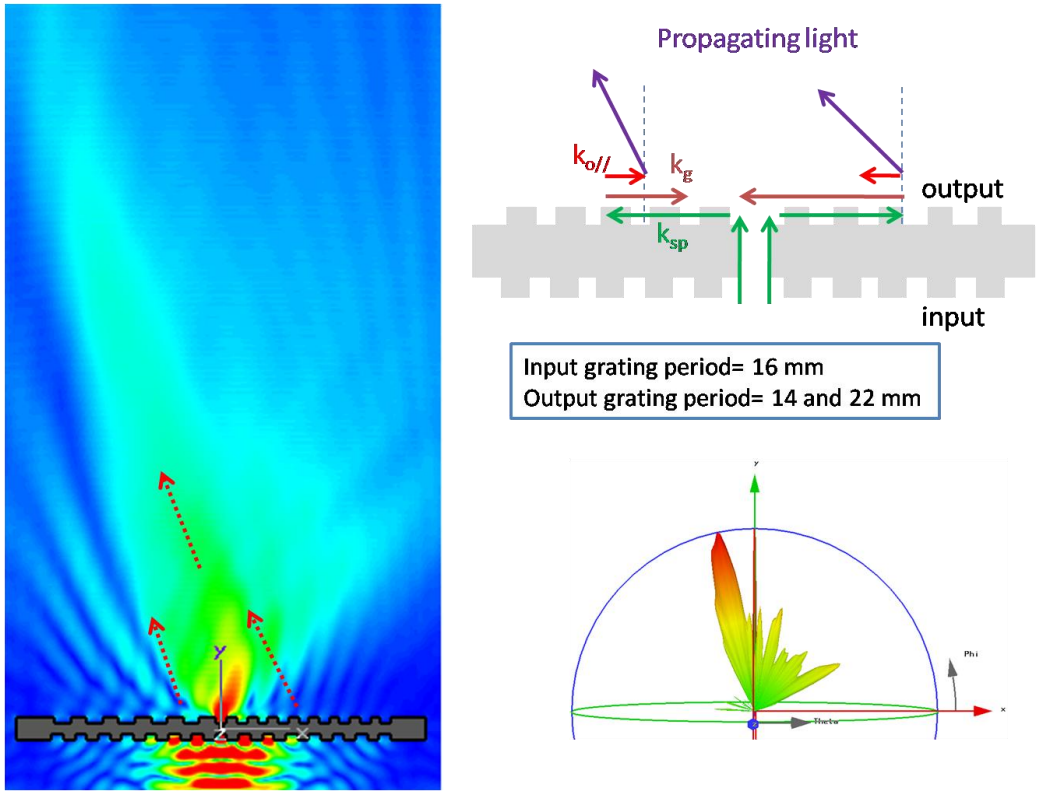

Figure 2.14: Calculated E-field and far field for subwavelength apertures with an input side grating period of 16 mm. The off-axis beam was achieved with the combination of these structures (output surface grating is 14 mm and 22 mm on the different sides of the aperture).

Hence, it is possible to change the beam by using subwavelength metallic apertures via coupling to the surface waves. The gratings have to be arranged asymmetrically in order to steer the beam. We observed a beaming angle of 15 degrees with a FWHM of 10 degrees. The momentum of the periodic corrugation, surface waves and the angle span of the finite source define the beaming angle. Our results show that it is possible to steer beam by the appropriate modification of the output surface.

Chapter 3

Off-Axis directional beaming via photonic crystal surface modes

3.1. Introduction

Photonic crystals (PCs) are periodic structures that are designed to affect the motion of photons in a similar way that periodicity of a semiconductor crystal affects the motion of electrons. PCs occur in nature and in various forms have been studied scientifically for the last 100 years. Examples of PC are shown in Fig. 3.1.

For electrons the periodic potential is provided by the periodically arranged atoms in a crystal. We shall note that appearance of a band gap for electrons is a consequence of the periodic potential. Band gap for electrons does not arise from the electron-electron interactions; rather it arises from the electron-lattice periodic potential interaction. Since the existence of a band gap is a consequence of the periodic potential it is natural to ask whether there may be band gaps for the EM waves. The possibility of the existence of band gaps for photons was long ago predicted, as early as 1979 [44]. In the case of photons, the periodic potential is provided by a periodically arranged dielectric constant. In fact the similarities

between the Maxwell equations written in an eigenvalue form and the hamiltonian for an electron propagating in a periodic potential is striking [1].

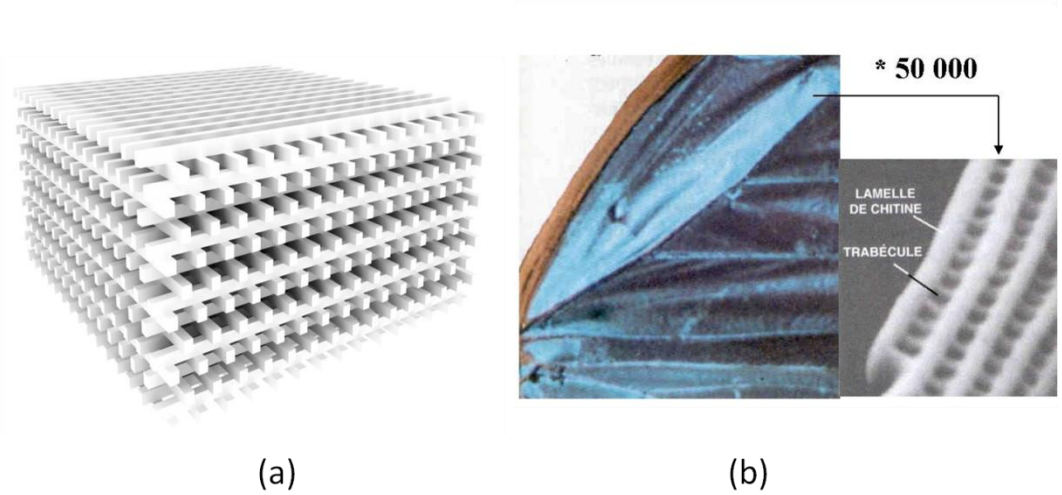

Figure 3.1: (a) A 3 dimensional PC made from alumina rods. Alumina rods are arranged in a face cubic centered arrangement. (b) There is no pigment in a butterfly wing which is blue due to PC (http://www.lpn.cnrs.fr/en/GOSS/CPOI.php).

Along with the existence of a band gap, a periodic potential for photons PCs strongly modify the dispersion properties of EM waves. Since PCs may control the propagation of EM waves in certain directions, they have recently attracted much attention. Many interesting phenomena such as enhancement and suppression of spontaneous emission [45], propagation of photons via hopping over coupled defects [46], and localized donor and acceptor modes [47], have been suggested and observed. One particular application of PCs has been commercialized by Samsung to increase the extraction efficiency of light emitting dioes (LEDs) [48].

A metallic surface and the surface of a corrugated PC have a similar property, i.e., both surfaces can support surface propagating EM waves [49, 50]. In

the previous chapter, we investigated off-axis beaming from an asymmetric metallic surface.

In this chapter, we theoretically show that PC surface can support surface propagating EM waves in the presence of a periodic corrugation. We experimentally demonstrate that when a periodic corrugation is added to the output surface of the PC, the power emitted through the PC waveguide is confined to a narrow angular region. In addition, we investigate theoretically and experimentally the possibility of off-axis beaming from PC waveguide using asymmetric periodic surface layer.

3.2. Surface Propagating Modes of PCs

There are three types of modes that are supported by a finite size PC, which is finite in one dimension and infinitely periodic in the other dimension. The first of these modes extends in the air and PC. The second mode extends in the air but decays in the PC and the last mode decays in the air but extends in the PC. Only the modes that are extending both in air and PC are observed in the transmission spectrum. The intensity profiles of these modes which are calculated using plane wave expansion method have been shown in Fig. 3.2 (a)-(c).

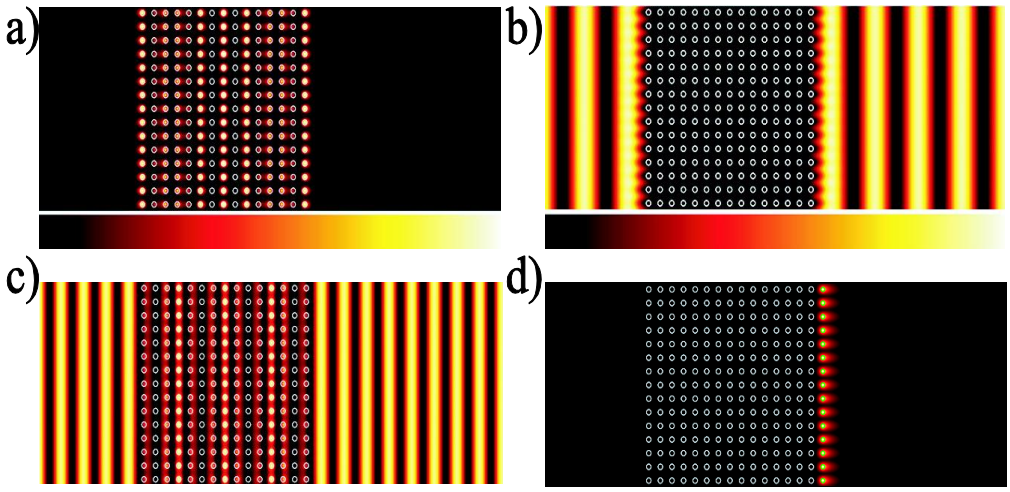

Figure 3.2: Electric field intensity profiles of the modes supported by the finite size PC: (a) mode decays in the air but extends in the PC, (b) mode extends in the air but decays in the PC and (c) mode extends in the air and the PC. (d) Surface mode: decays both in the air and PC; it is localized at the modified interface layer. These field profiles are calculated by using the plane wave expansion method.

On the other hand, the PC can also support one more mode by modifying the PC-air interface. The corrugation may be achieved by reducing the rod radius at the surface of the PC or by using rods of different shape. For this study we changed the radius of the rods at the surface of the PC from 1.55 mm to 0.76 mm.

Modes of an infinite PC can be calculated by using the plane-wave expansion method [51]. The same method can be used to identify the modes of a finite PC by employing a large enough supercell [52]. The PC is a 2 dimensional square array of circular alumina rods. The crystal is assumed to be continuous along z axis in our band structure calculations. The radius of the rods is 1.55 mm. The dielectric constant of alumina is 9.61. Lattice constants along x and y directions are 11 mm. The supercell is 40 layers long along y axis and consists of 1 unit cell along x axis. 15 unit cells along y axis contain alumina rods and the rest is free space. For comparison, we calculated the band structure of an infinite PC, i.e., infinite both in x axis and y axis (Fig 3.3(a)).

The band structure of the finite PC is calculated by plane wave expansion method with a large supercell is shown in Fig. 3.3 (b). Figure 3.3(c) shows that when the corrugation is added a band below the light line appears in the band structure (This band is shown with blue solid line in Fig. 3.3 (c) and (d).) This band is inside the photonic band gap and extends from 11.9 GHz to 12.8 GHz. The electric field intensity corresponding to these modes is calculated and plotted in Fig. 3.2 (d). Figure 3.2 (d) shows that the electric field intensity for these modes is evanescent both in air and inside PC. However, these modes have real wave vectors parallel to the PC surface. As a result, these modes are surface propagating waves.

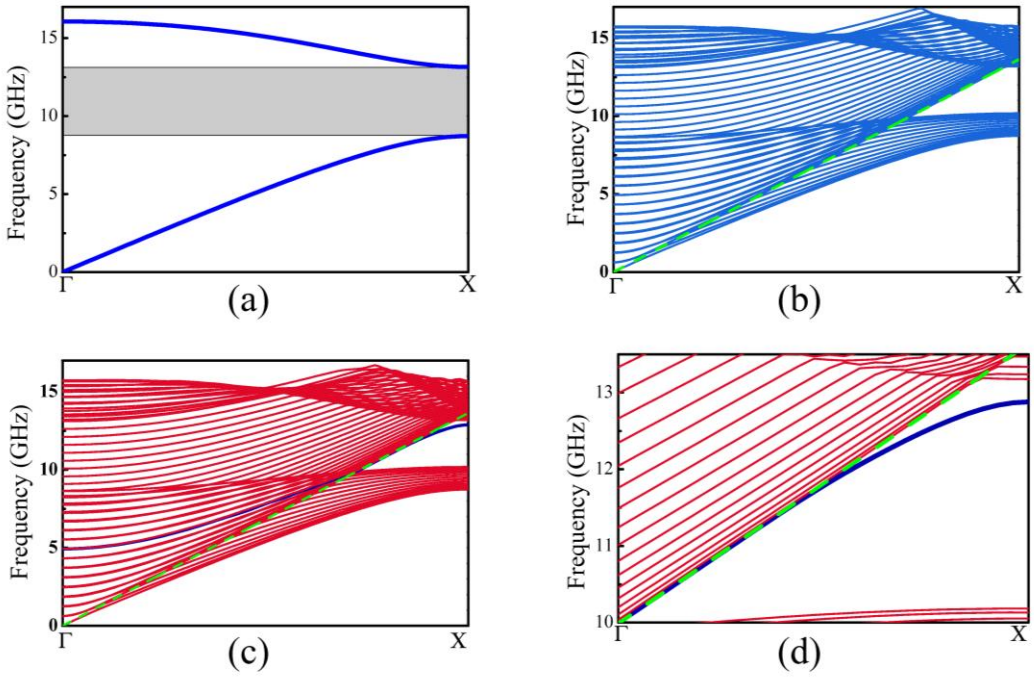

Figure 3.3: (a) The TM (electric field parallel to the axis of the rods) band structure of the infinite size PC (b) the TM band structure of the finite size (c) the TM band structure of the finite size PC when the radius of the rods at the surface of the PC is reduced to 0.76 mm. (d) zoomed view of the TM band structure of the finite size PC when the radius of the rods at the surface of the PC is reduced to 0.76 mm.

Since the surface propagating modes lie below the light line (Fig. 3.3 (d)) they cannot be excited by incident plane waves. These modes can be excited by two mechanisms. First mechanism is to couple the surface modes evanescently by using a prism configuration [53]. Second mechanism is to couple via wave vector conversion. Wave vector conversion can be achieved by adding a gratinglike structure to the surface of the corrugated PC, i.e., by adding an extra layer with a suitable lattice constant. In this study, we used the second method. We added an extra layer in front of the corrugated PC surface. The added layer is composed of alumina rods with a radius of 1.55 mm and a lattice constant of 22 mm.

3.3. Directional beaming from PC Waveguide

The EM waves emitted through a sub-wavelength aperture have a broad angular distribution, i.e., EM waves quickly diffract in all directions [14]. This phenomenon is investigated in the previous chapter.

The PC waveguide that we used in this study has a width smaller than the operation wavelength. The operation wavelength is around 2.5 cm, whereas the waveguide width is 1.9 cm. Hence, it is expected that the EM waves emitted through the PC waveguide would diffract in all directions from the PC waveguide aperture. We measured the intensity of the EM waves emitted through the PC waveguide over a rectangular area of 35x60 cm^2. Measurement setup consists of transmitting horn antenna and receiving monopole antenna. The PC waveguide is excited with the incident waves emitted through the transmitting horn antenna. Electric field intensity is measured on the exit side by using the monopole antenna with 0.5 cm steps. The measured intensity distribution at 12.45 GHz is shown in Fig. 3.4. The data shows that the EM waves emitted through the PC waveguide quickly diffracts in all directions.

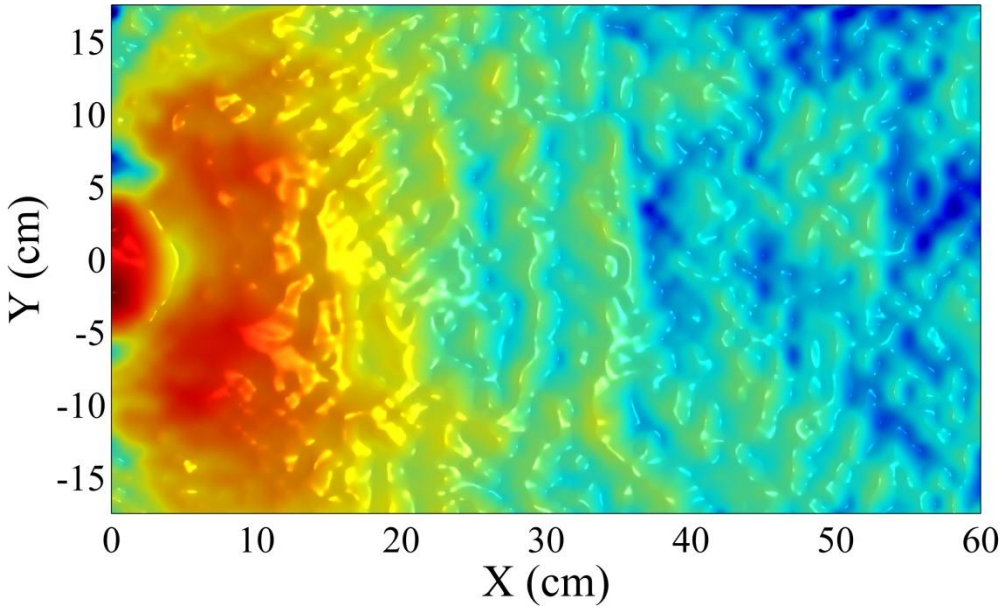

Figure 3.4: The measured intensity distribution at the exit side of the PC waveguide. Y-axis is parallel to the PC surface.

In the previous section, we showed that surface modes can be created on the surface of the PC by changing the radius of the rods on the PC surface. Since the modes of the PC waveguide decay into the bulk region of the PC, surface modes can be excited by the PC waveguide. Figure 3.5 shows the calculated electric field intensity at 12.45 GHz when the radius of the rods at the exit surface of the PC waveguide is reduced from 1.55 mm to 0.76 mm. The PC waveguide is excited by the incident Gaussian wave. The beam width is 10 lattice constants long. The PC waveguide is 15 lattice constants long along the propagation direction. The field intensity is calculated by FDTD method. The data shows that the surface modes are excited by the PC waveguide. In addition, Fig. 3.5 shows that the surface modes are not coupled to the radiating modes of the free space.

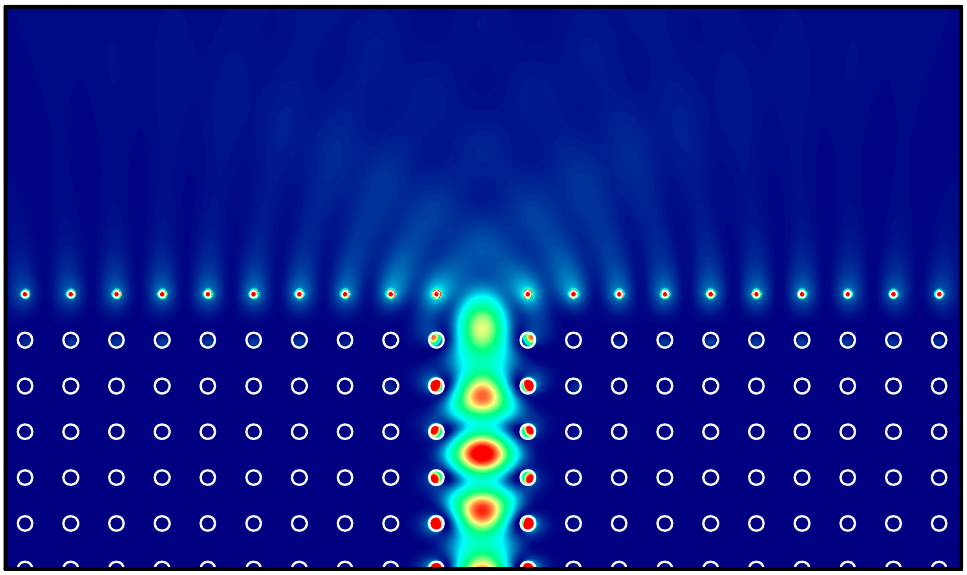

Figure 3.5: Calculated field intensity when the surface corrugation is added to the exit surface of the PC waveguide.

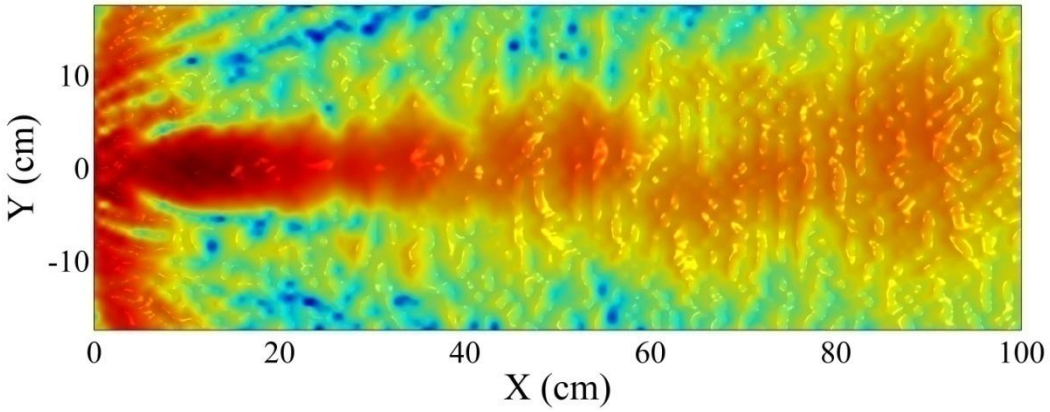

Figure 3.6: The measured intensity distribution at the exit side of the PC waveguide when the corrugation and grating-like layer are added to the exit surface of the PC waveguide. Y-axis is parallel to the PC surface.

The surface modes excited by the PC waveguide can be coupled to the radiating modes of the free space when a grating-like layer is added in front of the corrugation. We formed the grating-like layer with rods that have equal radius to the bulk PC rods. The grating-like layer has a period of twice the bulk PC period. The measured electric field intensity at 12.45 GHz over a region of 35x50 cm^2 area on the exit side of the PC waveguide in the presence of corrugation and grating-like layer is shown in Fig. 3.6. Figure 3.6 shows that the electric field intensity is confined to a narrow spatial region and propagates without diffracting into a wide angular region. In addition, the measured far field radiation patterns of the EM waves emitted from the PC waveguide with and without surface corrugation and grating-like layer is shown in Fig. 3.7(a) and (b), respectively. Figure 3.7(a) shows that without the surface corrugation and grating-like layer the emitted power spreads into a wide angular region. However, Fig. 3.7(b) shows that with the surface corrugation and the grating-like layer the emitted power are confined to a very narrow angular region with a half power beam width of 10 degrees.

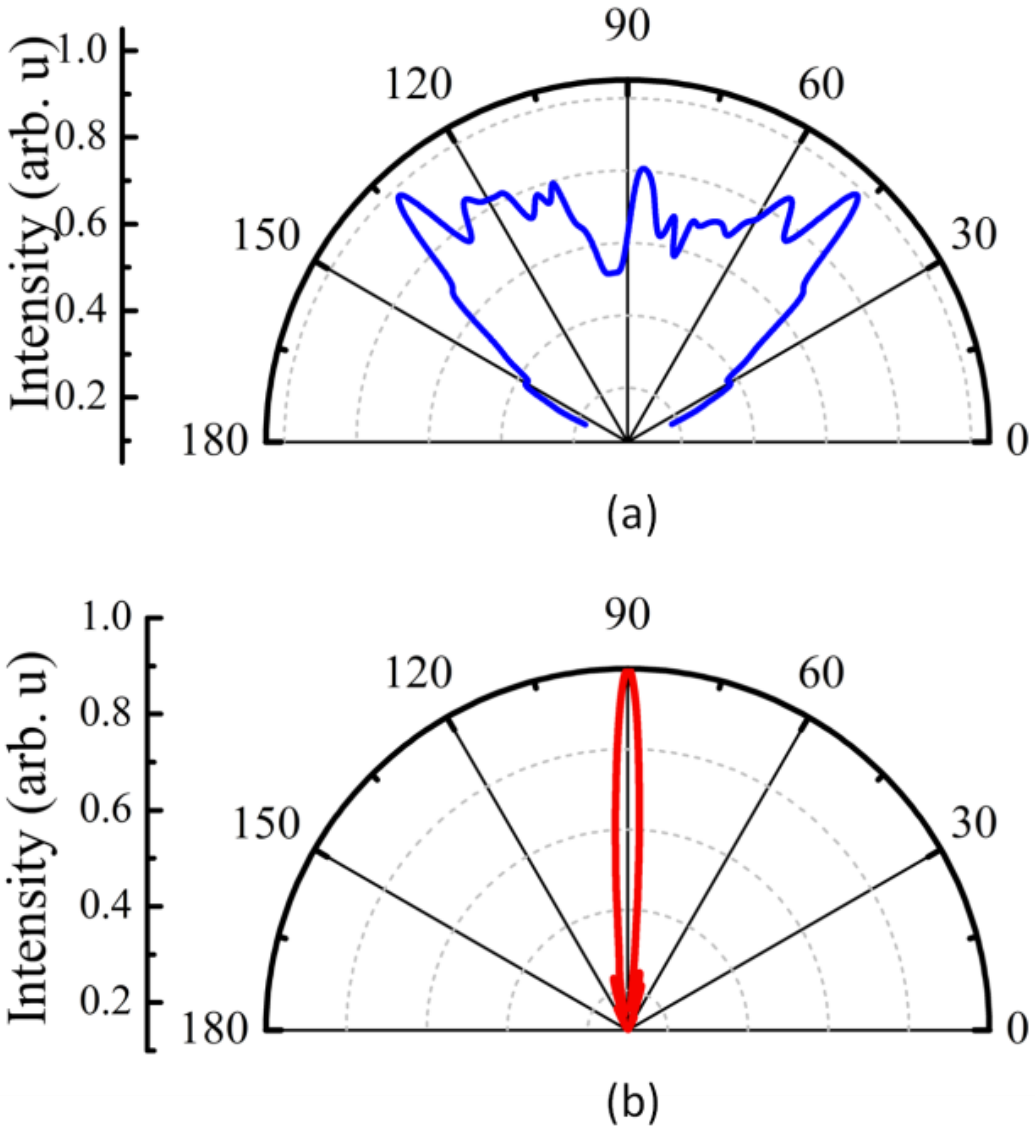

Figure 3.7: (a) Measured far field radiation pattern of the EM waves emitted from PC waveguide at 12.45 GHz (b) Measured far field radiation pattern of EM waves emitted from the PC waveguide with surface corrugation and grating-like layer.

3.4. Off-Axis directional beaming via Surface Modes of PC

In this section, we investigate the control of directional beaming via a PC waveguide with asymmetric surface corrugations. By using this new structure, we were able to change the beaming angle and attain off-axis directional beaming from a PC waveguide with subwavelength width.

In this study, we used the same PC waveguide structure with corrugation layer. However, we have used an asymmetric grating-like layer. The asymmetric grating-like layer has a period of twice the bulk PC period (22 mm) on one side and 33 mm (3xa) on the other side of the PC waveguide (Fig. 3.8). The grating-like layer is identical to the gratings on the output surface of the metallic structures. The EM waves throughout the waveguide diffract from this layer. The momentum of the periodic corrugation, surface waves and the angle span of the finite source define the beaming angle. Therefore, to steer the beaming angle period of the grating like layer, the different sides of the waveguide have to be different.

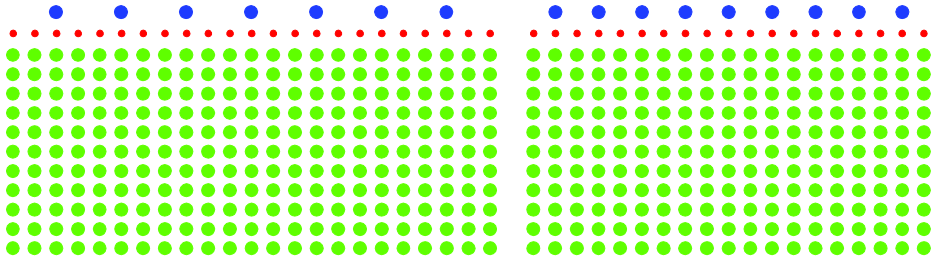

Figure 3.8: The 2D PC is constructed from a 43x11 square array of circular alumina rods (indicated as green dots). The crystal is 11 layers along the propagation direction. The radius of the rods in the modified layer (indicated as red dots) is half of the regular rods (0.76mm). The rods in the grating-like layer have equal radii of the bulk PC rods (indicated as blue dots). The asymmetric grating-like layer has a double period (22 mm) on one side and a triple period (33 mm) on the other side of the PC waveguide.

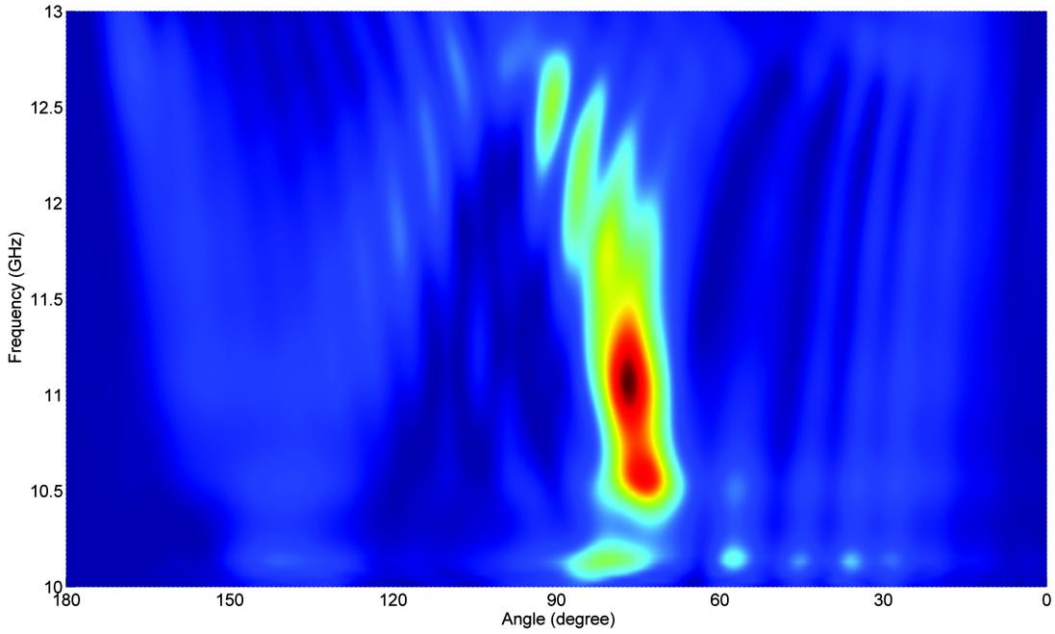

Figure 3.9: FDTD calculations of the transmission from the PC waveguide exhibit off-axis beaming around 11 GHz. The periods of the grating like layer on the different sides of the waveguide were designed as 22 mm and 33 mm in order to steer the beaming angle.

Figure 3.9 exhibits the FDTD calculations of the transmission from this PC waveguide. We used the same simulation tools and experiment setup for this part as in the metallic structures, but we used s-polarization (E- field is parallel to the rods). The off-axis beaming is obtained around 11 GHz. The measured and calculated radiation patterns of the EM waves emitted from the PC waveguide at 11.1 GHz is presented in Fig.3.10. We observed a beam that is confined to a narrow angular region with FWHM of 10 degrees and beaming angle is 14 degrees. This result is in good agreement with the FDTD calculations.

In addition, we measured the electric field intensity at 11.1 GHz over a region of 60x70 cm^2. Figure 3.11 shows that electric field intensity is confined to a narrow spatial region and propagates along 14 degree without diffracting. Hence,

the asymmetric grating-like layers provide an off-axis directional beaming from PC waveguide via PC surface modes.

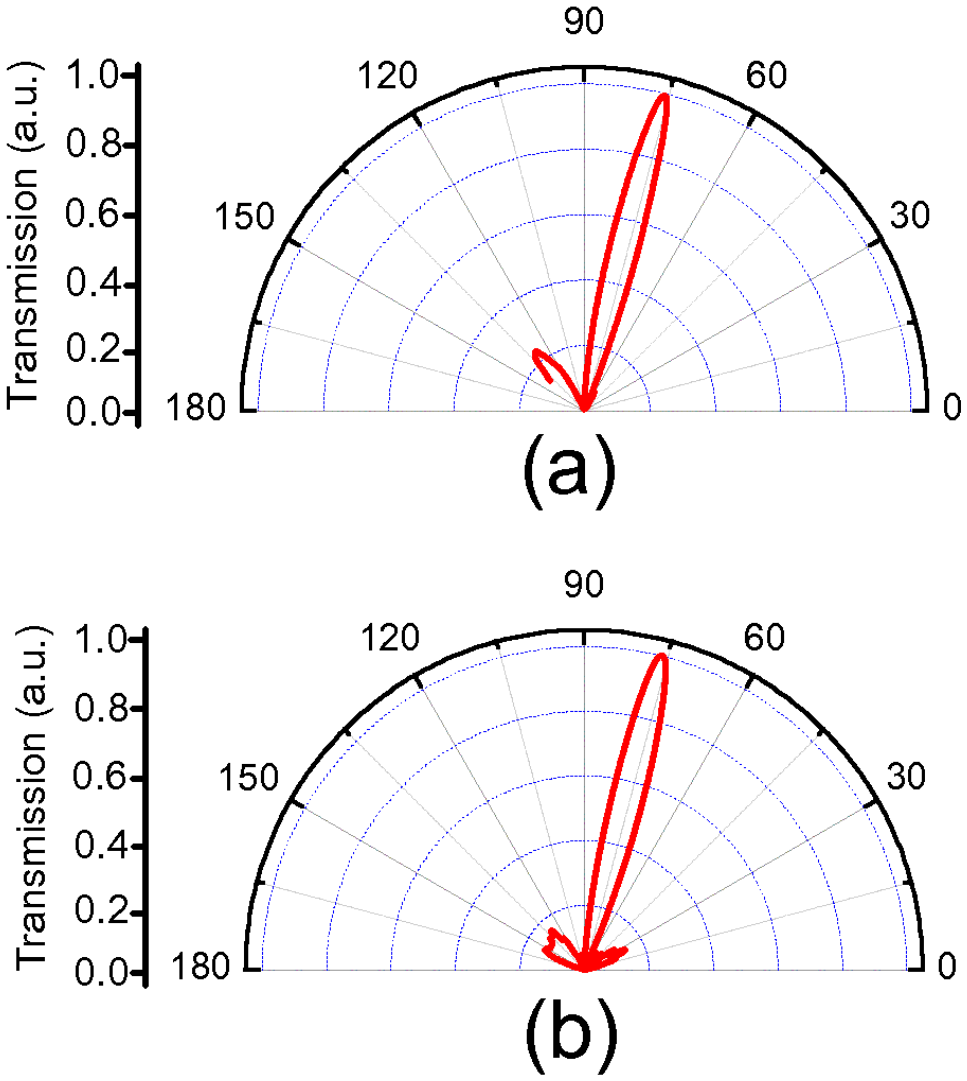

Figure 3.10: The measured (a) and calculated (b) radiation patterns of the EM waves emitted from the PC waveguide at 11.1 GHz. The right side of 90^{o} stands for the side with grating-like layer period of 33 mm.

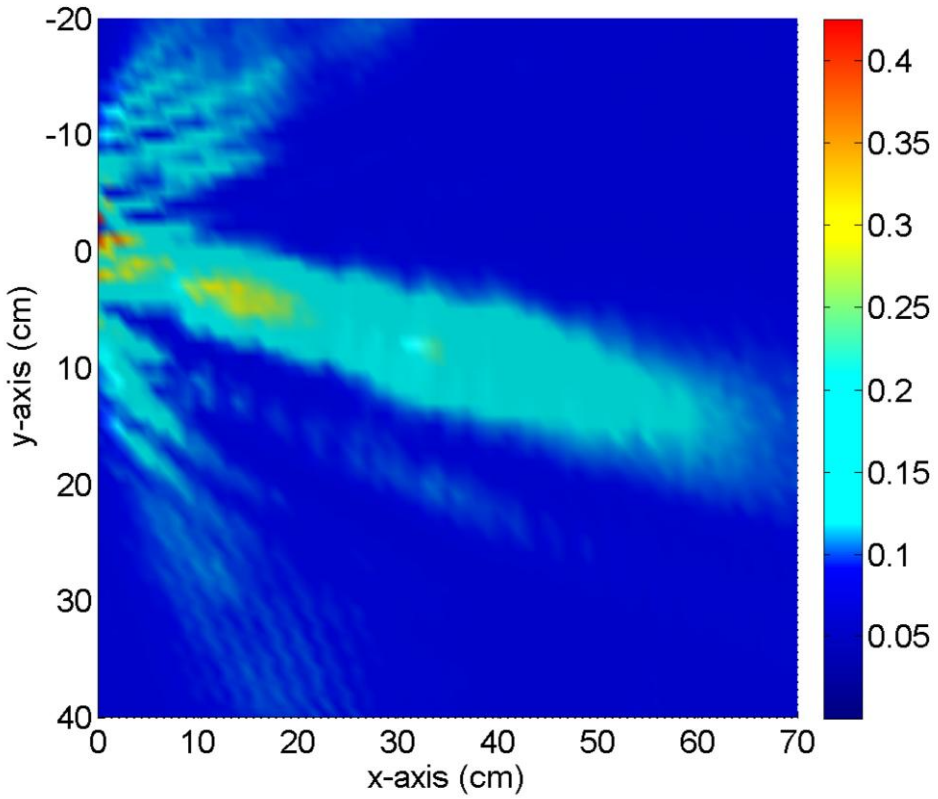

Figure 3.11: The measured intensity distribution at the exit side of the PC waveguide when the corrugation and grating-like layer are added to the exit surface of the PC waveguide. Y-axis is parallel to the PC surface and positive side of the axis indicates the side of grating-like layer with period of 33mm.

The off-axis beaming can be explained using SP diffraction theory. This theory states that: when wave vector of the SP is smaller than the grating vector, the wave vector of the diffracted light will be negative, or vice versa. This can be stated also as: the projected direction of the diffracted beam is opposite that of the SP propagation. Since the same phenomena holds for the surface waves of the PC, depending on the period of the grating-like layer the direction of the emitted beam changes. For the directional beaming, the grating-like layers with same periods on both sides of the waveguide, the two emerging beams overlap to form a beaming

pattern along the axis of propagation direction. On the other hand, the grating-like layers with different periods on different sides of the waveguide can be arranged such that the wave vector of one of the grating-like layer is negative and the wave vector of the other grating-like layer as positive. Hence, such a combination will provide a directional yet off-axis beaming.

Chapter 4

Frequency dependent steering with backward leaky waves

4.1. Introduction

As mentioned in the previous chapter, PCs [54-56] support Bloch surface waves [49]. In order to excite surface waves, a periodic surface defect layer may be placed at the exit of a PC waveguide [22-24, 57, 58]. These waves are analogous to SPs that are generated on the surface of corrugated metal films [15, 21]. Each corrugation on the metal slab acts as a passive element of an array antenna, excited by its neighbors, which results in directional beaming. Similarly, in the case of a PC, surface waves are diffracted by the dielectric periodic surface scatterers, that are separated by intervals that are smaller than the free space wavelength [22, 23, 58].

In the previous chapters, we investigated off-axis directional beaming, rather than the steering of the directional beam. There are also other studies focused on the in-plane steering of the radiation angle without relying on surface waves [59]. Leaky wave antennas, which are basically radiative transmission lines, have been used to achieve beam steering in the endfire and backfire directions via

forward and backward leaky waves. An overview of the physics of leaky waves, and their role in producing narrow-beam radiation, may be found in a pair of fundamental papers published by Tamir and Oliner in 1963 [60] [61]and also in [62]. In certain leaky wave antennas the beaming angle was adjusted electronically by changing the applied control voltage [63, 64] or mechanically by tuning the resonance frequency at a single operation frequency [65] . A frequency squint (i.e., the frequency dependence of the beaming angle) is typical of leaky wave radiators. The use of interdigital capacitors along the transmission line [63], the placement of dielectric rods in a waveguide [66]. In the work by Jackson *et al.* [66], a leaky wave explanation has been given for the problem of a plasmon wave on a corrugated silver surface, excited by a subwavelength aperture, that produces directive beaming of light. However, a beaming device relying on surface wave physics applicable at the optical wavelengths, and that does not rely on plasmonic waves, has yet to be reported. The use of leaky surface waves on a PC which has frequency scalability property may serve this purpose.

In this chapter, we have studied the surface mode and the radiation mode of a 2 layer PC under a surface defect layer called as the “dimer-layer” (Fig. 4.1). Previously, in addition to studies about the radiation behavior of sources placed inside PCs [67], the mechanism of directive radiation achieved via the surface of the PC has been already investigated [68]. The surface was regarded as a system of radiating sources whose resemblance with an array antenna was also shown. Here, the dimer-layer will be shown to support a backward guided bounded mode (surface wave) as well as a backward leaky mode. For the latter case, the PC structure behaves as a leaky wave antenna. Prior to our present study, the characteristics of surface waves propagating along a dimer-layer were investigated in [69], and especially backward propagating waves constituted an important part of the investigation. A modified version of the Attenuated Total Reflection technique was used in order to experimentally display the backward wave propagation phenomenon. Waves radiated by an inclined horn antenna were

coupled to the surface modes of the dimer-layer via a plexiglass prism. As an alternative approach, the exploitation of line sources placed inside the periodic configuration has been used to excite surface modes. We have adopted this latter approach in this study: a transverse monopole source is utilized to excite the surface and leaky modes in the dimer-layer. The dispersion diagram of the arrangement is obtained by employing the Rsoft Bandsolve Software which uses the Plane Wave Expansion (PWE) Method. Changes in the radiation angle of the beam as a function of frequency are confirmed experimentally. The measurement results are also supported by Finite Difference Time Domain (FDTD) Method simulations carried out with Rsoft Fullwave Software. Finally, the experiment concerning the half dimer-layer structure is used to explain the backward characteristics of the observed radiation.

4.2. Experimental Setup

Throughout the present study, three configurations are experimentally investigated, for gaining physical insight into the formation of the narrow-angle radiation patterns: 2-Layer PC (PC2), 3-Layer PC (PC3), and 2-Layer PC with a dimer-layer (PCD), which are shown in Fig. 4.1. The PC and the dimer-layer are constructed with the same kind of alumina rods with a relative permittivity ε = 9.61 (refractive index n = 3.1). The rods have a diameter $2r$ = 3.2mm and a length of 15.4cm. The PC2 (Fig. 4.1(a)) is assembled as an array of 2x100 rods with a lattice spacing a = 9.6mm (r=a/6). The PC3 consists of 3x100 rods of the same kind placed with the same lattice spacing a (Fig. 4.1(b)). The dimer-layer placed on top of PC2 provides the PCD structure, which is the third one investigated in this work (Fig. 4.1(c)). Dimer rods are in contact to each other, in pairs, at the lattice corners with periodicity of a. Therefore, their center to center distance is $2r$=a/3. The monopole antenna is inserted at the mid–point, with respect to the x-direction, of the overall structure, half a lattice constant (a/2) away from the PC surface for each configuration. The monopole within the frequency band of 11-

14.84 GHz (a/λ: 0.352-0.475) operates well as the excitation source. The excited transverse electric (TE) waves (along both the $\pm x$ directions) have an electric field component (E_y) parallel to the rods. As shown in Fig. 4.1(d), an Agilent two-port 5230A Programmable Network Analyzer (PNA) feeds the Agilent 8349B Microwave Amplifier, which drives the source antenna with a gain of 20dB. Angular distribution (AD) measurements of the transmission coefficient are carried out by employing a horn antenna as a receiver, scanning the semicircular path shown in Fig. 4.1(d), 1m away from the source.

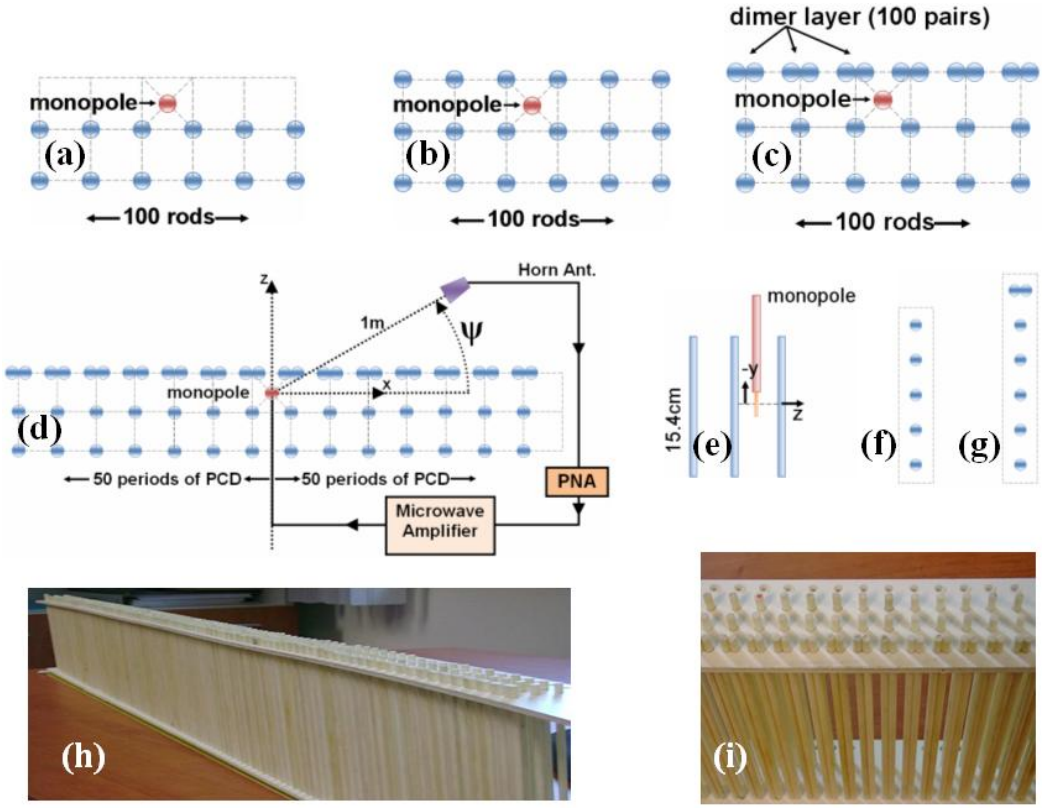

Figure 4.1: (a) PC2 structure, (b) PC3 structure, (c) PCD structure, (d) Experimental setup with the PCD, (e) side view of the monopole with the rods, (f) Single periodicity-cell of PC made of 5 layers (PC5), periodic along the *x*-direction (to be used in the simulations), (g) Single periodicity-cell consisting of the PC5 with a dimer on top, periodic along the *x*-direction, which is also used in the simulations, (h,i) images of the PCD that is constructed.

4.3. Dispersion Diagram

We first show in Fig. 4.2 the dispersion diagram of waves traveling along the *x*-direction for the two cases in Fig. 4.1(f) and 4.1(g). In particular, periodicity-cell for a PC (periodic along the *x*-direction) with 5 layers (PC5) stacked in the *z*-direction is shown in Fig. 4.1(f), and the structure, consisting of PC5 with a dimer-layer placed on the top is shown in Fig. 4.1(g). For the calculation of the band diagram, the unit cell is defined as periodic both in the *z*- and *x*-directions by the software used. The unit cell used in the simulations includes the structure shown either in Fig. 4.1(f) or Fig. 4.1(g) at the center. Besides, since we aim at simulating a structure periodic only in the *x*-direction, the periodicity of the unit cell along the *z*-direction is modified as follows: Along the *z*-direction, 50 periods (*a*) of free space are left above and below the structure to be simulated (this free space region is not shown in Figs. 4.1(f) and 4.1(g)). Therefore the simulated periodic unit cell consists of a PC5 structure, with replicas separated by 100 periods (*a*) of empty space along the *z*-direction, which space is considered to be long enough to well approximate the finite number of layers of the actual structures along *z*-direction. The PC5 with the dimer-layer in Fig. 4.1(g) is simulated in the same manner. In the dispersion diagram, obtained by using the Rsoft Bandsolve softwave, $k_{//}$ is the propagation wavenumber along the *x*-direction, and a bandgap for $0.339<a/\lambda<0.468$ (10.59-14.62GHz) is observed for the PC5 structure (between the dashed curves in Fig. 4.2). For the PC5 with dimer-layer case instead, due to the presence of the dimer layer, a defect surface mode is introduced in the dispersion diagram. The dotted curve for the surface mode in Fig. 4.2 has a negative slope. The figure shows the purely real part of the propagation constant of this mode below the light line. In the measurements, we will reduce the number of PC layers while in the interpretation of the experimental work, we are still going to rely on Fig. 4.2 since the fields radiated by the monopole would not significantly propagate through the bottom layers of the PC, in the frequency range

investigated. That is, reduction of the number of layers in PC will have a minor effect on guiding and beaming of waves created within the bandgap of the PC.

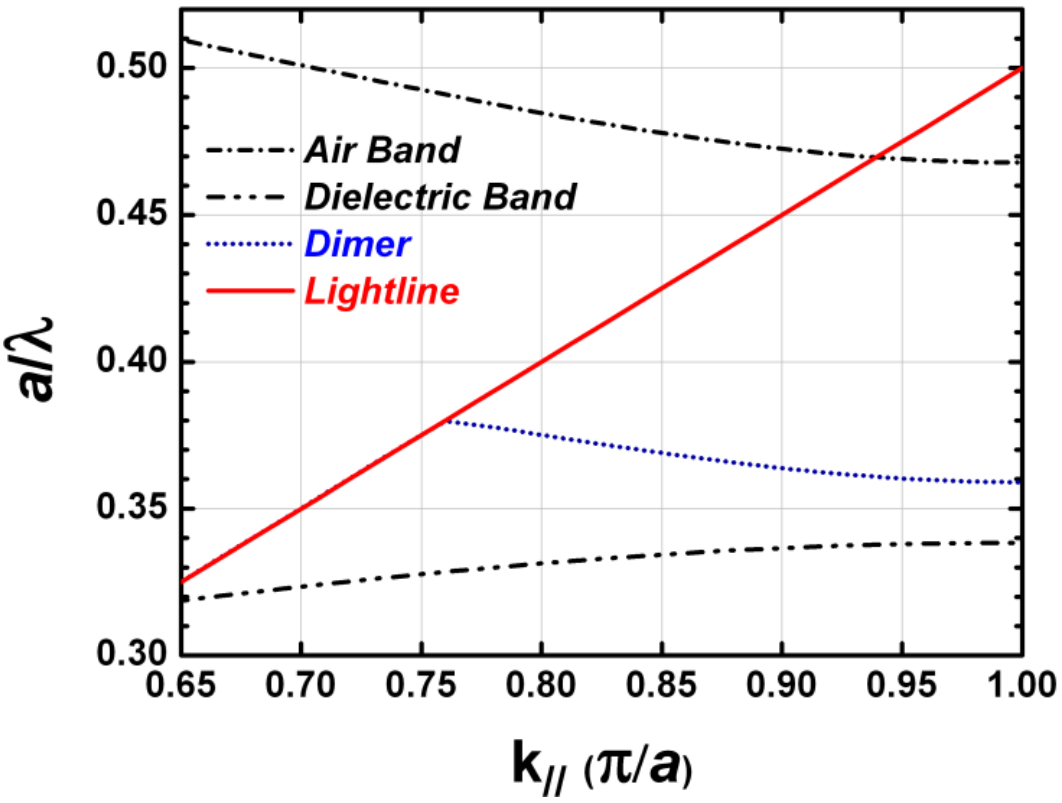

Figure 4.2: Dispersion diagram describing propagation along the *x*-direction. The surface mode in the dimer-layer (blue dot) resides inside the bandgap bounded by the air band (dash-dot) and the dielectric band (dashed with two dots) of the PC5 structure without dimer-layer.

4.4. Radiation properties of a source embedded in the PCD

The radiation characteristics of the three configurations (PC2, PC3, and PCD) excited by the monopole are simulated by using a 2D FDTD scheme of Rsoft Fullwave software and measured using the experimental setup with the same number of rods and layers like those used in Fig. 4.1. Both simulated and

measured results are collected at a distance of 1m from the center (where the source is located). The only difference is that in the simulation the structure has been approximated as infinitely long in the *y*-direction, and excited by a line source.

Regarding the AD of the radiation from the monopole source which is measured in free space (i.e., without any PC), it is observed that the AD is not completely uniform in the angular range. Moreover, average value of the amplitudes in the AD decreases with increasing frequency. As a result, we have performed normalization to the measurement results with respect to source as follows: We have measured the AD of the field strength for the monopole in free space without any PC and then found the average value of the AD in the analyzed angular range (0°-180°) for each frequency. It is observed that, in the considered frequency range the variation in the average value of the AD of monopole in free space is highly correlated with the variation of the average AD of the measured field strength when the PC2, PC3 and PCD are used. Then, for the monopole which is measured in free space, we have found the least squares approximation (line fit) of the curve which represents the average value of the AD as a function of frequency. Finally for normalization, at each frequency, values of AD of the field strength measured with a PC structure is divided by the value of the line fit at the same frequency. Normalization of the measurements with respect to the measurement of the monopole in free space carried out for PC2, PC3 and PCD. Whereas, for the line source simulated in free space, variation in the radiation is negligible in the angular and frequency range. As a result, no normalization is needed in the simulation results.

At each frequency, the strength of the radiated signal is plotted in the Radiation Graph (RG) as a function of the observation angle (ψ) in Fig. 4.3 for the simulated and measured cases. By polar-plotting a cross section at a fixed frequency (a/λ), the RG is used to extract the AD at that frequency. As a result, the values on the horizontal axis to which the peak values correspond, indicate the

angular directions where the directive radiation occurs. The values in the RG are scaled such that the maximum value in the RG corresponds to 1 in both the simulations and the measurements to provide convenience in the radiation pattern comparison.

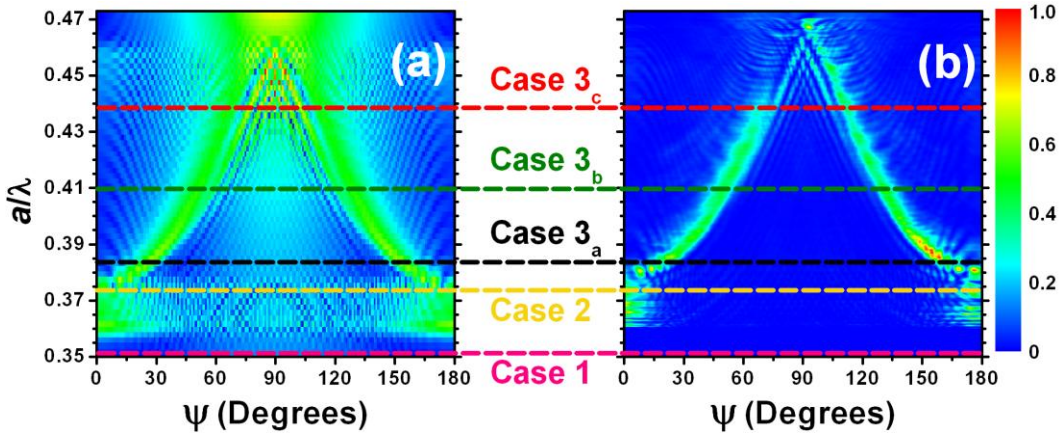

Figure 4.3: RG for the PCD obtained by FDTD simulation (a), and by measurement (b). Dashed lines represent the sample frequencies further investigated (magenta for Case 1, yellow for Case 2, black, green, and red for Cases3a, b, c, respectively). For each case, a polar plot of the radiation pattern is provided. Comparing Fig. 4.3(a) to Fig 4.3(b), the discrepancies (i.e., non-symmetric appearance especially at high frequencies) in the measurement RG are attributed to the artifacts of the manufactured PCD and to the non ideal amplitude and frequency (i.e., non-uniform AD) characteristics of the monopole source.

Three different cases will be of interest for us, whose distinction is made in terms of frequency ranges, based on what is observed in the dispersion diagram (Fig. 4.2) and in the RG of PCD (Fig. 4.3).

Case 1: The frequency range **$0.339<a/\lambda<0.359$** (10.59-11.22GHz) starts from the lower band edge and extends up to the lower-frequency tail of the dimer-layer mode shown in Fig. 4.2. These frequencies reside in the PC and PCD stopband and do not couple to the dimer-layer mode unless the frequency is too close to the minimum frequency of the dimer-layer mode. The AD plots of radiated field for the three configurations (PC2, PC3, and PCD) are drawn in Fig.

4.4 at the frequency a/λ=0.353. Although Figure 4.3 predicts no significant radiation for any angle at this frequency, Fig. 4.4 is given in order to make a fair and consistent comparison between the investigated structures. Irregularities in the measurement results arise from the low power radiation levels. In all of the three configurations, radiation around $\psi=90^{o}$ is observed because either there are no rods in front of the source to prevent radiation (for PC2) or because of the poor filtering capability of a single layer of dielectric rods that is placed in front of the source (for PC3 and PCD). In Case 1, surface states are not excited so that propagation along the dimer-layer is negligible unless the frequency is close to the dimer-layer mode frequencies. Fig. 4.4(a) shows that at a/λ=0.353 a small radiation in the region ψ=0° and ψ=180° occurs for the PCD. This results from the minor surface propagation due to the weak excitation of the mode represented by the lower-frequency tail of the dimer-layer mode starting at a/λ=0.359 (Fig. 4.2). Moreover, in the PCD case the same minor surface propagation is the reason for the high frequency oscillations shown in Fig. 4.4(a). This issue is going to be clearer after the discussion of surface modes and surface propagation in Case 2.

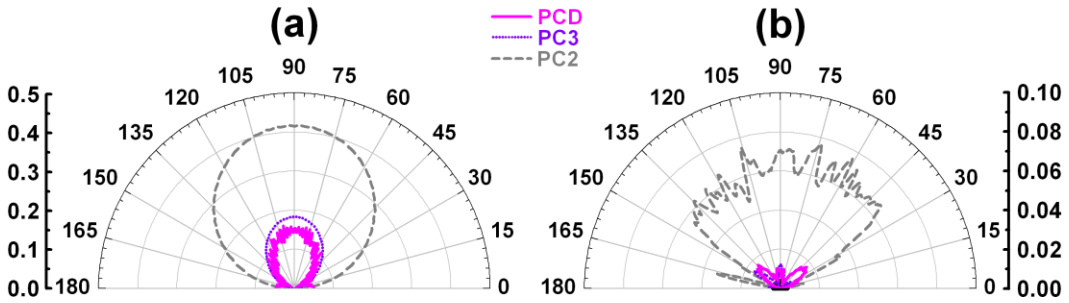

Figure 4.4: Normalized angular field distribution for Case 1 at a/λ=0.353. (a) Simulation results obtained from the RG in Fig. 4.3(a) (b) Measurement results obtained from the RG in Fig. 4.3(b).

Case 2 (the guided mode): The field excited by the source couples to the dimer-layer mode of the PCD, in the frequency region **0.359<*a*/λ<0.380** (11.22-11.88GHz). Below the light line (Fig. 4.2), the parallel wavenumber of the surface modes $k_{//}$ along the *x*-direction, parallel to the surface of the dimer-layer, is larger than the free space wavenumber k_0. In this case, wave propagation along the dimer-layer is allowed and the power is propagating at grazing angle ($\psi=0^o$ and $\psi=180^o$) since in this case $k_0 \approx k_{//}$ (but still $k_{//} > k_0$), without significant radiation occurring off the dimer-layer surface. In this case, power is emitted also by the truncation-ends of the structure toward the ±*x* directions. Indeed, at an operation frequency of $a/\lambda=0.373$ (indicated by the yellow dashed line in Fig. 4.3(b)), the radiation main lobes are close to $\psi=0°$ and $\psi=180°$ (Fig. 4.5). Observation of the measured and simulated results implies the existence of guided waves along the surface, which was observed in Fig. 4.2.

The oscillatory appearance in the radiation pattern is caused by the interference of the significant power coming out of the two edge-truncations because of the finite length (along *x*) of the PCD. In other words, the two ends of the PCD, excited by the left and right traveling modes produced by the source, act like distinct radiating sources in addition to the direct source-field arising from the center. This situation was mentioned in discussion of Case 1 regarding the oscillations and lobes at grazing angle in the AD of PCD seen in Fig. 4.4(a). Since the operation frequency is still in the PC stop band, the angular field distributions relative to PC2 and PC3 do not exhibit any beaming produced by excitation of modes, which has been also similarly shown for Case 1.

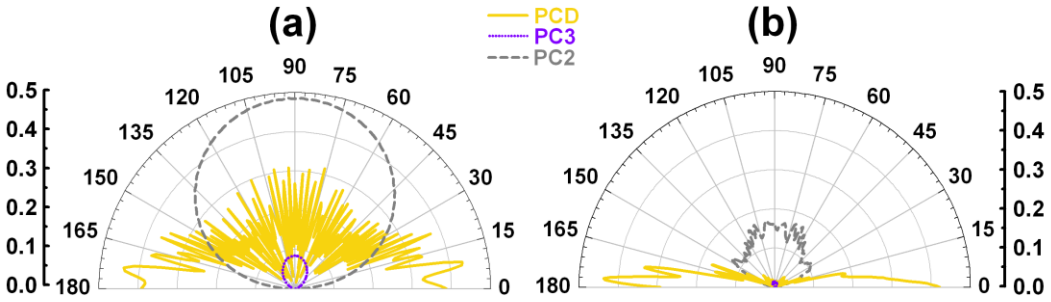

Figure 4.5: Normalized angular field distribution for Case 2 at a/λ=0.373. (a) Simulation results obtained from the RG in Fig. 4.3(a). (b) Measurement results obtained from the RG in Fig. 4.3(b).

Case 3 (the leaky mode): Frequencies higher than a/λ**=0.380 (**11.88GHz) are the main focus of this study. At this frequency, the dimer mode crosses the light line (Fig. 4.2). Under this case, we make two propositions regarding the modes: **P1)** The wavenumber $k_{//}$ possesses an imaginary part (i.e., $k_{//}$ is not purely real) when the real part of $k_{//} < k_0$ (the region above the light line), as implied by the leaky wave theory [62]. **P2)** The curve representing the real part of propagation constant of the mode in the dimer-layer still has negative slope above the light line. Hence, the mode has a negative group velocity ($v_g = d\omega/dk < 0$). A complex mode analysis will be carried out in a future study. Nevertheless, the following observations establish a strong base for our propositions concerning Case 3. Beyond a/λ=0.380, above the light line, $k_{//}$ (we should say the real part of $k_{//}$) is smaller than k_0. The complex part of $k_{//}$ is responsible for the radiation into the space above, on the right and left hand side of the PCD. Consequently, it is possible to attain two directive beams, at angles equal to ψ and (180^o -ψ), as shown in Fig. 4.6. Since $k_{//}$ is decreasing when frequency increases, as a result of the situation mentioned in P2, the radiation angle approaches broadside, $\psi = 90°$, as the frequency increases beyond a/λ=0.380. This behavior can be observed in Fig. 4.3 and Fig. 4.6. The PCD structure transfers power into the space above in small increments contributed discretely from each dimer and the PCD behaves like a leaky wave antenna [70]. The evanescent wave (we recall that $k_{//}$ has a complex

value) attenuates while propagating toward the two lateral truncation-ends of the PCD. Therefore, since most of the surface power is radiated (leaked) into the space above, only a small portion reaches the two truncation-ends of the PCD. Therefore, the oscillations in the radiation pattern that were caused by the radiation of the two truncation-ends of PCD in Case 2 are now not present. In Fig. 4.6(a), the far field radiation patterns are simulated by employing the far field option of the Rsoft Fullwave software. The measurement results (Fig. 4.6(b)) obtained at a distance of 1m are compared to the far field simulation results. The radiation patterns tend to smooth out in the far field. Moreover, the far field patterns turn out to have narrower angular beamwidths. Nonetheless, measurements performed at a distance of 1m are sufficient to offer estimates of the far field antenna behavior. The far field condition (measurement distance > $2d^2/\lambda$) given in [71] suggests the measurements being carried out at a distance of at least 20 m to obtain the approximate far field distribution. Here d=0.5m is the effective aperture of the antenna and λ=2.34cm is the wavelength corresponding to a/λ=0.41 which is an average value in the operation range. As a note, although the length of the PCD approximates 1m, the length of the effective aperture of the PCD which is responsible for the directive beam in a single quadrant covers only 0.5m, which is the length of the half section of the PCD structure. This issue will be clear when the PC with halved dimer-layer is studied in Section 2.3. The fact that for increasing frequency the beam scans toward the broadside direction (ψ= 90°) indicates that the leaky wave responsible for the directive radiation has a backward nature [62]. This is confirmed by the next experimental setup.

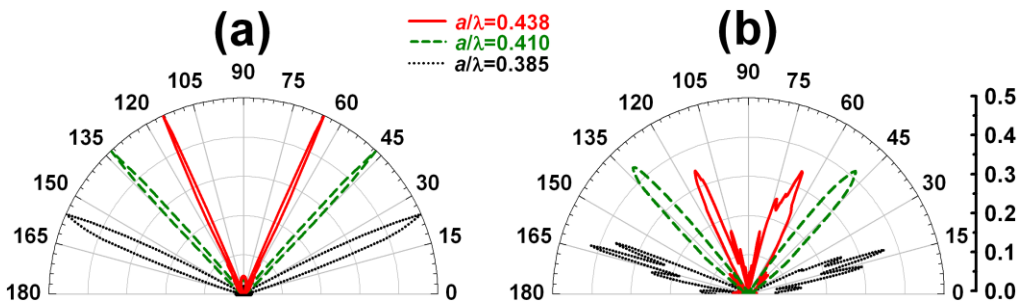

Figure 4.6: Angular field distribution for Case 3_{abc} (shown in Fig. 4.3) at frequencies a/λ=0.385 (black dotted line for Case 3_a), a/λ=0.410 (green dashed line for Case 3_b), and a/λ=0.438 (red solid line for Case 3_c). (a) Simulation results for the "far field" radiation pattern which are performed by Rsoft Fullwave software (previously, the simulation RG evaluated at 1m from the center was given in Fig. 4.3(a)). (b) Measurement results from the RG in Fig. 4.3(b). This shows that measurements performed at 1m provide an estimate of the far field radiation pattern.

Calculated mode profiles of the electric field $|E_y|$ in the XZ plane are shown in Fig. 4.7 (with linear scale in arbitrary units) for the same input level of line source at two different frequencies. The excitation source is located between the dimer-layer and PC2, as depicted in Fig. 4.1(a), and here recognized by the strong field intensity at x=0mm, z=5mm. The mode profile in Fig. 4.7(a) confirms the presence of surface propagation at a/λ=0.373 that we have described in Case 2. Since there is not significant attenuation while propagating along the x-direction, most of the power reaches the two PCD truncation-ends. On the other hand, in Fig. 4.7(b), at a/λ=0.41 the guided (leaky) wave is attenuated while it propagates along the x-direction (we recall that in this case the real part of $k_{//}$ is smaller than k_0), and only a very small amount of power reaches the two PCD truncation-ends. Because of their attenuation properties, leaky waves are not permitted to cover a long distance, which shows the appropriateness of P1 in Case 3. In Fig. 4.7(c), the cross sections of the mode profiles are given, which are taken along x-direction passing through the center of the dimers to provide a quantitative comparison. It is seen that for a/λ=0.373, energy is transferred towards the ends whereas for a/λ=0.410

the signal is decreasing along the *x*-direction since energy is radiated into space above the dimer layer.

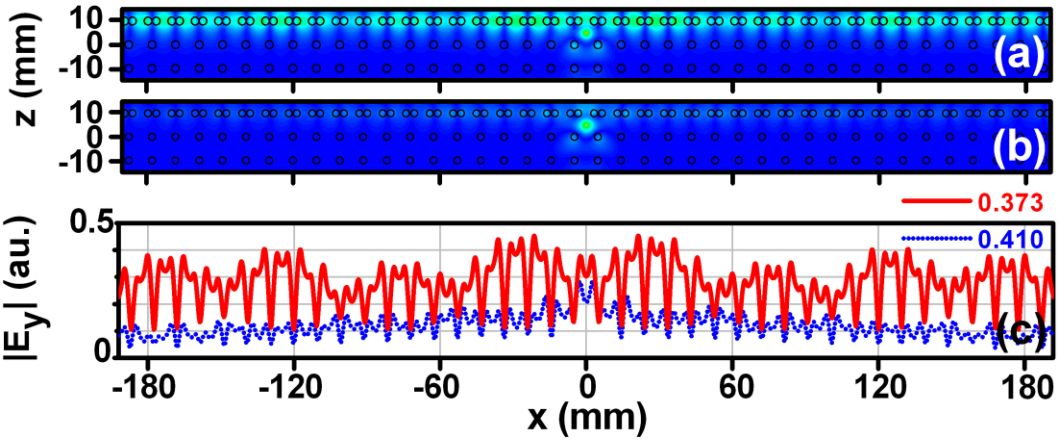

Figure 4.7: Calculated mode field profile for Case 2 and Case 3. (a) Case 2: the surface wave (guided) frequency is a/λ=0.373, (b) Case 3: the radiative (leaky wave) frequency is a/λ=0.41. (c) Cross sections of the mode profiles (Figs. 4.7(a) and 4.7(b)) taken along *x*-direction passing through the center of the dimers are plotted in the same arbitrary units which is used in Fig. 4.4(a) and Fig 4.5(a).

4.5. Backward wave character and radiation property of the leaky mode excited in the dimer-layer

We have already mentioned in our second proposition (**P2**) that Case 3 supports backward waves (with phase and group velocity traveling along opposite directions). This means that the radiative phenomenon exhibits an interesting property. That is, the guided leaky wave with a negative phase velocity in the – (+) *x* direction (and positive group velocity, since power is emanated by the source in both the ± *x* directions) is responsible for the directional beaming in the 1^{st} (2^{nd}) quadrant of the polar plot. The dimer pairs on the left (right) hand side of the XZ plane act like elements of an array antenna and the cumulative interference

provides the directive beaming in the range of $0° < \psi < \sim 70°$ for the 1st ($180° > (180°-\psi) > \sim 110°$ in the 2nd) quadrant. This situation is typical of backward leaky wave radiation and it has been used in several metamaterial-based leaky wave antennas, as in [72], operating in the microwave range. It can be explained with the backward nature of the field propagating along the ± *x* directions, and to clearly show this we analyze the radiation by a halved dimer-layer configuration shown in Fig. 4.8.

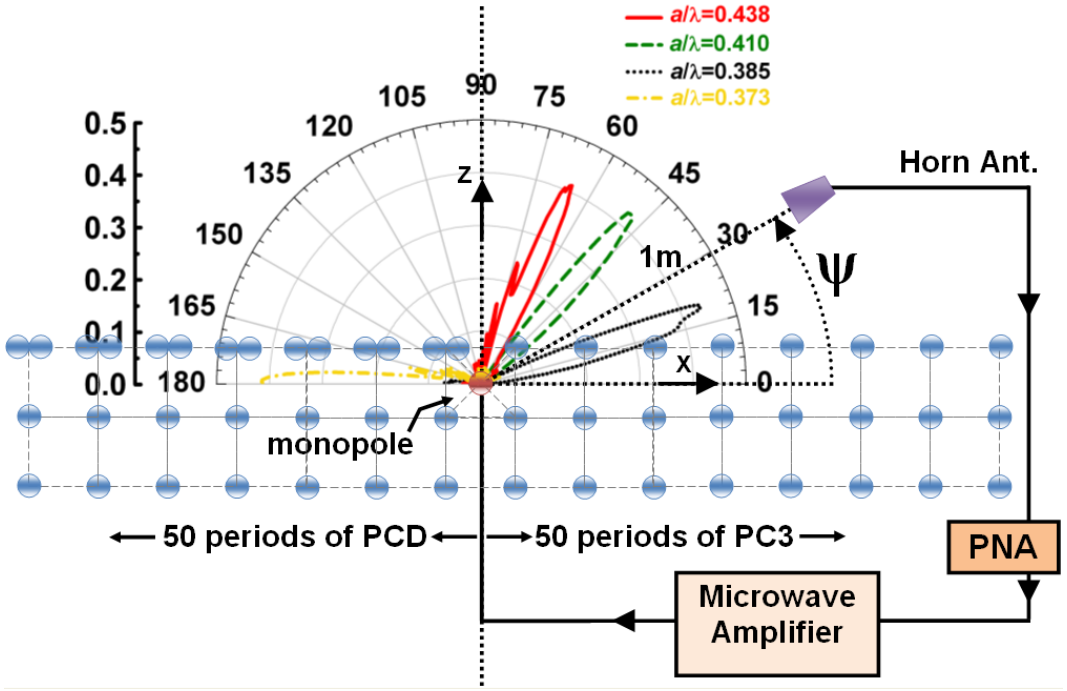

Figure 4.8: The experimental setup for PCHD and the normalized AD measurement. The angular field distribution is measured at a distance of 1m at frequencies of a/λ=0.373 (yellow dash-dotted line) which is the guiding frequency, and at the beaming frequencies which are a/λ=0.385 (black dotted line), a/λ=0.410 (green dashed line), a/λ=0.438 (red solid line).

The PC with a halved dimer-layer (PCHD) is very similar to the PCD except for the fact that dimer pairs for $x > 0$ are replaced by single rods. Therefore, the new configuration resembles PC3 for $x > 0$. Surface and leaky waves are able

to propagate only towards the –*x* direction while PC3 will not allow propagation in the +*x* direction. The experimental setup and the measured radiation patterns for three separate frequencies (belonging to Case 3) are depicted together in Fig. 4.8.

The corresponding RG for the PCHD is shown in Fig. 4.9. As it was stated for the PCD, no radiation is observed for **0.294<*a*/λ<0.359.** Accordingly, in the range **0.359<*a*/λ<0.380** the dimer-layer supports the surface mode. As a result, for ***a*/λ=0.373,** the radiation is observed only at ψ = 180° whereas no significant field is measured near ψ=0° or other angular directions. This is consistent with our earlier claims concerning Case 2.

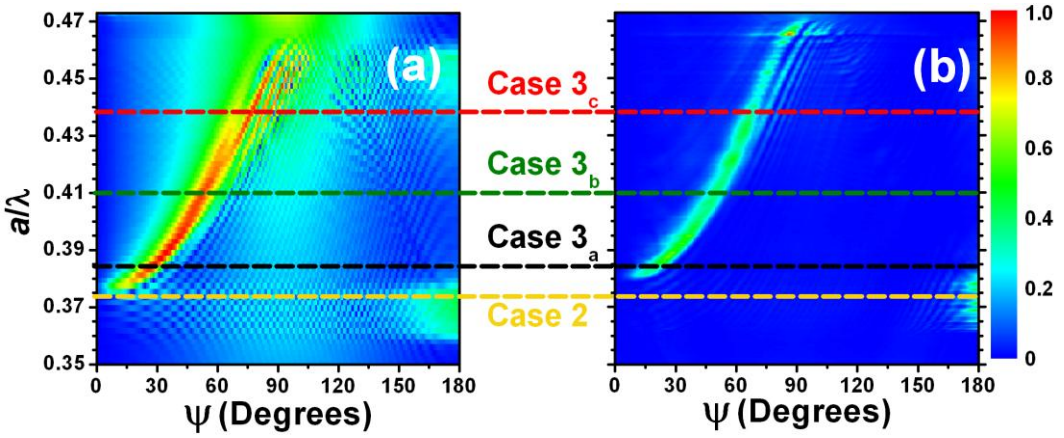

Figure 4.9: Radiation Graph for the PC with a halved dimer-layer. (a) Simulation, (b) Experimental result (yellow for Case 2, black, green, and red for Case 3a,b,c). The cross sections that are indicated by black, green, and red and yellow dashed lines are plotted in Fig. 4.8.

Finally, above the light line, at higher frequencies, we observe radiation only in the 1st quadrant while the leaky wave propagation takes place in –*x* direction. We notice that as the frequency is increased, the radiation angle gets closer to 90° (broadside), which is the opposite of what happens to leaky wave working in the forward regime. These observations demonstrate the backward characteristics (i.e., opposite signs of phase and group velocities) of the radiation from the dimer-layer. They also confirm our prior understanding regarding the

radiation phenomena for Case 3. It is also revealed that the effective aperture of PCHD (and PCD) is 0.5m (i.e., length of the dimer layer remaining at either side of the source) although the length of both structures is almost 1m.

Chapter 5

Metamaterial based cavities

5.1. Introduction

One of the important concepts in the physics of PCs is related to field localization on defects. In solid-state physics the idea of localization is associated with disorder that breaks the translational invariance of a crystal lattice and supports spatially localized modes with the frequency outside the phonon bands. A similar concept is well known in the physics of PCs in which an isolated defect (a region of different refractive index that breaks periodicity) is known to support a localized defect mode. An array of such defects creates a waveguide that allows directed light transmission for the frequencies inside the band gap. From the viewpoint of possible practical applications spatially localized states in optics can be associated with different types of all optical switching devices in which light manipulates and controls light itself owing to the varying input intensity. Photonic crystal defects have many important applications such as thresholdless semiconductor lasers [73] and single-mode light-emitting diodes [74].

Recently, periodically arranged metallic thin wires and Split Ring Resonator (SRRs) structures have attracted much attention in the scientific community. Material responses could be extended to the values that are not readily available with these artificial materials, since they are also called as metamaterials.

This type of artificial materials can provide negative permittivity and permeability over a certain frequency range.

EM waves cannot propagate in the negative μ or negative ε medium. Therefore, metamaterials exhibit a gap in the spectrum for the negative ε or μ region. Hence, it is possible to obtain highly localized cavity modes inside the stop band by introducing a defect into the structure, which is similar to the defect modes in PCs. However, defect structures in metamaterials have not investigated.

In this chapter, we investigate cavity formation in SRR and Composite Metamaterial (CMM) structures. We first introduce negative permittivity and permeability. Subsequently, we introduce the cavity structure and present the transmission of the SRR cavity and CMM cavity structures. Our results show that the modification of a unit cell of the metamaterial can exhibit a cavity resonance. We also show that the cavity formation in the metamaterials leads to the localization of the field within a subwavelength region and reduce the effective group velocity. Subsequently, we brought two and three cavities together in which we investigated the transmission spectrum of metamaterial based 2-cavity and 3-cavity systems.

5.2. Negative Permittivity and Permeability

The response of any material to EM waves is determined by two parameters: dielectric permittivity (ε) and magnetic permeability (μ). Generally, μ of naturally occurring materials is positive. Four decades ago, Veselago [75] proposed that artificially constructed materials can enable the negative values of ε and μ, since there are no restrictions with the laws of electromagnetism. In this pioneering study, Veselago predicted that via artificially constructed materials, along with simultaneously negative ε and μ, difficulty in obtaining negative refraction, reverse Doppler shift, and backward Cherenkov radiation can all be overcome. However, obtaining a simultaneously negative ε and μ and, therefore, a negative index of refraction is a significant challenge.

The EM response is dominated by negative permittivity concept in the visible and UV frequency regions. However, at lower frequencies starting from the near infrared and downwards, dissipation asserts itself, therefore dielectric function becomes imaginary. To achieve negative permittivity values at microwave range, the thin metallic wire concept is proposed [76-78].

By assembling thin metallic wire structures into a periodic medium with appropriate parameters, negative permittivity can easily be achieved at microwave frequencies. Plasma frequency of the thin metallic wires is given after detailed calculations as [76]:

$$\omega_p^2 = \frac{ne^2}{\varepsilon_0 m_{eff}} = \frac{2\pi c_0^2}{a^2 \ln(a/r)} \tag{5.1}$$

where c_0 is the speed of light in free space, a is the lattice parameter and r is the radius of the wires.

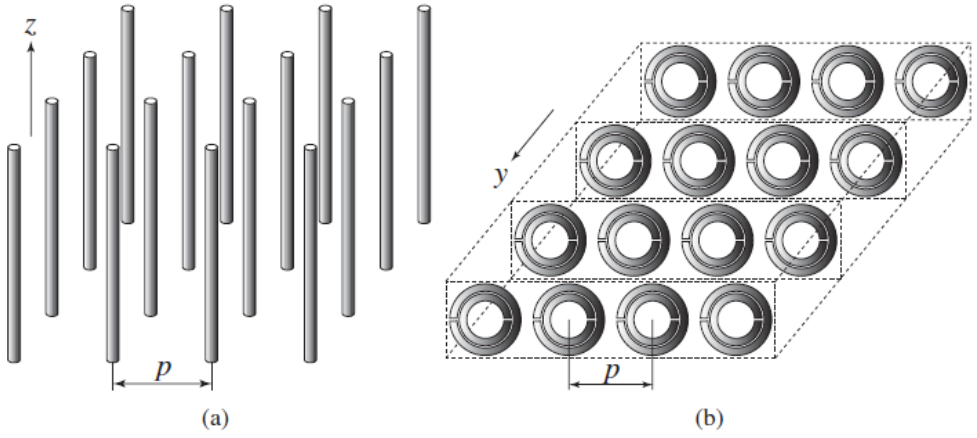

Figure 5.1: First metamaterials, constituted only by standard metals and dielectrics, proposed by Pendry. (a) Thin-wire structure exhibiting negative ε and positive μ if E//z. (b) SRR structure exhibiting positive ε and negative μ if H⊥y.

In the thin wire case, the effective medium theory holds since corresponding λ for ω_p is much larger than the radius of the wires. Therefore, an effective dielectric permittivity, ε_{eff} can be used to define the permittivity of the medium. As far as external EM radiation is concerned, a thin wire structure appears as an effectively homogeneous dielectric medium whose internal structure is only apparent as it dictates ε_{eff}.

Metallic thin wires arranged periodically are good candidates for a negative ε medium, because this structure exhibits a plasma frequency below which the material is opaque [77].

Because of the lack of magnetic charge analogous to an electric charge, it is more difficult to obtain a material with negative magnetic permeability. To obtain negative permeability, one has to extend the magnetic properties of the materials.

While several researchers proposed different structures for the purpose of negative permeability, probably the most common feature of these structures is the fact that they are based on resonance phenomena. Simply put, in order to have magnetic response, the underlying elements need to have non-zero magnetic dipole moment. But, it is well-known that the magnetic response of naturally occurring materials is small at high frequencies. This suggests that we cannot make use of the magnetic dipole moment of the molecules or atoms. Hence, we need to create our magnetic dipoles. A current carrying loop has a magnetic dipole moment. As a matter of fact, a medium composed of small conducting rings is diamagnetic; a simple result of the Lenz Law. A comparison with the effective dielectric response of a medium that is composed of harmonic oscillators provides the necessary clue.

In 1999, Pendry *et al.* introduced several configurations of conducting scattering elements displaying a magnetic response to an applied EM field when grouped into an interacting periodic array [79]. The resonant behavior of SRRs is due to the capacitive elements (gaps and splits), which in turn results in rather high

positive and negative values of permeability near the magnetic resonance frequency (ω_m).

Figure 5.1 shows the design of Pendry, described as a SRR. In a SRR, there are two rings both having a split. By having splits in the rings, the SRR unit can be made resonant at wavelengths much larger than the diameter of the rings. The purpose of the second split ring, inside and whose split is oriented oppositely to the outside split, is to generate a large capacitance in the small gap region. The gap between the rings prevents current from flowing around any one ring. However, there is a considerable capacitance between the two rings, which enables current to flow.

5.3. Split Ring Resonator structure

The SRR structure that we used for the present study was a one-dimensional periodic arrangement of square rings. The structures were printed on a Teflon substrate with ε=2.17, in which the thickness of the substrate was 1 mm. The thickness of the copper was 0.05 mm. The width of the wire stripes was 1.6 mm. The lattice constant along the x direction (propagation direction) was 4.95 mm. The height of the structure was 40 unit cells. 30 layers of the structures were stacked with a 2 mm period along the z direction. The E-field was in the y direction. A schematic drawing of SRR can be seen in Fig. 5.2(a).

The experimental setup consists of an HP 8510C network analyzer and two standard gain horn antennae in order to measure the transmission amplitude. We also performed simulations to check the experimental results. Simulations are performed by using commercial software, CST Microwave Studio which is a 3D full-wave solver, employing the finite integration technique (FIT). In order to determine the resonance frequencies of the structures under consideration, we have included one layer of the SRR structures along the propagation direction. In the simulation setup, the structures are subjected to an incident plane wave. Open boundary conditions are employed along the propagation direction. Periodic

boundary conditions are used along the directions other than the propagation direction. Hence, the structure is assumed to be periodic and infinite along the directions that are perpendicular to the propagation direction. The transmission amplitudes are obtained by measuring the fields at a distant point from the structures. This point was chosen such that beyond this point the transmission coefficients do not change with the increasing distance. Such a choice was made to exclude the near-field effects due to the highly resonant nature of the structures under consideration.

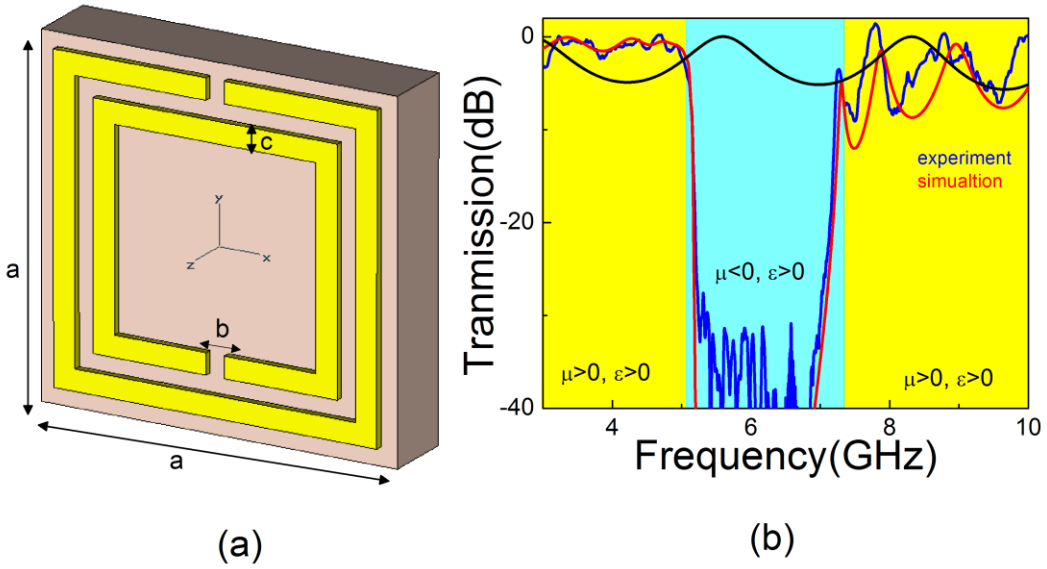

Figure 5.2: (a) The unit cell of the SRR structure: a=4.95 mm, b=0.25 mm and c=0.25mm. (b) The SRR structure has a bandgap between 5 and 7 GHz. However, the CRR structure transmits EM waves (black curve). Hence, the SRR structure exhibits $\mu<0$ medium at these frequencies.

The measured transmission demonstrated that the SRR structure has a band gap from 5 to 7 GHz (Fig. 5.2(b)). However, the closed-ring resonator (CRR) structure, which was obtained by closing the splits in the rings, transmitted EM waves at these frequencies. Therefore, this gap is due to the magnetic resonance

[80], in which the SRR structure exhibits a negative μ medium. When the EM field passes through the ring, an induced current is created, in which the generated field is perpendicular to the magnetic field of the light. The magnetic resonance results in a negative μ. EM waves cannot propagate in the negative μ medium and possess a band gap in the spectrum. The splits in the SRRs structure play a key role in obtaining magnetic resonance. Removing the splits prevents the current from flowing between the inner and outer rings, and therefore, the magnetic resonance is no longer present.

Notice that the wavelength is 5.00 cm, whereas the length of the SRR structure is 4.95mm. Therefore, by employing the aforementioned SRR structure with sizes corresponding to the $1/10^{th}$ of free space wavelength, magnetic resonance can be obtained. The reason why SRR received a great amount of interest is not only because of being a source for negative permeability, but also for achieving resonance with subwavelength features. Therefore, an effective medium theory becomes applicable for SRR media.

Moreover, we calculated the effective ε and μ of the SRR structure by use of a retrieval procedure. The retrieval procedure is widely used to calculate the effective parameters of the metamaterials [81-87]. In this method, the real and imaginary parts of the refractive index, wave impedance, and, therefore, the real and imaginary parts of the ε and μ are retrieved from the amplitude and the phase information of the transmission and reflection. The details of the retrieval procedure that were used in this study are outlined in Ref. [81]. This particular method has the advantage of identifying the correct branch of the effective ε and μ. The ambiguity in the determination of the correct branch is resolved by the use of an analytic continuation procedure. There was one layer of the structure along the propagation direction in this calculation. We employed periodic boundary conditions along directions other than the propagation direction. Therefore, the simulation setup coincides with a slab of material that consists of a single layer. The effective ε and μ were derived from the transmission and reflection

coefficients. The calculated parameters show that the SRR structure possesses effective ε>0, μ<0 from 5.0 to 7.0 GHz (Fig. 5.3(a)). Near the resonance frequency of SRR (6.0 GHz), the form of permittivity deviates from the Drude model. The effective permeability possesses both positive and negative high values around the magnetic resonance frequency.

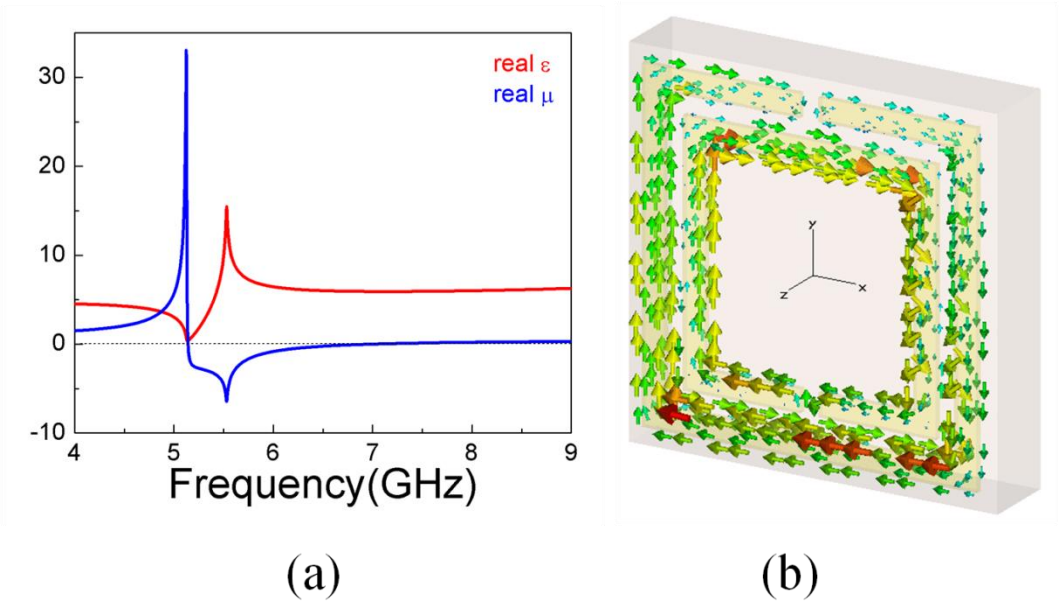

Figure 5.3: (a)The calculated effective ε and μ of the SRR structure by use of a retrieval procedure show that the SRR structure possesses effective ε>0, μ<0 from 5.0 to 7.0 GHz. (b) The calculated surface current density of the SRR structure at magnetic resonance frequency shows that the SRR structure behaves like a magnetic dipole.

We calculated surface current density of the SRR structure at magnetic resonance frequency. Figure 5.3(b) shows that the SRR structure behaves like a magnetic dipole.

5.4. Composite Metamaterial Structure

The metamaterial medium that we used in this study was composed of a 1D periodic arrangement of wire stripes and square SRR structures. The wire stripes were printed on the back of Teflon (ε=2.17) substrates, and the square SRR were printed on the front faces. The thickness of the Teflon substrate was 1mm. The unit cell of the Composite Metamaterial (CMM) structure is shown in Fig. 5.4(a). The width of the wire stripes was 1.6 mm.

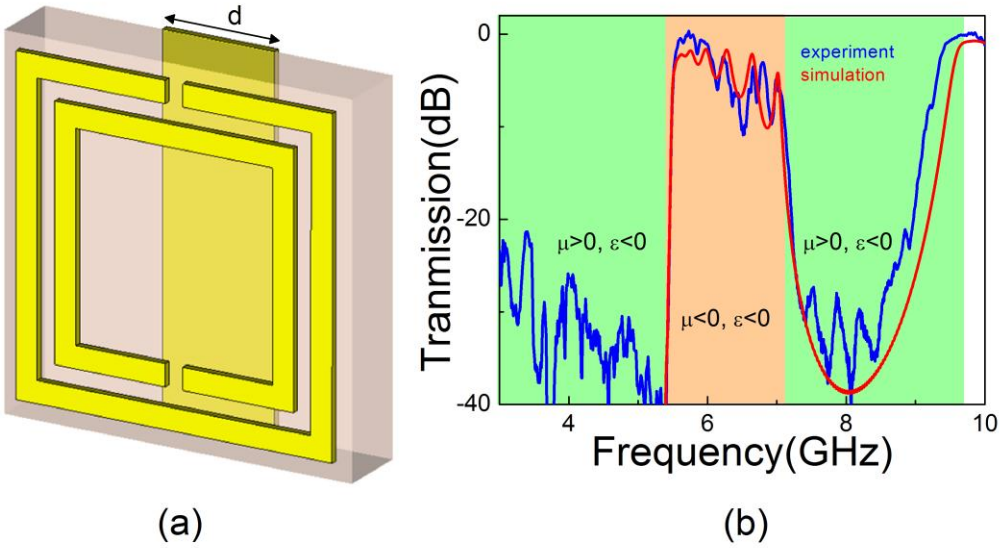

Figure 5.4: (a) Unit cell of the CMM structure: c=1.6 mm (b) The CMM structure transmits EM waves, because it has ε <0 and μ<0 between 5 and 7 GHz.

The measured transmission demonstrates that this CMM structure has a left-handed transmission peak from 5.5-7.0 GHz (Fig. 5.4(b)). The calculated transmission is in good agreement with the measured result. On the other hand, this CMM structure possesses a reflective medium from 7.0-9.4 GHz, or in other words, it has negative ε in this frequency region. In addition, calculated parameters

show that the CMM structure possesses effective $\varepsilon<0$, $\mu<0$ from 5.4 to 7.0 GHz and $\varepsilon<0$, $\mu>0$ from 7.0 to 9.4 GHz (Fig. 5.5).

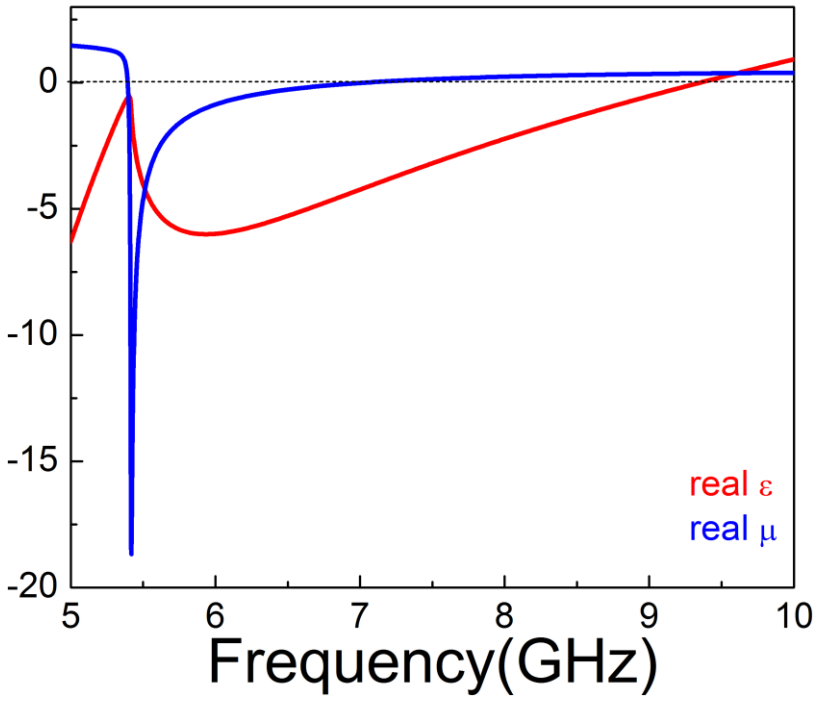

Figure 5.5: The calculated effective ε and μ of the SRR structure by use of a retrieval procedure show that the CMM structure possesses effective $\varepsilon<0$, $\mu<0$ from 5.4 to 7.0 GHz and $\varepsilon<0$, $\mu>0$ from 7.0 to 9.4 GHz.

5.5. Metamaterial based single cavity structure

It is possible to obtain a cavity mode in the forbidden transmission region of the SRR structure by introducing a defect in the structure. The translational symmetry of the negative μ or ε system can be broken by a positive μ medium. To break the symmetry of these periodic metamaterials, we changed the center unit cell of the structures by a closed-ring structure, which was placed on both sides of the board

and possessed positive ε and μ. The details regarding the unit cell of the cavity structure is shown in Fig. 5.6(a). Figure 5.6(b) shows the calculated effective parameters of the defect structure. The total single cavity system contains one cavity at the center and two metamaterial unit cells in each side of the cavity (1 cavity+4 metamaterial unit cells) in the propagation direction.

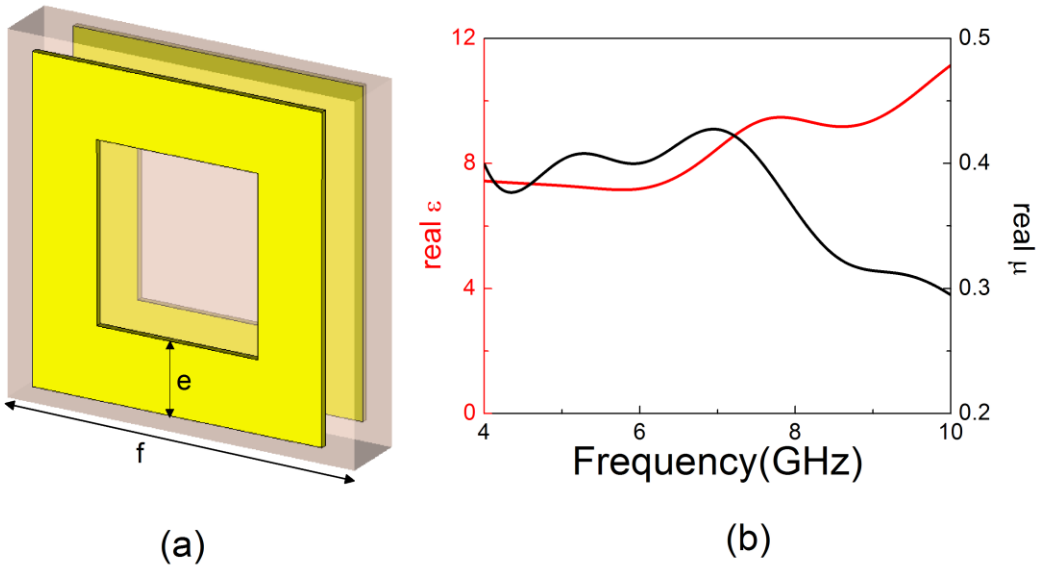

Figure 5.6: (a) Unit cell of the cavity structure: e=1 mm, f=5.4 mm. The unit cells of metamaterials are much smaller than the operating wavelength. (b) The calculated effective ε and μ of the cavity structure by use of a retrieval procedure.

This deformation in the SRR and CMM structures resulted in a cavity structure with a cavity resonance in the transmission spectrum. In Figs. 5.7(a) and 5.7(b) the transmission from the SRR cavity and CMM cavity structures are shown, respectively. The calculations agreed well with the experiments. We observed a cavity resonance with the *Q* factor (quality factor, defined as the center frequency, divided by the FWHM) of 192 at 6.7 GHz (44.7 mm) by the SRR cavity structure. The cavity resonance of the CMM structure was obtained at 7.5 GHz (40 mm) with a *Q* factor of 108.

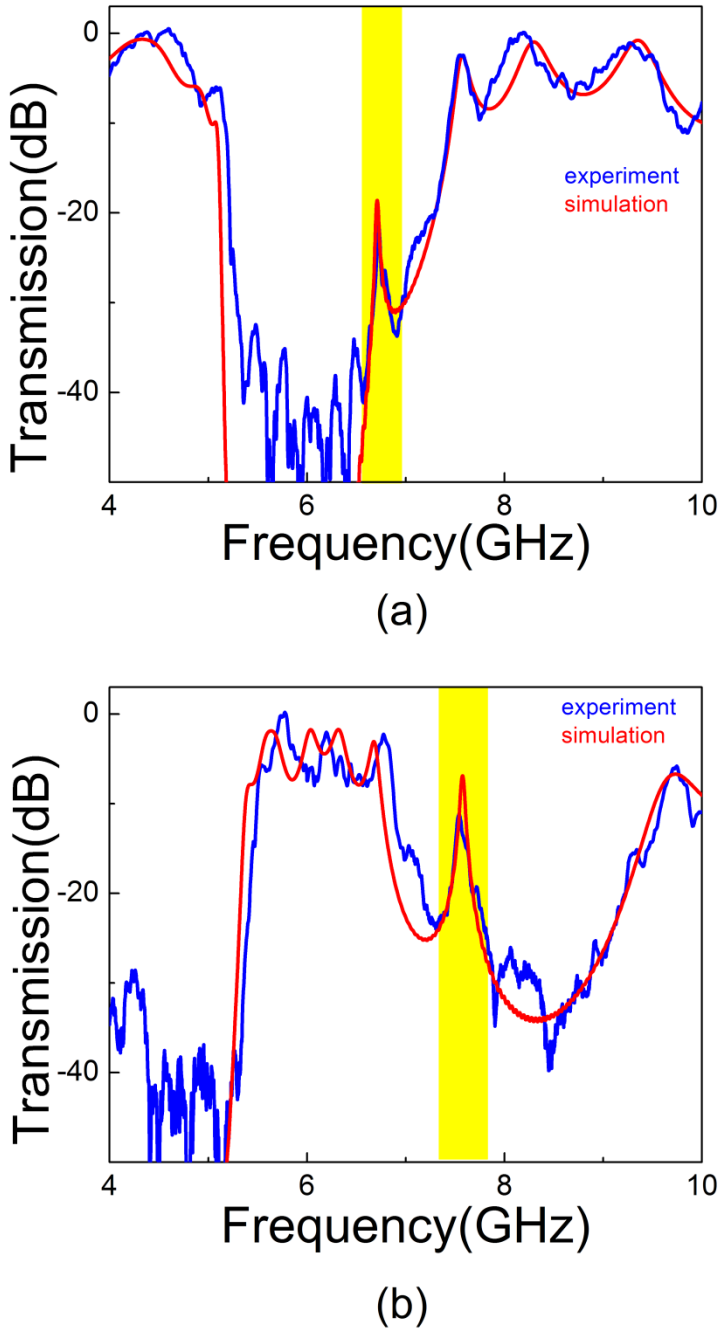

Figure 5.7: A cavity structure is introduced by replacing the center unit cell with a positive-index medium. The cavity resonance is observed at 6.7 GHz 44.7 mm and 7.5 GHz 40 mm by the (a) SRR cavity structure and (b) the CMM cavity structure, respectively.

Moreover, we calculated the transmissions for an SRR cavity structure without loss, with loss on board only, and loss on metal only. The results showed that the transmission at the cavity resonance is decreased because of the loss of the board and metal (Cu) (Fig. 5.8). The Q-factor for the SRR cavity resonance without a loss is 3290. On the other hand, the Q-factors are 1100 and 475 for the systems with loss on board only and with loss on metal only, respectively. Therefore, one can obtain metamaterial cavities with higher Q-factors by using different designs and materials.

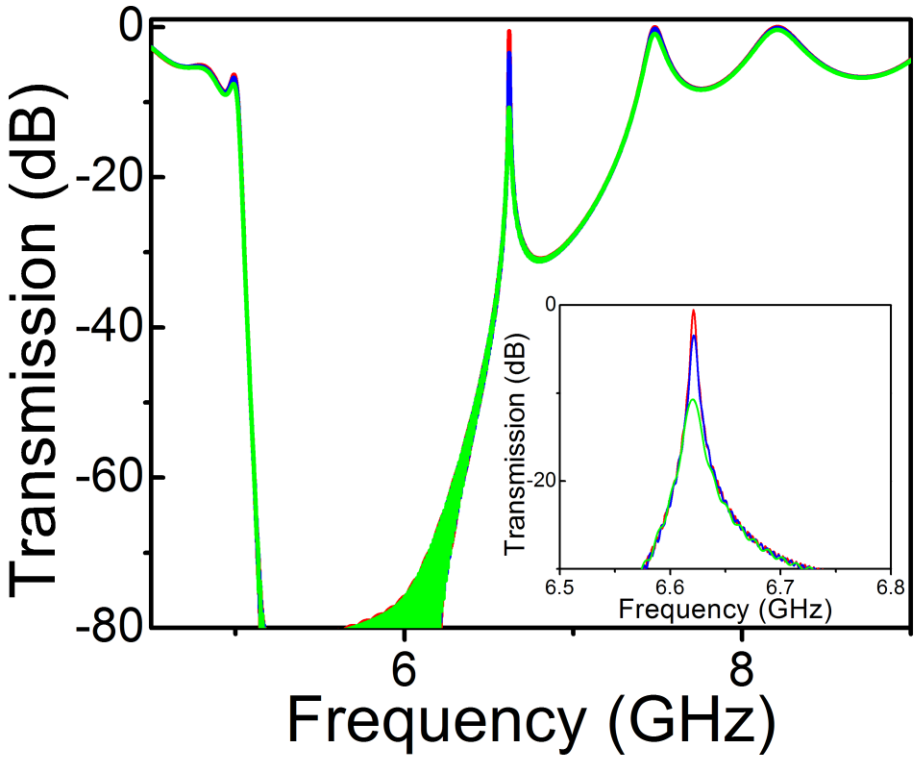

Figure 5.8: The calculated transmission for SRR cavity structure without loss (red line), with loss on board only (blue line), and with loss on metal only (green line). The calculated loss free transmission of the SRR cavity resonance possesses the highest Q-factor. It decreases if the losses of the materials have been introduced (inset: zoomed to the cavity resonance frequency).

The reflection of the SRR (CMM) structure is very high in the negative μ (ε) frequency range, and, therefore, the SRR (CMM) structures on both sides of the cavity behave like frequency-specific mirrors [88, 89]. The reflections of the EM waves between these two mirrors interfere constructively and destructively, giving rise to a standing wave pattern between the mirror surfaces, just like in Fabry-Perot resonances (FPRs). Any propagating light that is trapped between them will bounce back and forth between these two mirrors. Since the mirrors localize light within a finite region, the modes are quantized into discrete frequencies. The cavity resonance frequency depends on the geometry and size of the defects, as well as the geometry of the SRR and CMM.

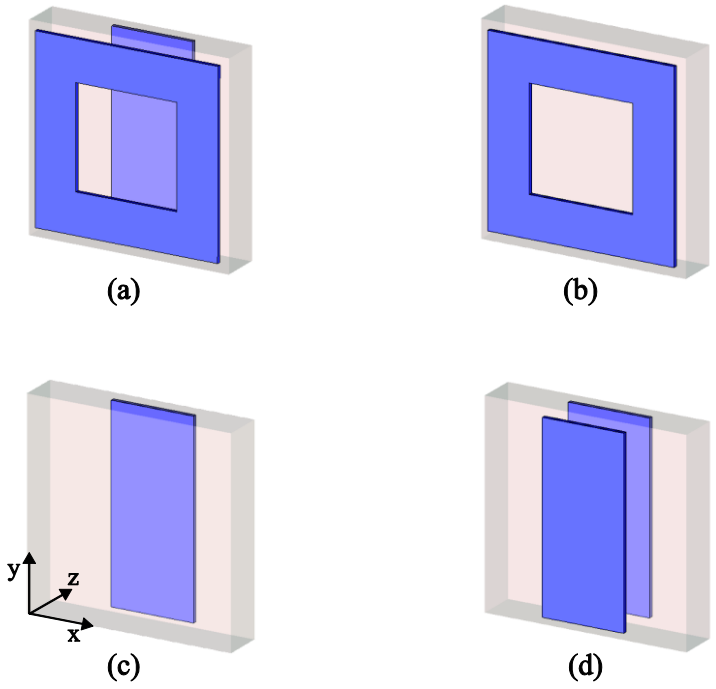

Figure 5.9: Four different defect structures used in this study: (a) D1: closed ring on the front side of the board and cut wire on the back side, (b) D2: closed ring only on the front side, (c) D3: cut wire only on the back side and, (d) D4: cut wire on both sides of the Teflon board. These defect structures were introduced in the center of the CMM structure. Therefore, there are four layers of a CMM structure in the forward and backward of the defect structures in the propagation direction.

We designed four different defect structures in order to investigate this issue. The defect structures are: (1) D1: closed ring on the front side of the board and cut wire on the back side, (2) D2: closed ring only on the front side, (3) D3: cut wire only on the back side and, (4) D4: cut wire on both sides of the Teflon board (Fig. 5.9). These defect structures are introduced in the center of the CMM structure.

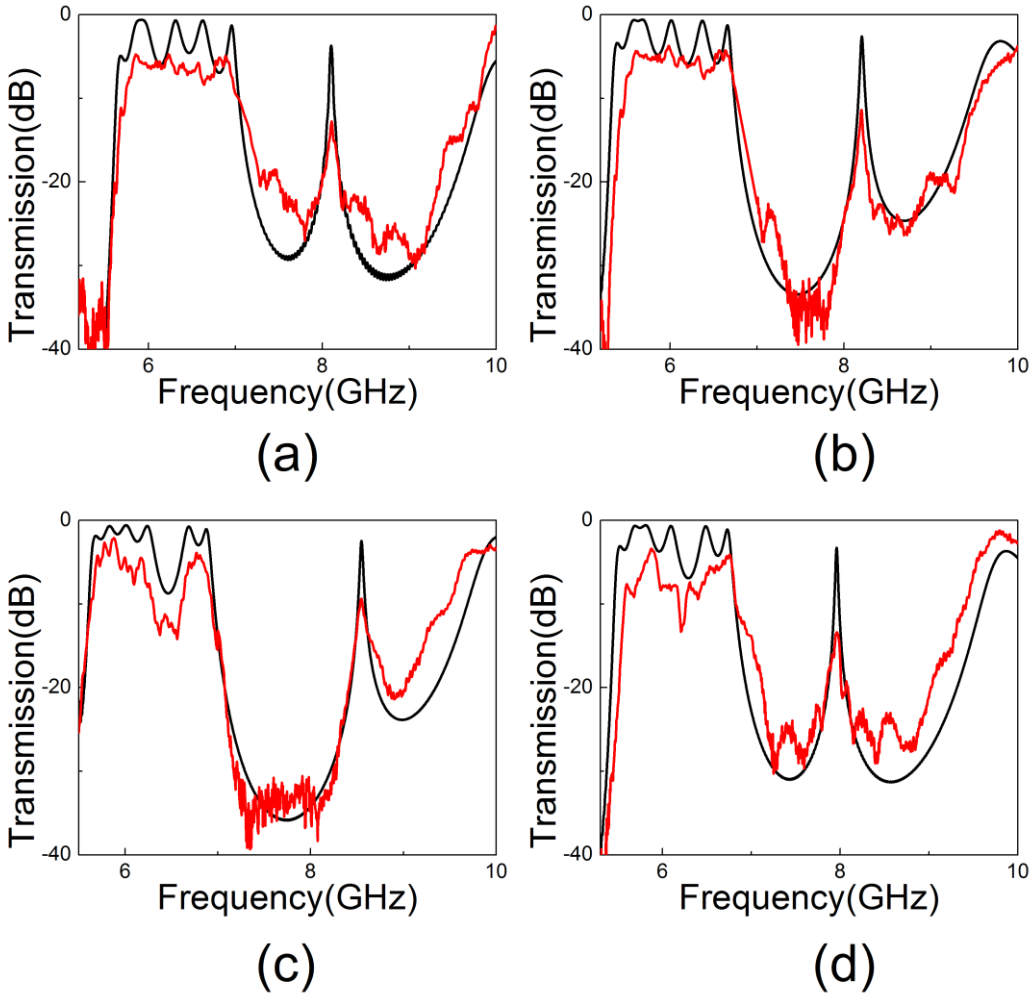

Figure 5.10: We observed cavity modes in the transmission spectrum of the CMM-based cavities (D1, D2, D3, and D4). The experiments (red line) are in good agreement with the CST Microwave calculations (black line). It is possible to design different CMM based cavity structures operating at different frequencies with different Q-factors.

We observed cavity modes in the transmission spectrum of the CMM-based cavities (Fig. 5.10). The experiments are in good agreement with calculations. All these defect structures allow a cavity mode in the transmission spectrum with different Q-factors (Table 5.1). Therefore, it is possible to design different CMM based cavity structures operating at different frequencies with different Q-factors.

	D1	D2	D3	D4
Frequency(GHz)	8.1	8.2	8.5	7.9
Q-factor	220	215	235	275

Table 5.1: Quality factors of the CMM based cavity structures

5.6. Subwavelength Localization

The calculated electric field distributions for the cavity structures show that the EM waves at the cavity resonance are trapped at the positive index region (Fig. 5.11). The length of the cavity is only $\lambda/8$, where λ is the cavity resonance wavelength. Hence, the field at the cavity resonance is enhanced at the subwavelength cavity region. Such a structure with enhanced EM fields can be used for several applications, including nonlinear optics [90]. Although it is possible to localize light into a subwavelength region with a regular FPR cavity, this localization is not smaller than $\lambda/2n$, where n is the refractive index of the dielectric gap. However, the phase dispersion properties of metamaterial-based cavity systems can be used to confine light into even smaller subwavelength dimensions.

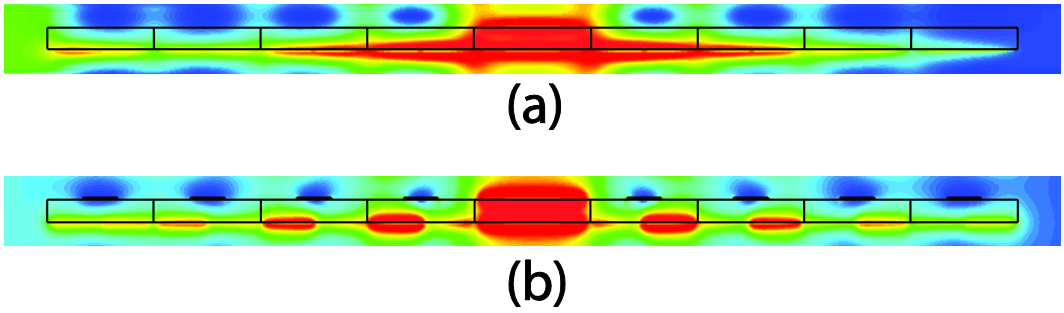

Figure 5.11: The calculated electric field is highly localized at the cavity region for (a) SRR cavity and (b) CMM cavity structures. Hence, the field at the cavity resonance is enhanced at the subwavelength λ/8 cavity region. (Red indicates the maximum, and blue indicates the minimum.)

5.7. Reduced Photon lifetime

A medium with a reduced group velocity, or in other words a medium with increased photon lifetime, offers a promising tool to increase the spontaneous emission rate and efficiency of nonlinear processes. Therefore, metamaterial based cavities with a controllable group velocity can bring significant advantages for optoelectronic devices.

The photon lifetime is defined as $\tau_p = \partial\varphi/\partial\omega$. Here, φ is the net phase difference between the phase of the EM waves propagating inside the structure and the phase of the EM waves propagating in free space for a total structure length. The photon lifetime corresponds to the propagation time of the EM waves inside the structure. The effective group velocity is inversely proportional to the photon lifetime and is defined as L/τ_p where L is the cavity length. The measured photon lifetime is 10 ns for SRR cavity structure and 3.3 ns for CMM cavity structure (Fig. 5.12). This also means that at the cavity resonance the effective group velocity is reduced by a factor of 67 for SRR cavity and 24 for CMM cavity when compared to the EM waves propagating in free space. The Q-factor and effective group velocity reduction factor are related through the localization of EM waves. It

is important to note that based on our experimental results, the lifetime is directly proportional to the quality factor via $\tau_p \alpha\ Q/\omega$.

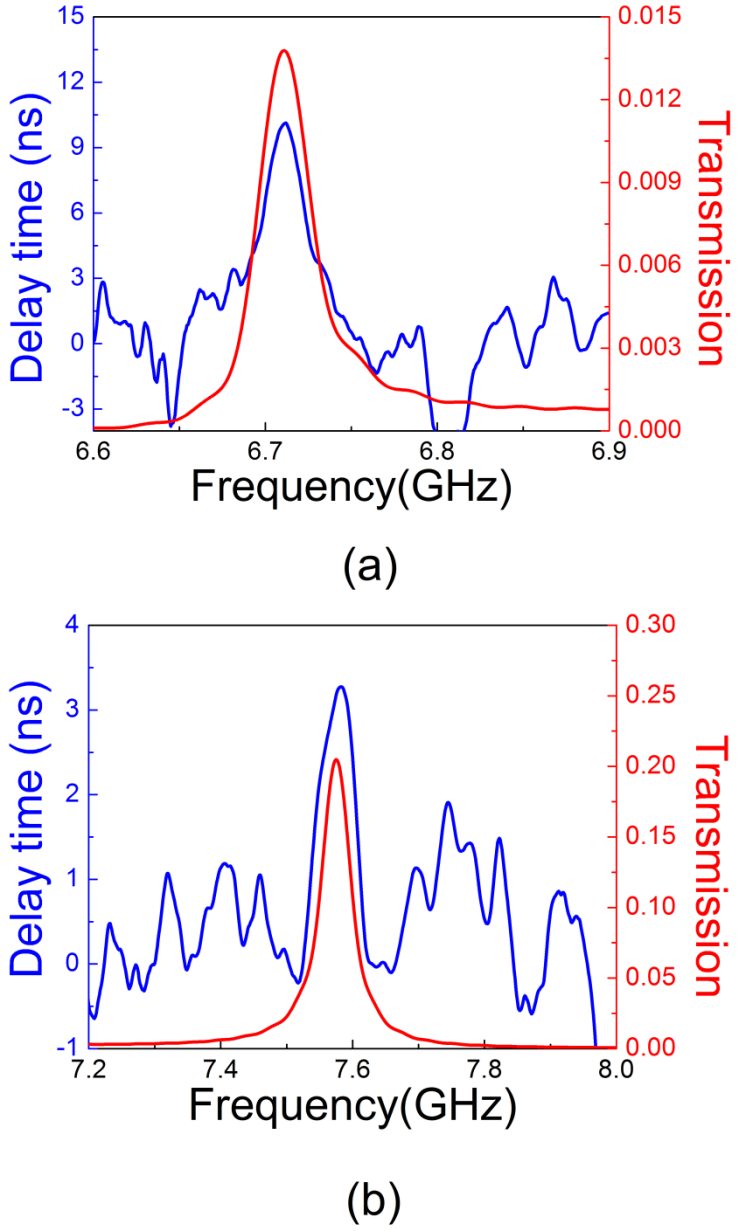

Figure 5.12: The measured photon lifetime is 10 ns for SRR cavity structure and 3.3 ns for CMM cavity structure. This also means that at the cavity resonance the effective group velocity is reduced by a factor of 67 for SRR cavity and 24 for CMM cavity when compared to the EM waves propagating in free space.

5.8. 1D Fabry Perot resonator model

As mentioned in section 5.3, one of the important properties of the metamaterial is to have a unit cell much smaller than the operating wavelength. Therefore, the metamaterials can be treated as a homogeneous medium with effective refractive index.

In this section, we model our metamaterial cavity system based on the information from the retrieval procedure and transmission spectrum as 1D FPRs with subwavelength cavity region at the center (Fig. 5.13(a)). By taking the full advantage of this FPR model, we calculated the transmission from the CMM based cavity structure using 1D transfer matrix method (TMM) [91, 92]. In the TMM calculations, we used effective ε and μ determined by use of retrieval procedure and Fresnel coefficients (reflection coefficient and transmission coefficient) for an interface when one of the two media is left-handed [93, 94].

The reflection and transmission coefficients for parallel polarization (*E* parallel to the plane of incidence, also called E, TM_z, *p*) and perpendicular polarization (*E* perpendicular to the plane of incidence, also called H, TE_z, *s*) are given, by [94]:

$$R_{//} = \frac{\varepsilon_{r1}k_{2z} - \varepsilon_{r2}k_{1z}}{\varepsilon_{r1}k_{2z} + \varepsilon_{r2}k_{1z}} = \frac{n_2\cos\theta_2 - n_1\cos\theta_1}{n_2\cos\theta_2 + n_1\cos\theta_1} \tag{5.2}$$

$$T_{//} = \frac{2(\varepsilon_{r1}\varepsilon_{r2}\mu_{r2}/\mu_{r1})k_{1z}}{\varepsilon_{r1}k_{2z} + \varepsilon_{r2}k_{1z}} = \frac{2n_2\cos\theta_1}{n_2\cos\theta_2 + n_1\cos\theta_1} \tag{5.3}$$

$$R_{\perp} = \frac{\mu_{r2}k_{1z} - \mu_{r1}k_{2z}}{\mu_{r2}k_{1z} + \mu_{r1}k_{2z}} = \frac{n_2\cos\theta_1 - n_1\cos\theta_2}{n_2\cos\theta_1 + n_1\cos\theta_2} \tag{5.4}$$

$$T_{\perp} = \frac{2\mu_{r2}k_{1z}}{\mu_{r2}k_{1z} + \mu_{r1}k_{2z}} = \frac{2n_2\cos\theta_1}{n_2\cos\theta_1 + n_1\cos\theta_2} \tag{5.5}$$

where n_i (i = 1, 2) is the intrinsic impedance of medium i (i = 1, 2)

The calculated transmission using 1D TMM and CST Microwave Studio are in good agreement (Fig. 5.13(b)). Therefore, it is also in agreement with the measurement.

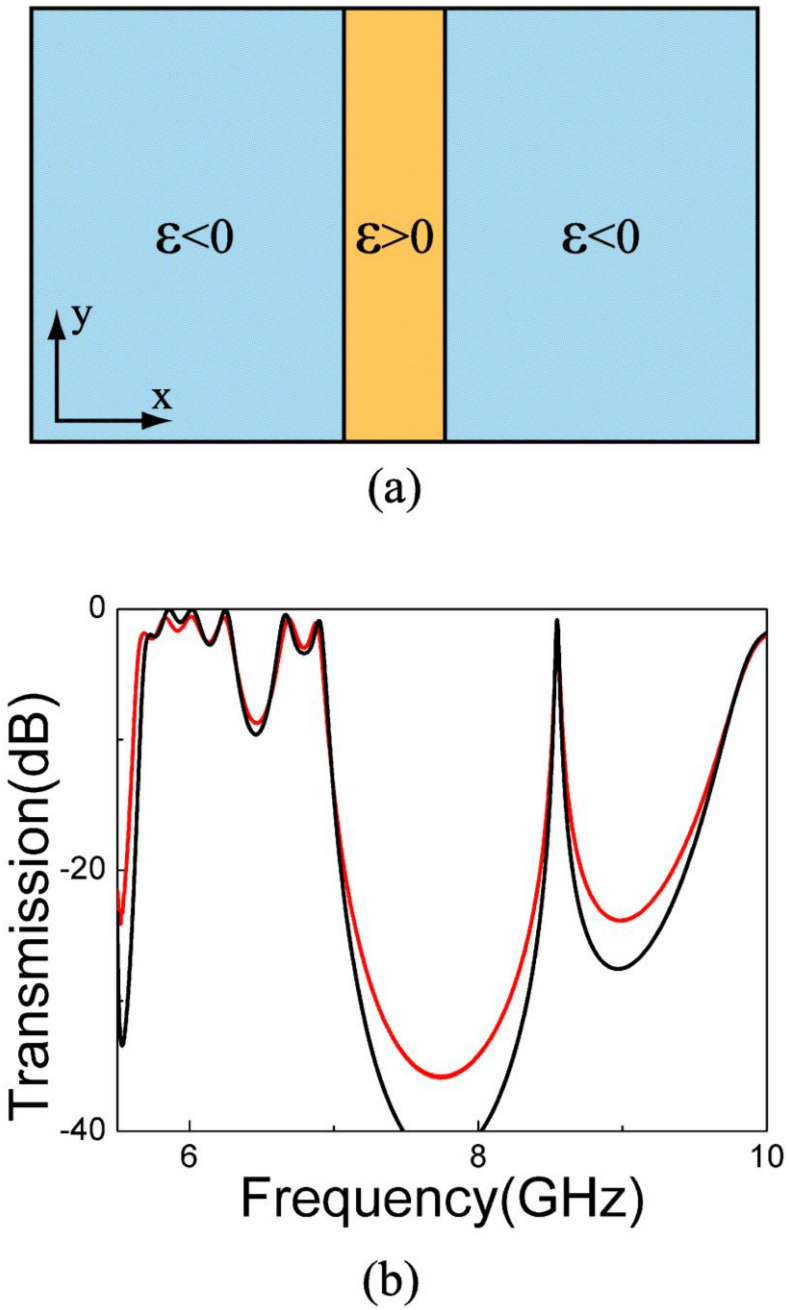

Figure 5.13: (a). The CMM based cavities can be treated as 1D FPRs with a subwavelength cavity region at the center. (b). The calculated transmission from the model of the CMM based cavity (D3) structure using the 1D transfer matrix method (black line) and CST Microwave Studio (red line) are in good agreement.

In order to demonstrate the validity of the FPR model we investigated the resonant condition at the cavity frequency for CMM based cavity structure. We considered each 4 layers CMM structure as the mirrors of the FPR with the reflection coefficient $re^{-i\phi}$, where ϕ is the reflection-phase factor in radians. In a FPR, the circulating field E_c can be written as a function of the incident field E_i as:

$$E_c = \frac{t}{1-r^2 e^{-2i(\beta L+\phi)}} E_i \tag{5.6}$$

where β is the propagation constant of cavity structure, L is the length of the cavity, and t is the transmission coefficient of the mirror. This equation is valid also for our model. In our model, the mirrors are 2 layer CMM structure and φ is the reflection-phase from this structure. The resonant condition is satisfied when

$$\phi_T = \beta L + \phi = m\pi \text{ (m=0, ±1, ±2…)} \tag{5.7}$$

where enhancement of the circulating fields results a high transmission at the resonant frequencies [95, 96]. For our model, this resonance condition can be viewed as cavity resonance, where a narrow transmission window within the band gap region is observed.

We calculated the reflection-phase (ϕ) for 4 layer CMM using CST MWS and total phase by adding the additional phase component from the cavity structure. The calculated total phase (ϕ_T) around the cavity resonance shows that the resonance condition is satisfied at the cavity mode frequency for a CMM based cavity structure, just like in FPRs (Fig. 5.14).

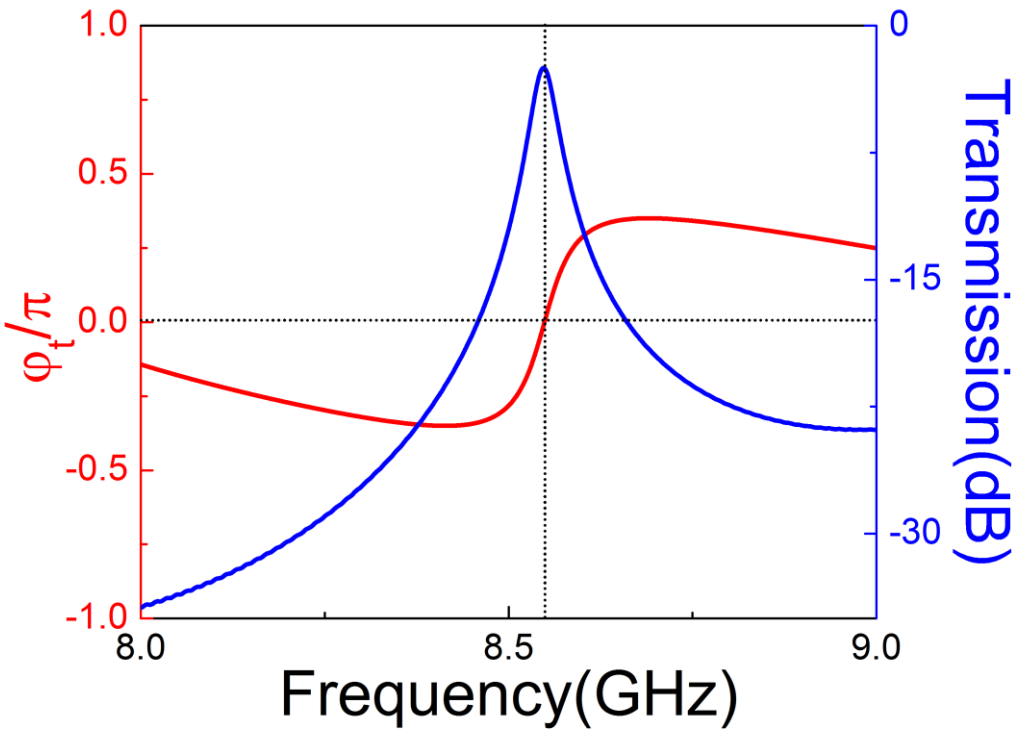

Figure 5.14: The calculated total phase (τ) around the cavity resonance shows that the resonance condition is satisfied at the resonance frequency for a CMM based cavity (D3) structure, just like in FPRs.

5.9. Metamaterial based coupled cavity systems

In this section, we investigate metamaterial based 2 and 3 cavity systems. We brought two cavities together with an intercavity distance of two metamaterial unit cells. The total two-cavity system contains two cavities and four metamaterial unit cells at each side of each cavity (2 cavities+10 metamaterial unit cells) in the propagation direction. For two coupled cavities, the transmission characteristics as a function of frequency are measured and calculated.

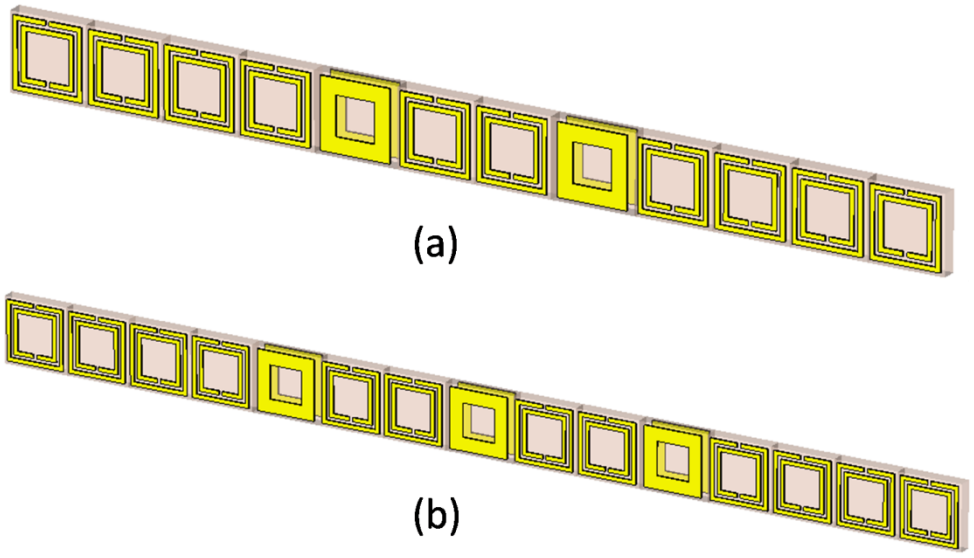

Figure 5.15: (a) The total two-cavity system contains two cavities and four metamaterial unit cells at each side of each cavity (b) the total three-cavity system contains three cavities and four metamaterial unit cells in each side of the each cavity.

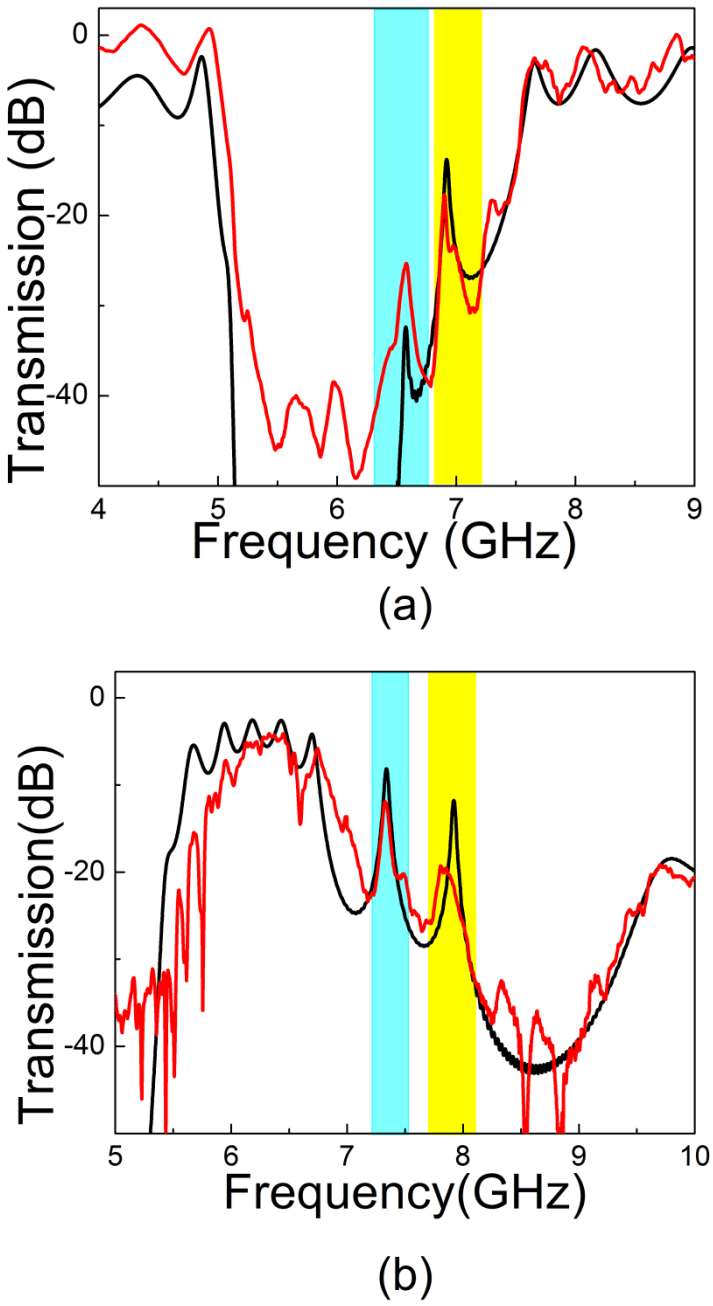

Figure 5.16: Measured (red curves) and calculated (black curves) transmission spectra for (a) SRR based (b) CMM based two-coupled-cavity. The measured values of resonance frequencies are ω_1=6.5 GHz and ω_2=6.9 GHz for the SRR based cavity structure and ω_1=7.3 GHz and ω_2=7.9 GHz for the CMM based cavity structure.

As shown in Fig. 5.16, we observed that the resonance modes are split into two distinct symmetric and antisymmetric modes that are similar to a PC cavity structure. In PC cavity structures, when two isolated cavities are brought together the localized photon modes should overlap. Due to this interaction, the doubly degenerate eigenmode splits into two distinct modes as: symmetric and antisymmetric [97]. These modes are reminiscent of the bonding and antibonding states in solid state physics. For example, in the diatomic molecules, the interaction between the two atoms produces a splitting of the degenerate atomic levels into bonding and antibonding orbitals [98]. The measured values of resonance frequencies are ω_1=6.5 GHz and ω_2=6.9 GHz for the SRR based cavity structure and ω_1=7.3 GHz and ω_2=7.9 GHz for the CMM based cavity structure.

When we brought three cavities together with an intercavity distance of two metamaterial unit cells, the single cavity mode Ω splits into three different eigenmodes. In this case, the total three-cavity system contains three cavities and four metamaterial unit cells in each side of the each cavity (3 cavities+12 metamaterial unit cells) in the propagation direction. The corresponding transmission spectra of the system were measured and calculated. As shown in Fig. 5.17, there is a good agreement between the measured and calculated transmission characteristics of the three coupled cavities. The resonance frequencies were Γ_1=6.4 GHz, Γ_2 =6.7 GHz, and Γ_3=7.0 GHz for the SRR based cavity structure and Γ_1=7.2 GHz, Γ_2=7.6 GHz, and Γ_3=8 GHz for the CMM based cavity structure.

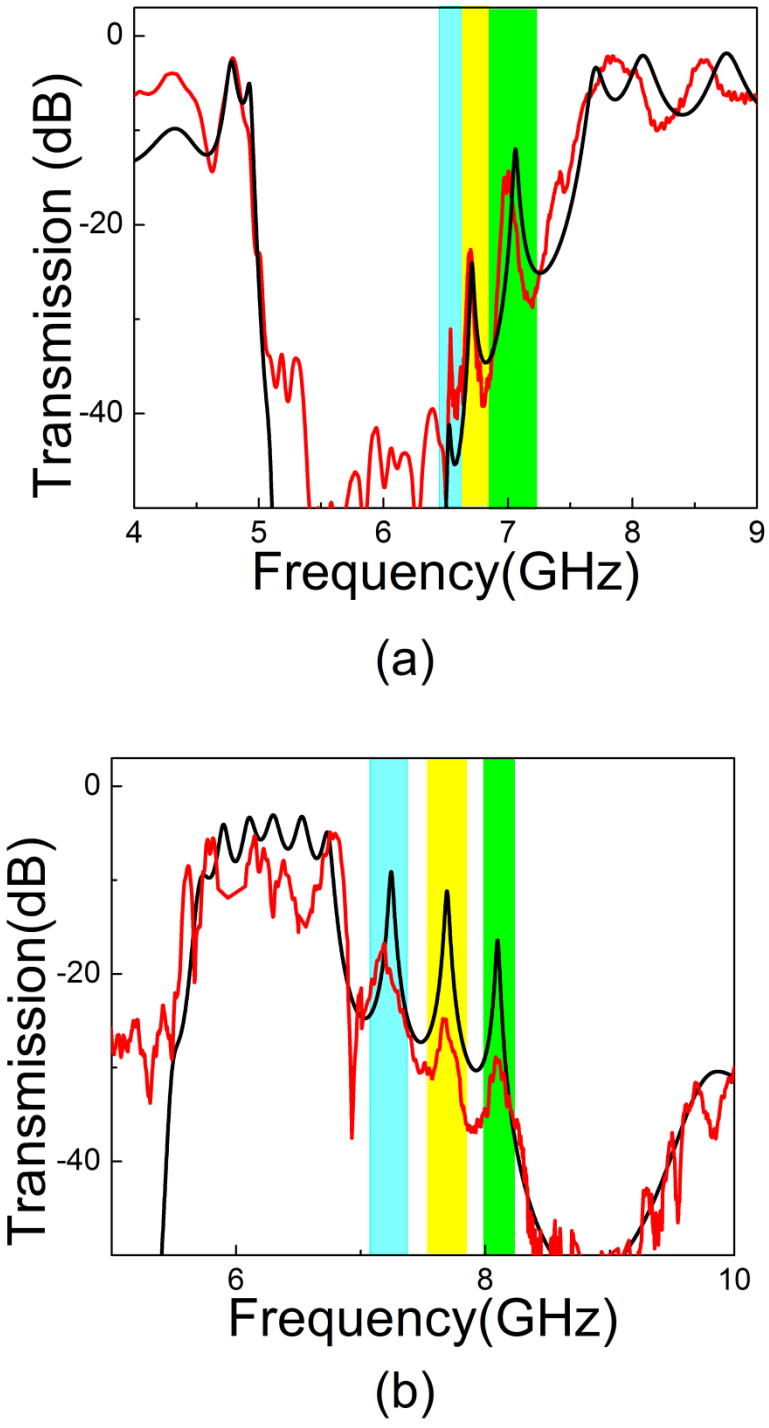

Figure 5.17: Measured (red curves) and calculated(black curves) transmission spectra for (a) SRR based (b) CMM based three-coupled-cavity.

The classical wave analog of the tight-binding (TB) picture [99] has successfully been applied to photonic structures [100]. By using the direct implications of the TB picture, a novel propagation mechanism for photons along the localized coupled cavity modes in PCs was proposed [101] and demonstrated [102]. In these structures, photons can hop from one tightly confined mode to the neighboring one due to the weak interaction between them. The same approach can be applied to metamaterial based coupled cavities. Using the TB picture, it is possible to obtain eigenvalues and eigenvectors corresponding to two coupled cavity structures [102, 103]. Hence, the dispersion relation and group velocity can be obtained, keeping only the nearest-neighbor coupling terms as:

$$\omega(k) = \Omega[1 + \kappa \cos(k\Lambda)] \tag{5.8}$$

$$v_g(k) = \nabla_{\mathrm{k}}\omega_{\mathrm{k}} = -\kappa\Lambda\Omega \sin(\mathrm{k}\Lambda) \tag{5.9}$$

Here, κ is a TB parameter that can be obtained from the splitting of the eigenmodes of two coupled cavities, in which Ω is the frequency mode of the single cavity and Λ is the distance between the two cavity structures (intercavity distance).

The calculated TB parameter is κ=-0.07 for CMM based coupled cavities. We can obtain the dispersion relation of the coupled cavity structures by using these TB parameters and Λ= 9.9 mm (4 metamaterial unit cells). Figure 5.18(a) shows the calculated dispersion relation ω(k). We also plotted the normalized group velocity corresponding to the coupled cavity structure. As shown in Fig. 5.18(b), the group velocity has a maximum value of nearly one-hundredth the speed of light in vacuum, at the coupled-cavity band center, and vanishes at the band edges.

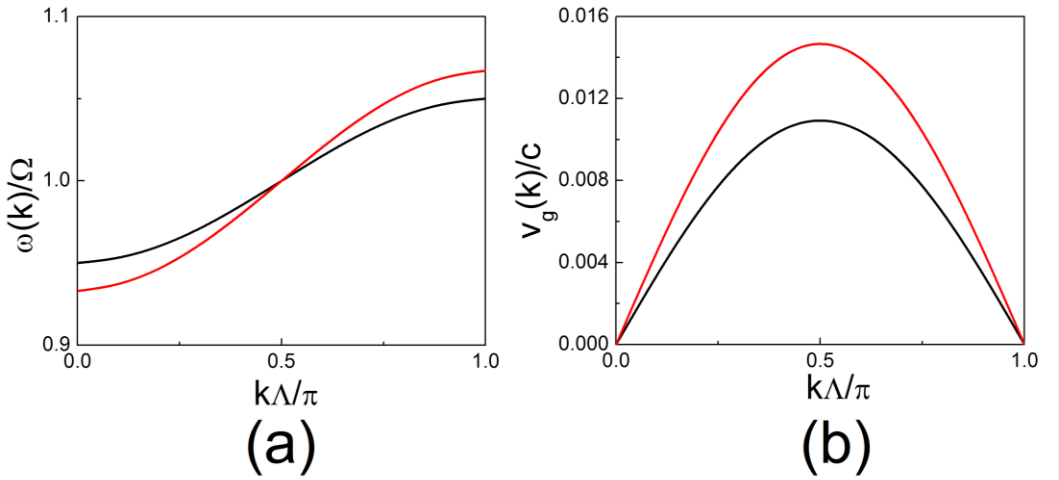

Figure 5.18: (a) The calculated dispersion relation of the coupled cavity structures is shown (black curves stand for the SRR based cavity and the red curves stand for the CMM cavity structure.) (b) The group velocity is two orders of magnitude smaller than the speed of light at the band center and vanishes at the band edges.

The proposed cavity structures can be extended to optical frequencies and can be used in several applications such as nonlinear optics and high density data storage.

Chapter 6

Ultrafast and sensitive bioassay

6.1. Introduction

Artificially constructed materials may exhibit different physical characteristics that are not attainable by ordinary materials. One of the most common elements of metamaterials, which was introduced by Pendry *et al.* in 1999, is the split ring SRR [104]. In recent years SRRs have received a growing amount of interest since such structures may lead to negative values of permeability. Later experimental and theoretical studies have shown that SRR media, when combined properly with thin wire media, may exhibit left-handed properties [105-107]. An SRR structure consists of concentric rings separated by a gap. Magnetic resonance is induced by the splits at the rings and by the gap between the inner and outer rings [104]. The resonance frequency of the SRR depends on its geometrical parameters [108, 109]. Since SRR structures are quite undiscovered and are the essential components of left-handed metamaterials, a considerable amount of effort has been made in order to understand the underlying physics of SRRs [109-112]. SRR structures are mainly used to increase antenna performance for obtaining properties such as an electrically small antenna size [113-116] and high directivity [117, 118].

In this chapter, we investigate the use of SRRs for bioassay (biological assay) applications. We report the results of a new bioassay technique that

significantly improves the total assay time and the lower detection limit of colorimetric Enzyme-Linked Immunosorbent Assay (ELISA). The new bioassay technique is based on 1) the focusing of microwaves by SRR structures to a small volume micro-cuvette for uniform heating, 2) the creation of a thermal gradient between the assay medium and the silver nanoparticles for rapid completion of the bioassay steps.

6.2. Limitations of Bioassays

Bioassays are typically conducted to measure the effects of a substance on a living organism. Bioassays are widely used for the detection and determination of a wide variety of proteins, peptides, and small molecules. Currently, the two major limitations encountered in the bioassays are: rapidity of the bioassay and detection sensitivity. Rapidity of the bioassays is controlled by the chemical kinetics involved during the binding of proteins. The rapid detection of target biomolecules, becomes an important issue in the event of an outbreak of an infectious disease or a biological terror attack that has an immediate impact on human health. Sensitivity of the bioassays is affected by the quantum yield of fluorophores and the optical limitations of the detection system.

It was previously shown that the rapidity and sensitivity of fluorescence-based bioassays can be improved by the combined use of low-power microwave heating and plasmon-resonant particles (PSPs, e.g., silver nanoparticles) [119, 120]. The improvement in the sensitivity of the bioassays is due the close-range interactions of fluorescent species with PSPs, where an increase in fluorescence signatures and a decrease in lifetimes of fluorophores are observed [121]. The rapidity was improved by low-power microwave heating of the bioassay components, where a thermal gradient between the assay medium and PSPs result in the completion of biorecognition events in less than 1 minute [119]. Despite the usefulness of low-power microwave heating with PSPs for the construction of rapid bioassays, the issue of control over the uniform heating of small volume

samples (≤ 10 μl) remains unresolved. One has to employ additional materials on the bioassay platform to remove the excess microwave energy, which leads to an increase in the duration of microwave heating and in some cases evaporation of the small volume samples. In this regard, one can alleviate these issues using focused microwaves.

Focusing of microwaves to a specific region of interest, especially for small volume samples, can be accomplished by the use of metal-based mini-antennas with dimensions smaller than the wavelength of incident EM energy [122]. The mini-antennas focus the incident electric field to sharp edges of the mini-antennas, where up to a ~40,000-fold enhancement of the electric field is predicted [122]. Subsequently, the temperature of any solvent placed near the edges of the mini-antennas can be increased in a controlled manner. It was shown that one can extract biological materials from Anthrax spores by breaking down the walls of the spores by focused microwaves using aluminum mini-antennas fashioned into a "bow-tie" structure [123]. Despite their potential, these mini-antennas were never employed in bioassays. In this chapter, we report an ultrafast bioassay preparation method that overcomes the above-mentioned limitations using a combination of low power microwave heating and SRR structures.

6.3. Construction and characterization of SRR structures

The SRR structures are deposited on a FR4 substrate (2x2 cm^2) with a copper layer of thickness 30 μm deposited on the board. FR4 (National Electrical Manufacturers Association designation for circuit boards) is made from woven fiberglass with epoxy resin binder. The geometrical parameters of the SRR are d = 3 mm, t = 0.9 mm and w = 9.4 mm as shown in Fig. 6.1(a). The circuit board has a thickness 2.4 mm and dielectric constant of ε = 3.85. A single micro-cuvette with 10 μl volume capacity is drilled in the split of the SRR. Fig. 6.1(b) shows the real-color photograph of a typical SRR structure.

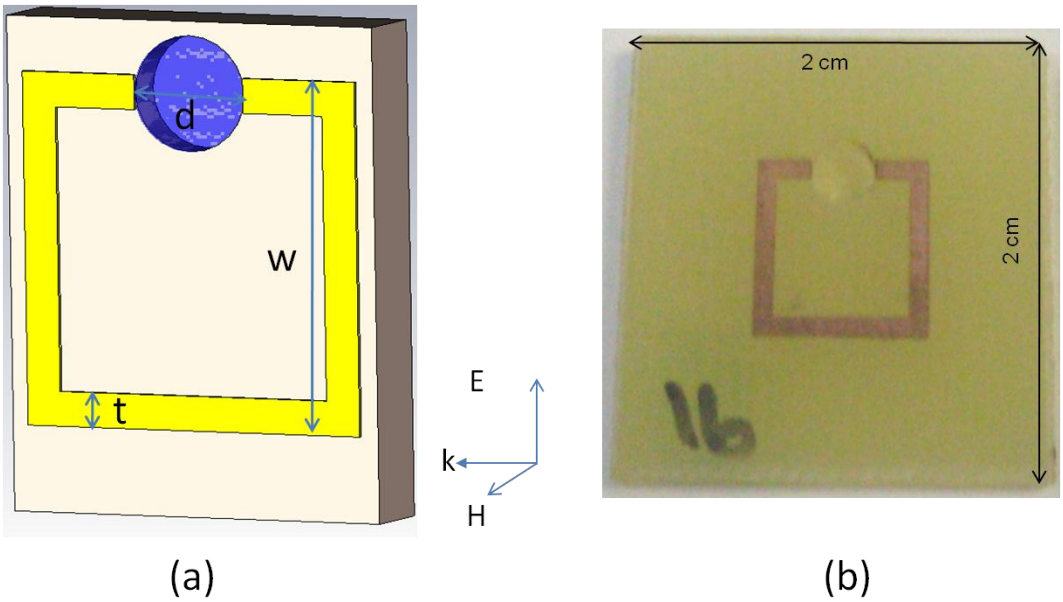

Figure 6.1: (a) Schematic depiction of copper SRR structures printed on a circuit board. The dimensions of the SRR structures are d = 3 mm, t = 0.9 mm and w = 9.4 mm. A single micro-cuvette (depth = 1 mm) is drilled in the split of the SRR and has a 10 µl volume capacity. (b) Real-color photographs of SRR structures.

Numerical simulations of the transmission spectrum of SRR structures were carried out to validate the use of SRR structures at 2.45 GHz. Simulations are carried out using a commercially available fullwave solver, CST Microwave Studio® (Computer Simulation Technology AG), which employs finite integration method [105]. In the simulation setup, the structure is subjected to an incident plane wave. Open boundary conditions are employed along the propagation direction (the incident field propagates along the x-direction, with E and H along the y- and z-direction, respectively). The transmission amplitudes are obtained by using the fields at a distant point from the structures.

Transmission spectrum of the constructed SRR structures was also experimentally measured. Two monopole antennas are used to transmit and detect the EM waves through the single SRR according to the previously published

procedure [124]. In this regard, first, the transmission spectrum in free space (i.e. without the SRR) was measured using monopole antennas and a HP-8510 C network analyzer. This spectrum was used to calibrate the network analyzer. The transmission spectrum of the SRR structures was measured by maintaining the distance between the transmitter and receiver monopole antennas. The length of the monopole antennas are $\lambda/2$, arranged to work at the frequency range covering the ω_m of the SRR structures.

6.4. Deposition of Silver Island Films inside the micro-cuvette of SRR structures

The micro-cuvettes were incubated with hydrogen peroxide for 5 min to oxidize the surface. Then, the surfaces were functionalized with amine groups by incubating a 10 μl aqueous solution of poly-lysine (5% w/v) inside the micro-cuvettes for 2 hours. Unbound material was washed with deionized water. Silver Island Films (SIFs) were deposited inside the micro-cuvette (bottom and the walls) using a modified version of the Tollen's reaction scheme. In this regard, first a solution of silver nitrate (0.5 g in 60 ml of deionized water) was placed in a clean 100-ml glass beaker. While stirring at the quickest speed, 200 μL of freshly prepared 5% (w/v) sodium hydroxide solution is added, which results in the formation of dark brown precipitates of silver particles. The precipitates were re-dissolved by ammonium hydroxide (2 ml). The resultant clear solution is cooled down to 5°C by placing the beaker in an ice bath. After 2 minutes, a fresh solution of D-glucose (0.72 g in 15 ml of water) is added. Subsequently, a 10 μl portion of this mixture was transferred to the micro-cuvettes and the temperature of the mixture is then warmed to 40°C by placing the SRR structures into pre-warmed laboratory oven (ThermoFisher, Model 280A). As the color of the mixture turns from yellow to green to green-brown (in 20 minutes), the mixture is removed from the micro-cuvettes. Subsequently, SIFs-deposited SRR structures were rinsed with deionized water several times and kept in air-tight dry containers until further use.

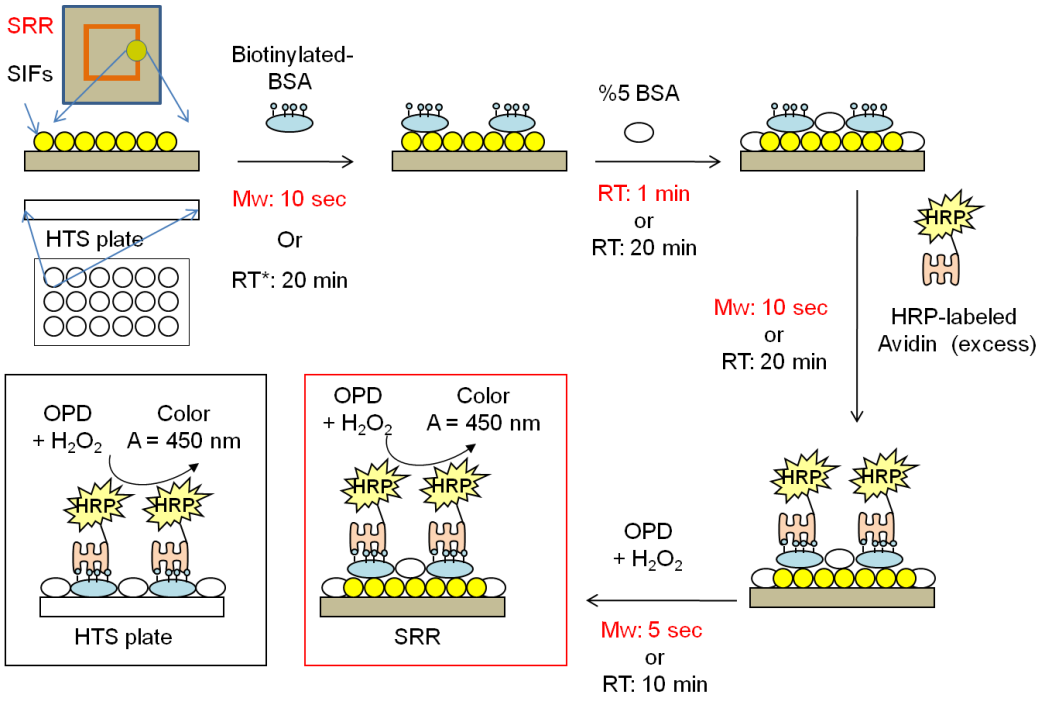

Figure 6.2: Schematic depiction of the ELISA for the detection of the model protein (biotinylated-BSA) used in this study. Control experiments were carried out in a commercially available 96-well high throughput screening (HTS) plates without SIFs. SRR: Split ring resonator structures; SIFs: Silver island films; BSA: Bovine serum albumin; HRP: horse radish peroxidase; OPD: o-Phenylenediamine; RT: Room temperature; Mw: Low-power microwave heating; A: Absorbance.

6.5. Construction of colorimetric ELISA on SRR structures and HTS plates

In order to compare the efficiency (in terms of assay time and sensitivity) of SRR structures with the commercially available HTS plates, identical ELISA test for a model protein (b-BSA) was carried out on both the SRR structures using microwaves and on HTS plates at room temperature. Figure 6.2 shows the schematic depiction of the ELISA test used for b-BSA. In the first step, a solution

of b-BSA with a range of bulk concentrations (1 μM to 1 pM) was incubated on SRR structures (10 μl) and HTS plates (100 μl) using low power microwave heating (Emerson Model no: MW8784SB, power input 1050W at 2.45 GHz, duty cycle:3) for 10 seconds or at room temperature for 20 minutes, respectively. Unbound material was removed by rinsing with deionized water several times. The surfaces were then treated with 5% (w/v) BSA to reduce the non-specific binding of avidin. In the next step, a 1 mg/ml solution of HRP-labeled avidin was incubated on SRR structures (10 seconds, microwave heating, duty cycle: 3) and HTS plates (20 minutes, room temperature). After washing off the unbound material by rinsing the surface with deionized water several times, a mixture of OPD and hydrogen peroxide was incubated on SRR structures (10 seconds, microwave heating, duty cycle: 3) and HTS plates (10 minutes, room temperature). The enzymatic reaction was stopped by the addition of 0.1 M sulfuric acid at the end of the indicated reaction times. Due to the intense color of the mixture on SRR structures and to measure the absorbance spectrum, this mixture was diluted and transferred to the HTS plates. The dilution of the mixture was done to ensure that the absorbance reading of all samples was less than 1. All experiments were repeated at least three times.

6.6. Ultrafast and sensitive Bioassay

In order to employ SRR structures in biosensing applications using microwave heating, these structures have to be designed to function at the desired microwave frequency. Since most biosensing applications are based on water and water can be efficiently heated at 2.45 GHz using a conventional microwave oven, a SRR structure was designed that functions at 2.45 GHz. In this regard, first the SRR structures were characterized based on their transmission properties. It is well known that SRR structures have a strong response to EM wave due to magnetic resonance, which can be observed as a “dip” in the transmission spectrum of the SRR structure [125, 126]. This can be attributed to the resonant nature of the SRR

structures. Figure 6.3(a) shows the simulated and the experimental transmission spectrum for the SRR structures. Numerical simulations predict a dip in the transmission spectrum at 2.45 GHz, which is also experimentally observed, proving that the designed SRR structures function at 2.45 GHz. As seen in Fig. 6. 3(a)values >0 dB were obtained from measurements. This is essentially related to two effects. One is related to the presence of dielectric board which, due to higher index of refraction, causes local confinement of the emitted signal by refraction through the board, and by the diffraction at the edges of the board. The other reason is that the presence of resonant structure (namely SRR) enhances the field locally compared to free space propagation In addition, numerical calculations predict that the exposure of the SRR structures to an external magnetic field induces solenoidal current along the split ring (Fig. 6.3(b)). That is, the SRR structure can be considered as a resonant magnetic dipole. The associated magnetic-field pattern from the SRR was previously shown to be dipolar [127].

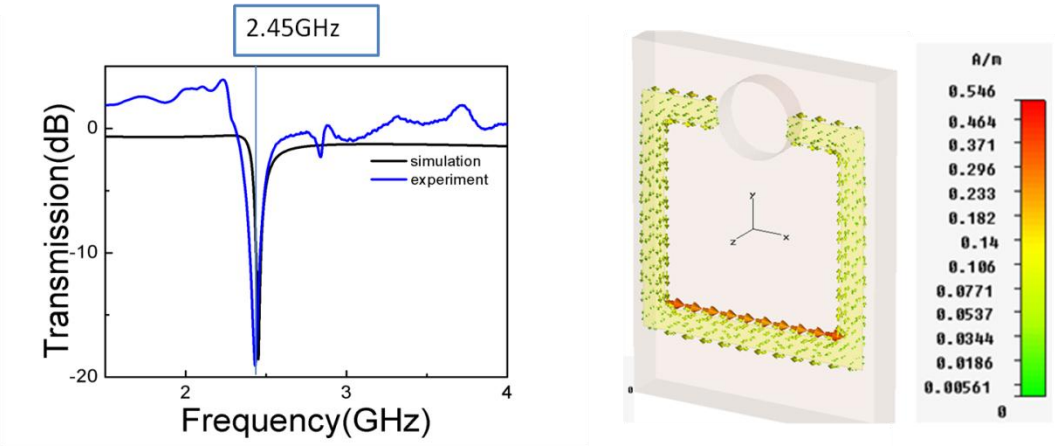

Figure 6.3: (a) Simulated and experimental transmission spectrum for SRR structures. (b) Calculated surface current distribution along the SRR structures.

In addition, the SRR structures are predicted to concentrate the incident electric field within the split in the ring. Figure 4 shows the simulated electric-field (total field) distribution along X-Y (Figure 6.4(a)) and Z-planes (Fig. 6.4(b)) of the SRR structures. Figure 6.4(a) shows that electric fields are focused around the tips of the split in the ring, which was also shown for other metal-based mini-antennas [123]. This prediction can be explained in terms of short-circuiting the propagation of the incident electric field across the metal surface, such that charge builds up in the split of the ring, effectively localizing the microwaves to the micro-cuvette. In addition, the enhancement of incident electric field along the ring is also predicted, which is due to the excess charge buildup in the ring. One can manipulate the charge buildup by varying the magnitude and duration of the incident field. It is important to note that the micro-cuvette has a depth of 1mm, and the enhanced incident electric field on the X-Y plane crosses the top of micro-cuvette. That is, the incident electric field (in the X-Y plane) will be localized to the top of the micro-cuvette but not throughout the micro-cuvette. Subsequently, water placed in the micro-cuvette will not be effectively heated by the localized electric fields in the X-Y plane. Since the bioassays will be carried out only in the micro-cuvette, which has a volume of 10 μl, the electric field enhancement in the Z-plane is more relevant to the rapid heating of the solution placed in the micro-cuvette. As shown in Fig. 6.4(b), the electric field enhancement in the Z-plane is predicted to occur uniformly throughout the micro-cuvette extending into the entire micro-cuvette. Subsequently, the rapid and uniform heating of the solution placed in the micro-cuvette can be realized.

It is important to further comment on the nature of the micro-cuvette. The SRR structures were designed for bioassays that are required to process small volume samples. In this regard, two parameters were considered during the design of the SRR structures: 1) a micro-cuvette with a small-volume capacity that will reduce the assay time to a few seconds while yielding measurable absorption signal after the completion of the bioassays and 2) no loss of samples will occur due to low power microwave heating. It is also important to note that the walls and

the bottom of the micro-cuvettes are modified with silver nanoparticles to create a thermal gradient between the solution and the surface of the silver nanoparticles where the bioassays are constructed. It was previously shown that the metal nanoparticles do not interact with the incident electric field due to their relatively small size (~80 nm) as compared to the wavelength of the microwaves (12.2 cm at 2.45 GHz) [119, 128]. Subsequently, it is expected that the inclusion of non-continuous silver nanoparticles inside the micro-cuvettes will not affect the electric field distribution, but play an important role in the creation of the thermal gradient.

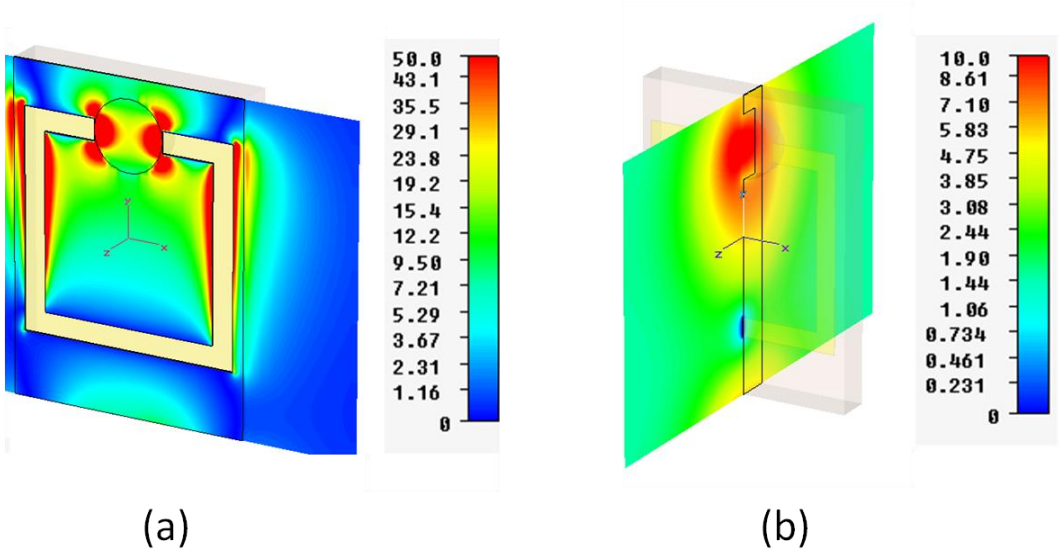

Figure 6.4: Simulated electric field enhancements for SRR structures (a) X-Y plane and (b) Z-plane. The scales displayed to the right of the figures represent the magnitude of the electric field intensity distribution in the respective dimensions.

Figure 6.5 shows the real-color photographs of the SRR structures with and without silver nanoparticles present in the micro-cuvettes. SRR structures with mechanically drilled micro-cuvettes before the deposition of silver nanoparticles have the same color of the FR4 substrate, which is composed of fiber glass and epoxy resin. After the deposition of silver nanoparticles, the color of the surface of micro-cuvette was changed to the color of silver nanoparticles (green-brown). The color of silver nanoparticles deposited onto surfaces depends on the loading and the size of the nanoparticles themselves. As shown in Fig. 6.5, the color of the

silver nanoparticles in 5 different SRR structures look nearly identical, proving the reproducibility of the process of deposition of silver nanoparticles. According to our procedure silver nanoparticles are allowed to grow for 20 minutes at 40°C, which resulted in higher loading density of silver nanoparticles as compared to a typical SIFs surface used for other applications [119]. It is important to note that the detection signal in the present study is absorbance based and subsequently, the effect of silver nanoparticles on the signal is not sought as one would do in metal-enhanced fluorescence based biosensing scheme [119]. The criteria for the extent of loading of silver nanoparticles in the present study are 1) retaining the split in the ring (so that the circuit of the ring is not completed) and 2) providing the largest amount of surface area (of silver nanoparticles) for the construction of the bioassays. In this regard, the deposition of thin metal films inside the micro-cuvette would complete the circuit and the SRR structures would be unusable for biosensing applications.

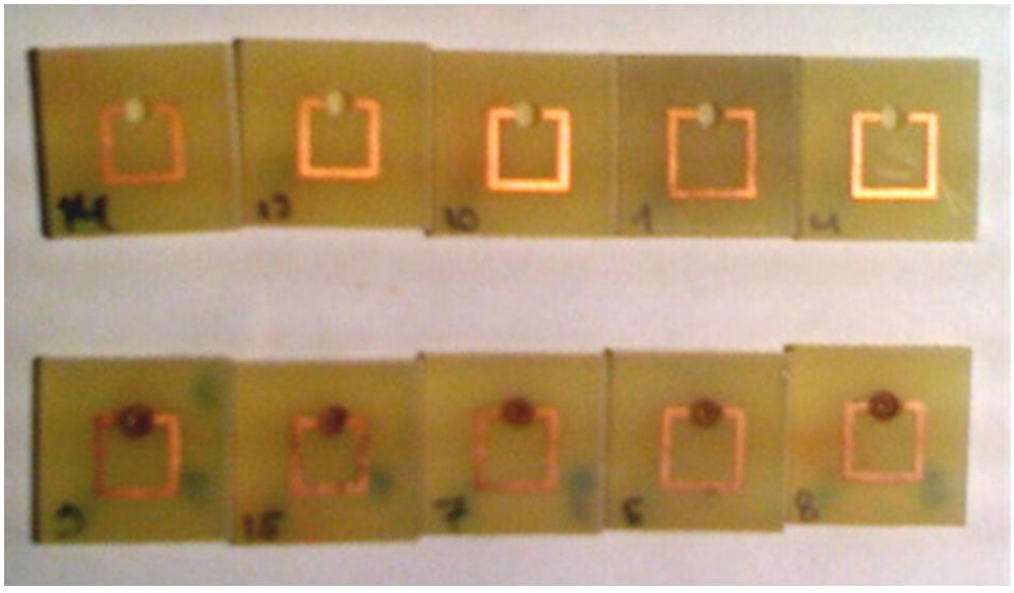

Figure 6.5: Reproducibility studies for the deposition of SIFs inside the micro-cuvettes of the SRR structures. SIFs were deposited at the same time using Tollen's reaction scheme. SIFs were covalently linked to poly-lysine groups inside the micro-cuvettes and did not detach from the surface after the completion of the bioassays.

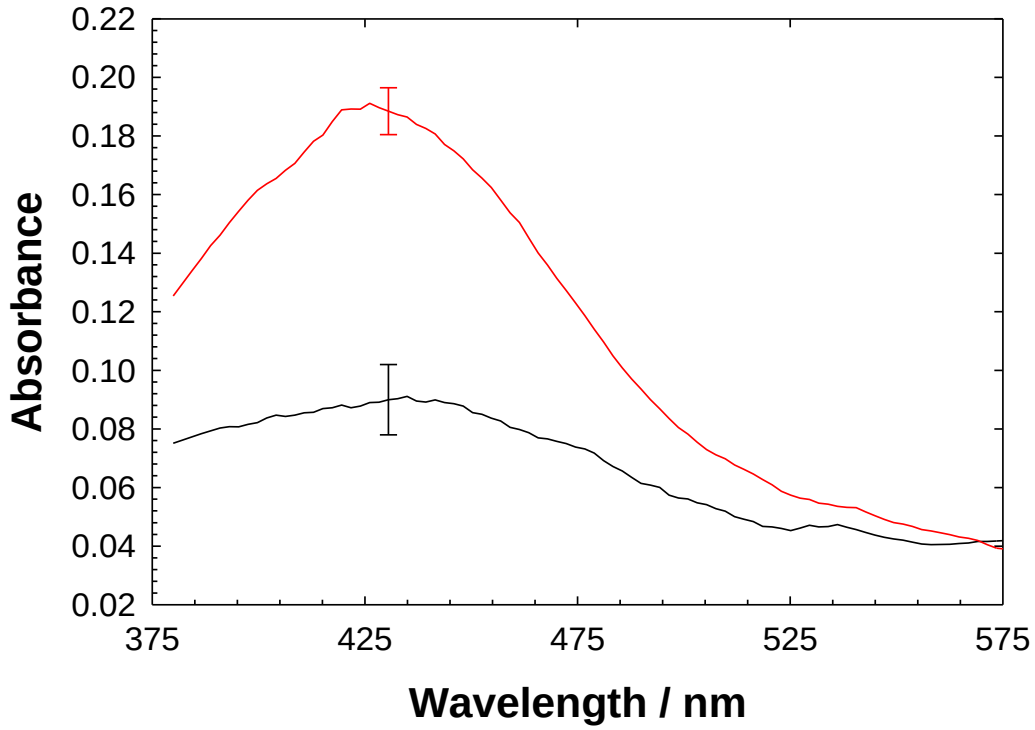

Figure 6.6: Typical absorbance spectrum for OPD after the completion of ELISA for 10^{-9} M b-BSA using SRR structures (Mw assay) and HTS wells (RT assay). The average spectrum for 3 different runs is shown. The enzymatic reaction was stopped using 0.1 M sulfuric acid, which is also used to dilute the solution to keep the absorbance value < 1.

The proof-of-principle demonstration of the ultrafast bioassays was accomplished by using a model biotin-avidin bioassay. Figure 6.6 shows a typical absorption spectrum for OPD (organic substrate for HRP enzyme) after the completion of ELISA for a model protein (b-BSA) using SRR structures (Mw assay) and HTS wells (RT assay). It is important to remind that the control experiments at room temperature was carried out using commercially available 96-well HTS plates to directly compare the efficiency of new SRR structures in terms of total assay time and sensitivity with the "gold standard" for ELISA tests, which are HTS plates. A typical ELISA test for b-BSA using HTS plates at room

temperature took 70 minutes to complete. The identical ELISA took less than 2 minutes to complete using the new SRR structures, low-power microwave heating and silver nanoparticles. As shown in Fig. 6.6, the absorption value for 10 nM b-BSA sample was significantly larger for ELISA on SRR structures than the identical assay on HTS wells. This is thought to occur due to the increased efficiency of enzymatic reaction by microwave heating. It was previously shown that when exposed to microwaves the conversion of the non-luminescent organic substrates to luminescent products by HRP is significantly increased [122, 129]. In this regard, the use of low power microwaves increases the sensitivity of ELISA, where larger absorbance (or chemiluminescence) signals are obtained using microwave heating for the enzymatic conversion of the organic substrates, as compared to room temperature incubation.

Figure 6.7 shows the comparison of the normalized absorbance at 450 nm for OPD after the completion of ELISA for the detection of b-BSA using SRR structures (Mw assay) and HTS wells (RT assay). In control experiments, where b-BSA is omitted from the surface, the background signal (horizontal lines in Fig. 6.7) is measured to determine the lower detection limit for ELISA using both the SRR structures and HTS wells. In room temperature ELISA carried out on HTS wells, which took 70 minutes to complete, the detectable concentration range for b-BSA was ~1 nM – 1 μM. Using SRR structures, low-power microwaves heating and silver nanoparticles the identical ELISA was completed within 2 minutes and the lower detection limit for b-BSA is improved by 100-fold (0.01nM). That is, the lower detection limit for the absorbance-based ELISA is now approaching the sensitivity of ELISA based on chemiluminescence detection scheme, which is a significant improvement of the current absorbance-based bioassays. The detectable concentration range for b-BSA using SRR structures was ~0.01 nM – 1 μM. It is also important to note that silver nanoparticles did not detach from the surface after the completion of the bioassays.

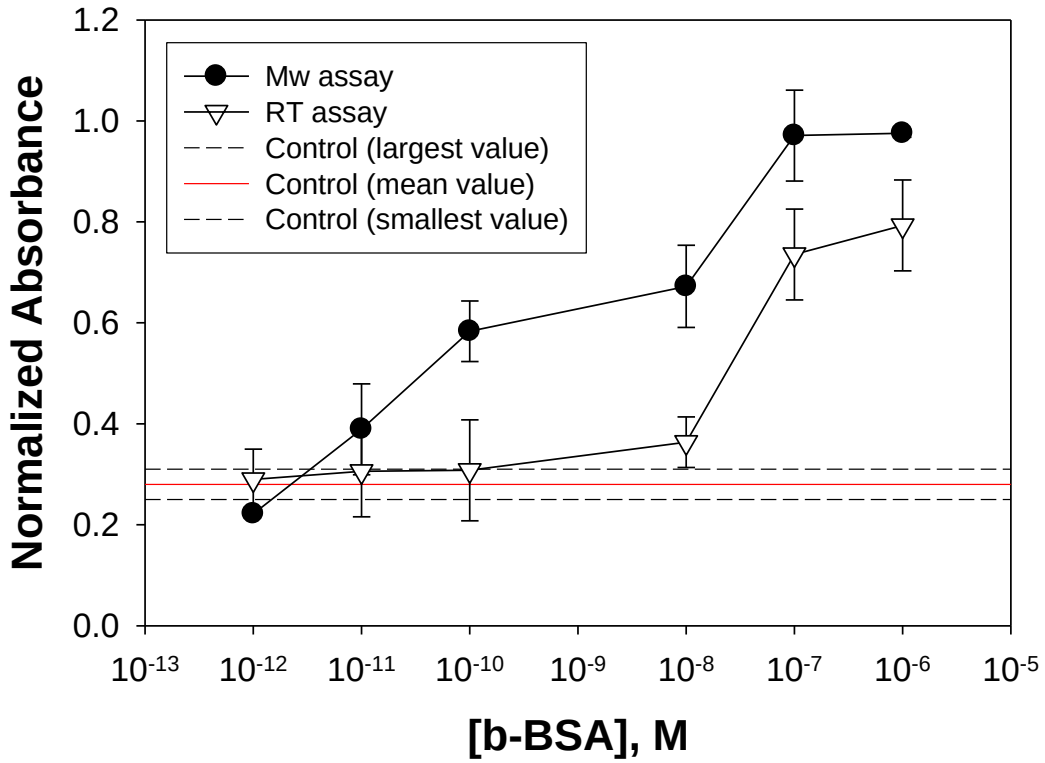

Figure 6.7: Normalized absorbance at 450 nm for OPD after the completion of ELISA for the detection of b-BSA using SRR structures (Mw assay) and HTS wells (RT assay). The absorbance values were normalized to the largest value observed: 10^{-6} M for Mw assay. The average absorbance for 3 different runs is shown. In the control experiment, b-BSA was omitted from the surface. The mean (red solid line), largest (dashed black line) and smallest (dashed black line) absorbance values for control experiments are shown to determine the detectable concentration range using both methods.

While the bioassay for the detection of b-BSA took 70 minutes to complete on HTS wells at room temperature, the identical bioassay was completed within 2 minutes using low-power microwave heating and the silver nanoparticle-modified SRR structures. The detectable concentration range for b-BSA was ~1 nM – 1 μM and ~0.01 nM – 1 μM for ELISA run at room temperature (HTS plates) and with microwave heating (SRR structures), respectively. A 100-fold improvement of the lower detection limit for b-BSA using SRR structures over HTS plates is observed.

Chapter 7

Conclusion

The aim of this thesis was to investigate beaming and localization of EM waves in periodic structures at microwave frequencies. We characterized periodic structures: subwavelength metallic gratings, PCs and metamaterials by using experimental and numerical techniques.

In chapter 2, we studied off-axis directional beaming from subwavelength aperture with metallic gratings. We obtained directional beaming from metallic aperture with symmetric gratings at SP resonance frequency. In order to change the beaming angle or, in other words, to steer the beam, we redesigned the output surface grooves. We changed the periods of the grooves on different sides of the aperture. One of the sides has a smaller period while the other side has a longer period than the input side. We verified the off-axis directional beaming with an FWHM of 10° by measuring and simulating transmission. We further showed that the beaming angle is 15°. Moreover we investigated the origin of the off-axis beaming by simulating 3 different cases with different output grating periods. The possibility to have steered beaming is a combinatory result of the generalized form for the conservation of the parallel component of the wave vector at the interface of a periodic medium, and the finite angle span of the source.

It is possible to excite surface waves by adding a periodic surface defect layer may be placed at the exit of a PC waveguide. These waves are analogous to SPs that are generated on the surface of corrugated metal gratings. Based on this

idea, in chapter 3, we investigated theoretically and experimentally the possibility of off-axis beaming from PC waveguide using asymmetric periodic surface layer. First of all, we theoretically showed that PC surface can support surface propagating EM waves in the presence of a periodic corrugation. We experimentally demonstrated that when a periodic corrugation is added to the output surface of the PC, the power emitted through the PC waveguide is confined to a narrow angular region. We observed a beaming angle of 15° with a FWHM of 10°. The momentum of the periodic corrugation surface waves and the angle span of the finite source define the beaming angle. Our results show that it is possible to steer the beam by the appropriate modification of the output surface.

In chapter 4, we studied frequency dependent beam steering with a PC with a surface defect layer made of dimmers. The dispersion diagram was obtained with the Plane Wave Expansion Method. The dispersion diagram reveals that the dimer-layer supports a surface mode with negative slope. Two facts are noted: First, a guided (bounded) wave was present, propagating along the surface of the dimer-layer. Second, above the light line, the fast traveling mode couple to the propagating spectra and as a result a directive (narrow beam) radiation with backward characteristics was observed and measured. In this leaky mode regime, symmetrical radiation patterns with respect to the normal to the PC surface were attained. We observed and measured beam steering in a 70° angular range when frequency ranges in the 11.88-13.69GHz interval. Thus, a PC based surface wave structure that acts as a frequency dependent leaky wave antenna was presented. Angular radiation pattern measurements are in agreement with those obtained via numerical simulations that employ the FDTD. Finally, the backward radiation characteristics that in turn suggest the existence of a backward leaky mode in the dimer-layer are experimentally was verified.

In chapter 5, we successfully demonstrated subwavelength localization with a metamaterial based cavity structure. Cavity resonances are observed in the transmission spectrum of a SRR and CMM based cavity structures. These cavity resonances are shown to exhibit high-quality factors. Since the unit cells of

metamaterials are much smaller than the operation wavelength, subwavelength localization is possible within these metamaterial cavity structures. We showed that the EM field is localized into a region of $\lambda/8$, where λ is the cavity resonance wavelength.

Subsequently, in taking full advantage of the effective medium theory, we modeled CMM based cavities as 1D FPRs with a subwavelength cavity at the center. We calculated the transmission from the FPR model using the 1D TMM, which is in good agreement with the measured result. We investigated the FPR phase condition for a CMM based cavity, in which the condition was satisfied at the cavity frequency. Therefore, our results show that it is possible to treat metamaterial based cavities as one-dimensional FPRs with a subwavelength cavity.

Moreover, we introduced coupled-cavity structures and presented the transmission spectrum of SRR and CMM based coupled-cavity structures. The splitting of eigenmodes was observed due to the interaction between the localized EM cavity modes. The dispersion relation and normalized group velocity of the coupled-cavity structures were calculated. The maximum group velocity was found to be 100 times smaller than the speed of light in vacuum.

Finally in chapter 6, we have reported a new approach to commercially available colorimetric ELISA demonstrating that the total assay time and lower detection limit of ELISA can be significantly improved. The new approach included the design and use of electrically small SRR structures to focus low-power microwaves to a small volume micro-cuvette containing silver nanoparticles, where the bioassay was constructed. The design of the SRR structures was carried out by numerical simulations to show these structures can function at the frequency of a common microwave oven (2.45 GHz), which were also confirmed by experimental transmission studies. Silver nanoparticles were covalently attached to the bottom and the walls of the micro-cuvette in a way that the presence of silver nanoparticles did not result in completion of the circuit in the SRR structures. Silver nanoparticles were used to create a thermal gradient

between the water and their surfaces, effectively driving the HRP-labeled avidin in the relatively warmer water to the surface of silver nanoparticles containing b-BSA. While the bioassay for the detection of b-BSA took 70 minutes to complete on HTS wells at room temperature, the identical bioassay was completed within 2 minutes using low-power microwave heating and the silver nanoparticle-modified SRR structures. The detectable concentration range for b-BSA was ~1 nM – 1 μM and ~0.01 nM – 1 μM for ELISA run at room temperature (HTS plates) and with microwave heating (SRR structures), respectively. A 100-fold improvement of the lower detection limit for b-BSA using SRR structures over HTS plates is observed.

Bibliography

1. J. Joannopoulos, S. Johnson, J. Winn, and R. Meade, *Photonic crystals: Molding the flow of light* (Princeton Univ Pr, 2008).

2. K. Sakoda, *Optical properties of photonic crystals* (Springer Verlag, 2005).

3. T. Krauss and R. De La Rue, "Photonic crystals in the optical regime--past, present and future," Progress in Quantum Electronics **23**, 51-96 (1999).

4. V. Agranovich and D. Mills, *Surface polaritons* (North-Holland, Amsterdam, 1982).

5. H. Raether, *Surface plasmons on smooth and rough surfaces and on gratings* (Springer-Verlag Berlin, 1988).

6. W. Barnes, A. Dereux, and T. Ebbesen, "Surface plasmon subwavelength optics," Nature **424**, 824-830 (2003).

7. H. Ditlbacher, B. Lamprecht, A. Leitner, and F. Aussenegg, "Spectrally coded optical data storage by metal nanoparticles," Optics Letters **25**, 563-565 (2000).

8. B. Rothenhaeusler and W. Knoll, "Surface–plasmon microscopy," (1988).

9. H. Atwater and A. Polman, "Plasmonics for improved photovoltaic devices," Nature Materials **9**, 205-213 (2010).

10. A. Haes and R. Van Duyne, "A unified view of propagating and localized surface plasmon resonance biosensors," Analytical and Bioanalytical Chemistry **379**, 920-930 (2004).

11. X. Zhang and Z. Liu, "Superlenses to overcome the diffraction limit," Nature Materials **7**, 435-441 (2008).

12. Z. W. Liu, H. Lee, Y. Xiong, C. Sun, and X. Zhang, "Far-field optical hyperlens magnifying sub-diffraction-limited objects," Science **315**, 1686-1686 (2007).

13. I. I. Smolyaninov, Y. J. Hung, and C. C. Davis, "Magnifying superlens in the visible frequency range," Science **315**, 1699-1701 (2007).

14. H. A. Bethe, "Theory of diffraction by small holes," Physical Review **66**, 163-182 (1944).

15. H. J. Lezec, A. Degiron, E. Devaux, R. A. Linke, L. Martin-Moreno, F. J. Garcia-Vidal, and T. W. Ebbesen, "Beaming light from a subwavelength aperture," Science **297**, 820-822 (2002).

16. H. Caglayan, I. Bulu, and E. Ozbay, "Beaming of electromagnetic waves emitted through a subwavelength annular aperture," Journal of the Optical Society of America B-Optical Physics **23**, 419-422 (2006).

17. F. Garcia-Vidal, L. Martin-Moreno, H. Lezec, and T. Ebbesen, "Focusing light with a single subwavelength aperture flanked by surface corrugations," Applied Physics Letters **83**, 4500 (2003).

18. S. S. Akarca-Biyikli, I. Bulu, and E. Ozbay, "Resonant excitation of surface plasmons in one-dimensional metallic grating structures at microwave frequencies," Journal of Optics a-Pure and Applied Optics **7**, S159-S164 (2005).

19. L. Yu, D. Lin, Y. Chen, Y. Chang, K. Huang, J. Liaw, J. Yeh, J. Liu, C. Yeh, and C. Lee, "Physical origin of directional beaming emitted from a subwavelength slit," Physical Review B **71**, 41405 (2005).

20. H. Caglayan, I. Bulu, and E. Ozbay, "Extraordinary grating-coupled microwave transmission through a subwavelength annular aperture," Optics Express **13**, 1666-1671 (2005).

21. L. Martin-Moreno, F. Garcia-Vidal, H. Lezec, A. Degiron, and T. Ebbesen, "Theory of highly directional emission from a single subwavelength aperture surrounded by surface corrugations," Physical Review Letters **90**, 167401 (2003).

22. E. Moreno, F. García-Vidal, and L. Martín-Moreno, "Enhanced transmission and beaming of light via photonic crystal surface modes," Physical Review B **69**, 121402 (2004).

23. I. Bulu, H. Caglayan, and E. Ozbay, "Beaming of light and enhanced transmission via surface modes of photonic crystals," Optics Letters **30**, 3078-3080 (2005).

24. P. Kramper, M. Agio, C. Soukoulis, A. Birner, F. Müller, R. Wehrspohn, U. Gösele, and V. Sandoghdar, "Highly directional emission from photonic crystal waveguides of subwavelength width," Physical Review Letters **92**, 113903 (2004).

25. S. Kim, H. Kim, Y. Lim, and B. Lee, "Off-axis directional beaming of optical field diffracted by a single subwavelength metal slit with asymmetric dielectric surface gratings," Applied Physics Letters **90**, 051113 (2007).

26. D. Lin, T. Cheng, C. Chang, J. Yeh, J. Liu, C. Yeh, and C. Lee, "Directional light beaming control by a subwavelength asymmetric surface structure," Opt. Express **15**, 2585-2591 (2007).

27. V. Agranovich and D. Mills, "Surface polaritons: Electromagnetic waves at surfaces and interfaces," Journal of the Optical Society of America B Optical Physics **1**, 410 (1984).

28. M. Brongersma and P. Kik, *Surface plasmon nanophotonics* (Springer Verlag, 2007).

29. J. Pendry, L. Martin-Moreno, and F. Garcia-Vidal, "Mimicking surface plasmons with structured surfaces," Science **305**, 847 (2004).

30. A. Hibbins, B. Evans, and J. Sambles, "Experimental verification of designer surface plasmons," Science **308**, 670 (2005).

31. T. W. Ebbesen, H. J. Lezec, H. F. Ghaemi, T. Thio, and P. A. Wolff, "Extraordinary optical transmission through sub-wavelength hole arrays," Nature **391**, 667-669 (1998).

32. H. Ghaemi, T. Thio, D. Grupp, T. Ebbesen, and H. Lezec, "Surface plasmons enhance optical transmission through subwavelength holes," Physical Review B **58**, 6779-6782 (1998).

33. L. Martin-Moreno, F. J. Garcia-Vidal, H. J. Lezec, K. M. Pellerin, T. Thio, J. B. Pendry, and T. W. Ebbesen, "Theory of extraordinary optical transmission

through subwavelength hole arrays," Physical Review Letters **86**, 1114-1117 (2001).

34. A. Degiron, H. Lezec, W. Barnes, and T. Ebbesen, "Effects of hole depth on enhanced light transmission through subwavelength hole arrays," Applied Physics Letters **81**, 4327 (2002).

35. C. Genet, M. Van Exter, and J. Woerdman, "Fano-type interpretation of red shifts and red tails in hole array transmission spectra," Optics Communications **225**, 331-336 (2003).

36. W. L. Barnes, W. A. Murray, J. Dintinger, E. Devaux, and T. W. Ebbesen, "Surface plasmon polaritons and their role in the enhanced transmission of light through periodic arrays of subwavelength holes in a metal film," Physical Review Letters **92**, 107401 (2004).

37. R. Gordon, A. G. Brolo, A. McKinnon, A. Rajora, B. Leathem, and K. L. Kavanagh, "Strong polarization in the optical transmission through elliptical nanohole arrays," Physical Review Letters **92**, 037401 (2004).

38. K. Koerkamp, S. Enoch, F. Segerink, N. Van Hulst, and L. Kuipers, "Strong influence of hole shape on extraordinary transmission through periodic arrays of subwavelength holes," Physical Review Letters **92**, 183901 (2004).

39. J. Gomez Rivas, C. Schotsch, P. Haring Bolivar, and H. Kurz, "Enhanced transmission of thz radiation through subwavelength holes," Physical Review B **68**, 201306 (2003).

40. M. Beruete, M. Sorolla, I. Campillo, J. Dolado, L. Martin-Moreno, J. Bravo-Abad, and F. Garcia-Vidal, "Enhanced millimeter-wave transmission through subwavelength hole arrays," Optics Letters **29**, 2500-2502 (2004).

41. A. Hibbins, J. Sambles, and C. Lawrence, "The coupling of microwave radiation to surface plasmon polaritons and guided modes via dielectric gratings," Journal of Applied Physics **87**, 2677 (2000).

42. M. Sigalas, C. Chan, K. Ho, and C. Soukoulis, "Metallic photonic band-gap materials," Physical Review B **52**, 11744-11751 (1995).

43. S. S. Akarca-Biyikli, I. Bulu, and E. Ozbay, "Enhanced transmission of microwave radiation in one-dimensional metallic gratings with subwavelength aperture," Applied Physics Letters **85**, 1098-1100 (2004).

44. K. Ohtaka, "Energy band of photons and low-energy photon diffraction," Physical Review B **19**, 5057-5067 (1979).

45. E. Yablonovitch, "Inhibited spontaneous emission in solid-state physics and electronics," Physics Review Letters **58**, 2059 (1987).

46. A. Yariv, Y. Xu, R. Lee, and A. Scherer, "Coupled-resonator optical waveguide: A proposal and analysis," Optics Letters **24**, 711-713 (1999).

47. N. Stefanou and A. Modinos, "Impurity bands in photonic insulators," Physical Review B **57**, 12127-12133 (1998).

48. Y. Lee, S. Kim, J. Huh, G. Kim, Y. Lee, S. Cho, Y. Kim, and Y. Do, "A high-extraction-efficiency nanopatterned organic light-emitting diode," Applied Physics Letters **82**, 3779 (2003).

49. R. Meade, K. Brommer, A. Rappe, and J. Joannopoulos, "Electromagnetic bloch waves at the surface of a photonic crystal," Physical Review B **44**, 10961-10964 (1991).

50. D. Beaglehole, "Coherent and incoherent radiation from optically excited surface plasmons on a metal grating," Physical Review Letters **22**, 708-711 (1969).

51. K. Ho, C. Chan, and C. Soukoulis, "Existence of a photonic gap in periodic dielectric structures," Physical Review Letters **65**, 3152-3155 (1990).

52. F. Ramos-Mendieta and P. Halevi, "Surface electromagnetic waves in two-dimensional photonic crystals: Effect of the position of the surface plane," Physical Review B **59**, 15112-15120 (1999).

53. W. Robertson, G. Arjavalingam, R. Meade, K. Brommer, A. Rappe, and J. Joannopoulos, "Observation of surface photons on periodic dielectric arrays," Optics Letters **18**, 528-530 (1993).

54. E. Yablonovitch, T. Gmitter, and K. Leung, "Photonic band structure: The face-centered-cubic case employing nonspherical atoms," Physical Review Letters **67**, 2295-2298 (1991).

55. S. John, "Strong localization of photons in certain disordered dielectric superlattices," Physical Review Letters **58**, 2486-2489 (1987).

56. B. Temelkuran, E. Ozbay, J. P. Kavanaugh, G. Tuttle, and K. M. Ho, "Resonant cavity enhanced detectors embedded in photonic crystals," Applied Physics Letters **72**, 2376-2378 (1998).

57. S. Morrison and Y. Kivshar, "Engineering of directional emission from photonic-crystal waveguides," Applied Physics Letters **86**, 081110 (2005).

58. H. Caglayan, I. Bulu, and E. Ozbay, "Off-axis directional beaming via photonic crystal surface modes," Applied Physics Letters **92**, 092114 (2008).

59. T. Baba and M. Nakamura, "Photonic crystal light deflection devices using the superprismeffect," Ieee Journal of Quantum Electronics **38**, 909-914 (2002).

60. T. Tamir and A. A. Oliner, "Guided complex waves, part i," Proceedings of the Institution of Electrical Engineers **110**, 310 (1963).

61. T. Tamir and A. A. Oliner, "Guided complex waves, part ii," Proceedings of the Institution of Electrical Engineers **110**, 325 (1963).

62. D. Jackson and A. Oliner, "Leaky-wave antennas," Antenna Engineering Handbook.

63. D. Sievenpiper, "Forward and backward leaky wave radiation with large effective aperture from an electronically tunable textured surface," IEEE transactions on antennas and propagation **53**, 236-247 (2005).

64. D. Sievenpiper, J. Schaffner, J. Lee, and S. Livingston, "A steerable leaky-wave antenna using a tunable impedance ground plane," IEEE Antennas and Wireless Propagation Letters **1**, 179-182 (2002).

65. L. Liu, C. Caloz, and T. Itoh, "Dominant mode leaky-wave antenna with backfire-to-endfire scanning capability," Electronics Letters **38**, 1414-1416 (2002).

66. D. Jackson, J. Chen, R. Qiang, F. Capolino, and A. Oliner, "The role of leaky plasmon waves in the directive beaming of light through a subwavelength aperture," Opt. Express **16**, 21271-21281 (2008).

67. I. Bulu, H. Caglayan, and E. Ozbay, "Radiation properties of sources inside photonic crystals," Physical Review B **67**, 205103 (2003).

68. I. Bulu, H. Caglayan, and E. Ozbay, "Highly directive radiation from sources embedded inside photonic crystals," Applied Physics Letters **83**, 3263-3265 (2003).

69. S. Foteinopoulou, M. Kafesaki, E. Economou, and C. Soukoulis, "Backward surface waves at photonic crystals," Physical Review B **75**, 245116 (2007).

70. Y. Lo and S. Lee, *Antenna handbook: Antenna fundamentals and mathematical techniques* (Kluwer Academic Publishers, 1993).

71. C. Balanis, "Antenna theory, hoboken," New Jersey: John Wiley & Sons, Inc **8**, 21-31 (2005).

72. T. Ueda, N. Michishita, A. Lai, and T. Itoh, "Leaky wave antenna based on evanescent-mode left-handed transmission lines composed of a cut-off parallel-plate waveguide loaded with dielectric resonators," IEICE Transactions on Electronics **90**, 1770-1775 (2007).

73. P. Villenevue, S. Fan, and J. Joannopoulos, "K.-y. Lim, gs petrich, la kolodziejski, and r. Reif," Appl. Phys. Lett **67**, 167 (1995).

74. P. Gourley, J. Wendt, G. Vawter, T. Brennan, and B. Hammons, "Optical properties of two dimensional photonic lattices fabricated as honeycomb nanostructures in compound semiconductors," Applied Physics Letters **64**, 687 (1994).

75. V. G. Veselago, "The electrodynamics of substances with simultaneously negative values of permittivity and permeability," Sov. Phys. Usp. **10**, 504-509 (1968).

76. J. B. Pendry, A. J. Holden, W. J. Stewart, and I. Youngs, "Extremely low frequency plasmons in metallic mesostructures," Physical Review Letters **76**, 4773-4776 (1996).

77. J. B. Pendry, A. J. Holden, D. J. Robbins, and W. J. Stewart, "Low frequency plasmons in thin-wire structures," Journal of Physics-Condensed Matter **10**, 4785-4809 (1998).

78. D. R. Smith, D. C. Vier, W. Padilla, S. C. Nemat-Nasser, and S. Schultz, "Loop-wire medium for investigating plasmons at microwave frequencies," Applied Physics Letters **75**, 1425-1427 (1999).

79. J. B. Pendry, A. J. Holden, D. J. Robbins, and W. J. Stewart, "Magnetism from conductors and enhanced nonlinear phenomena," Ieee Transactions on Microwave Theory and Techniques **47**, 2075-2084 (1999).

80. K. Guven, K. Aydin, and E. Ozbay, "Experimental analysis of true left-handed behaviour and transmission properties of composite metamaterials," Photonics and Nanostructures-Fundamentals and Applications **3**, 75-78 (2005).

81. X. D. Chen, T. M. Grzegorczyk, B. I. Wu, J. Pacheco, and J. A. Kong, "Robust method to retrieve the constitutive effective parameters of metamaterials," Physical Review E **70**, 016608 (2004).

82. X. Chen, B. I. Wu, J. A. Kong, and T. M. Grzegorczyk, "Retrieval of the effective constitutive parameters of bianisotropic metamaterials," Physical Review E **71**, 046610 (2005).

83. T. Koschny, M. Kafesaki, E. N. Economou, and C. M. Soukoulis, "Effective medium theory of left-handed materials," Physical Review Letters **93**, 107402 (2004).

84. T. Koschny, P. Markos, E. N. Economou, D. R. Smith, D. C. Vier, and C. M. Soukoulis, "Impact of inherent periodic structure on effective medium description of left-handed and related metamaterials," Physical Review B **71**, 245105 (2005).

85. T. Koschny, P. Markos, D. R. Smith, and C. M. Soukoulis, "Resonant and antiresonant frequency dependence of the effective parameters of metamaterials," Physical Review E **68**, 065602 (2003).

86. D. R. Smith, S. Schultz, P. Markos, and C. M. Soukoulis, "Determination of effective permittivity and permeability of metamaterials from reflection and transmission coefficients," Physical Review B **65**, 195104 (2002).

87. D. R. Smith, D. C. Vier, T. Koschny, and C. M. Soukoulis, "Electromagnetic parameter retrieval from inhomogeneous metamaterials," Physical Review E **71**, 036617 (2005).

88. K. Aydin and E. Ozbay, "Experimental investigation of reflection characteristics of left-handed metamaterials in free space," Iet Microwaves Antennas & Propagation **1**, 89-93 (2007).

89. E. Ozbay, K. Aydin, E. Cubukcu, and M. Bayindir, "Transmission and reflection properties of composite double negative metamaterials in free space," IEEE transactions on antennas and propagation **51**, 2592-2595 (2003).

90. A. Yariv and P. Yeh, "Photonics: Optical electronics in modern communications (the oxford series in electrical and computer engineering)," (2006).

91. P. Markoš and C. Soukoulis, "Transmission studies of left-handed materials," Physical Review B **65**, 33401 (2001).

92. D. Fredkin and A. Ron, "Effectively left-handed (negative index) composite material," Applied Physics Letters **81**, 1753 (2002).

93. C. Caloz and T. Itoh, *Electromagnetic metamaterials: Transmission line theory and microwave applications: The engineering approach* (Wiley-IEEE Press, 2006).

94. A. Ishimaru, *Electromagnetic wave propagation, radiation, and scattering* (Prentice Hall New Jersey, 1991).

95. M. Ünlü and S. Strite, "Resonant cavity enhanced photonic devices," Journal of Applied Physics **78**, 607 (1995).

96. E. Özbay and B. Temelkuran, "Reflection properties and defect formation in photonic crystals," Applied Physics Letters **69**, 743 (1996).

97. M. Antonoyiannakis and J. Pendry, "Electromagnetic forces in photonic crystals," Physical Review B **60**, 2363-2374 (1999).

98. C. Kittel, "Introduction to solid state physics. 1996," (John Wiley, New York).

99. N. Ashcroft and N. Mermin, "Solid state physics (saunders college, philadelphia, 1976)," International edn.

100. E. Lidorikis, M. Sigalas, E. Economou, and C. Soukoulis, "Tight-binding parametrization for photonic band gap materials," Physical Review Letters **81**, 1405-1408 (1998).

101. T. Mukaiyama, K. Takeda, H. Miyazaki, Y. Jimba, and M. Kuwata-Gonokami, "Tight-binding photonic molecule modes of resonant bispheres," Physical Review Letters **82**, 4623-4626 (1999).

102. M. Bayindir, B. Temelkuran, and E. Ozbay, "Tight-binding description of the coupled defect modes in three-dimensional photonic crystals," Physical Review Letters **84**, 2140-2143 (2000).

103. M. Bayindir, C. Kural, and E. Ozbay, "Coupled optical microcavities in one-dimensional photonic bandgap structures," Journal of Optics a-Pure and Applied Optics **3**, S184-S189 (2001).

104. J. B. Pendry, A. J. Holden, D. J. Robbins, and J. W. Stewart, "Magnetism from conductors and enhanced nonlinear phenomena," IEEE Transactions on Microwave Theory and Techniques **47**, 2075-2084 (1999).

105. D. R. Smith, W. J. Padilla, D. C. Vier, S. C. Nemat-Nasser, and S. Schultz, "Composite medium with simultaneously negative permeability and permittivity," Physical Review Letters **84**, 4184 (2000).

106. R. A. Shelby, D. R. Smith, and S. Schultz, "Experimental verification of a negative index of refraction " Science **291**, 77 (2001).

107. K. Aydin, K. Guven, C. M. Soukoulis, and E. Ozbay, "Observation of negative refraction and negative phase velocity in left-handed metamaterials," Applied Physics Letters **86**, 124102 (2005).

108. Y. Hsu, Y. Huang, J. Lih, and J. Chern, "Electromagnetic resonance in deformed split ring resonators of left-handed meta-materials," Journal of Applied Physics **96**, 1979 (2004).

109. K. Aydin, I. Bulu, K. Guven, M. Kafesaki, C. Soukoulis, and E. Ozbay, "Investigation of magnetic resonances for different split-ring resonator parameters and designs," New Journal of Physics **7**, 168 (2005).

110. N. Katsarakis, T. Koschny, M. Kafesaki, E. Economou, and C. Soukoulis, "Electric coupling to the magnetic resonance of split ring resonators," Applied Physics Letters **84**, 2943 (2004).

111. K. Aydin, K. Guven, N. Katsarakis, C. Soukoulis, and E. Ozbay, "Effect of disorder on magnetic resonance band gap of split-ring resonator structures," Opt. Express **12**, 5896-5901 (2004).

112. D. Smith, J. Gollub, J. Mock, W. Padilla, and D. Schurig, "Calculation and measurement of bianisotropy in a split ring resonator metamaterial," Journal of Applied Physics **100**, 024507 (2006).

113. F. Qureshi, M. Antoniades, and G. Eleftheriades, "A compact and low-profile metamaterial ring antenna with vertical polarization," IEEE Antennas and Wireless Propagation Letters **4**, 333-336 (2005).

114. S. Hrabar, J. Bartolic, and Z. Sipus, "Waveguide miniaturization using uniaxial negative permeability metamaterial," IEEE transactions on antennas and propagation **53**, 110-119 (2005).

115. K. Buell, H. Mosallaei, and K. Sarabandi, "A substrate for small patch antennas providing tunable miniaturization factors," IEEE transactions on antennas and propagation **54**, 135-146 (2006).

116. K. Alici and E. Ozbay, "Electrically small split ring resonator antennas," Journal of Applied Physics **101**, 083104 (2007).

117. B. Wu, W. Wang, J. Pacheco, X. Chen, J. Lu, T. Grzegorczyk, J. Kong, P. Kao, P. Theophelakes, and M. Hogan, "Anisotropic metamaterials as antenna substrate to enhance directivity," J Comput Phys **181**, 186-221 (2002).

118. I. Bulu, H. Caglayan, K. Aydin, and E. Ozbay, "Compact size highly directive antennas based on the srr metamaterial medium," New Journal of Physics **7**, 223 (2005).

119. K. Aslan and C. D. Geddes, "Microwave-accelerated metal-enhanced fluorescence: Platform technology for ultrafast and ultrabright assays," Analytical Chemistry **77**, 8057-8067 (2005).

120. K. Aslan and C. D. Geddes, "New tools for rapid clinical and bioagent diagnostics: Microwaves and plasmonic nanostructures," Analyst **133**, 1469-1480 (2008).

121. K. Aslan, I. Gryczynski, J. Malicka, E. Matveeva, J. R. Lakowicz, and C. D. Geddes, "Metal-enhanced fluorescence: An emerging tool in biotechnology," Current Opinion in Biotechnology **16**, 55-62 (2005).

122. M. J. R. Previte, K. Aslan, and C. D. Geddes, "Spatial and temporal control of microwave triggered chemiluminescence: A protein detection platform," Analytical Chemistry **79**, 7042-7052 (2007).

123. K. Aslan, M. J. Previte, Y. Zhang, T. Gallagher, L. Baillie, and C. D. Geddes, "Extraction and detection of DNA from bacillus anthracis spores and the vegetative cells within 1 min," Anal Chem **80**, 4125-4132 (2008).

124. H. Caglayan and E. Ozbay, "Surface wave splitter based on metallic gratings with sub-wavelength aperture," Optics Express **16**, 19091-19096 (2008).

125. K. Aydin, K. Guven, N. Katsarakis, C. M. Soukoulis, and E. Ozbay, "Effect of disorder on magnetic resonance band gap of split-ring resonator structures," Optics Express **12**, 5896-5901 (2004).

126. A. B. Movchan and S. Guenneau, "Split-ring resonators and localized modes," Physical Review B **70**, - (2004).

127. T. Koschny, P. Markos, D. R. Smith, and C. M. Soukoulis, "Resonant and antiresonant frequency dependence of the effective parameters of metamaterials," Physical Review E **68**, - (2003).

128. K. Aslan and C. D. Geddes, "Microwave-accelerated ultrafast nanoparticle aggregation assays using gold colloids," Anal Chem **79**, 2131-2136 (2007).

129. M. J. Previte, K. Aslan, S. N. Malyn, and C. D. Geddes, "Microwave triggered metal enhanced chemiluminescence: Quantitative protein determination," Anal Chem **78**, 8020-8027 (2006).

Appendix A

Publications in SCI Journals

1. Irfan Bulu, Humeyra Caglayan, and Ekmel Ozbay, "Radiation properties of sources inside photonic crystals," Physical Review B **67**, 205103 (2003).
2. Irfan Bulu, Humeyra Caglayan, and Ekmel Ozbay, "Highly directive radiation from sources embedded inside photonic crystals," Applied Physics Letters **83**, 3263 (2003).
3. (INVITED) Ekmel Ozbay, Irfan Bulu, Koray Aydin, Humeyra Caglayan, and Kaan Guven "Physics and applications of photonic crystals," Photonics and Nanostructures **2**, 87 (2004).
4. Ekmel Ozbay, Irfan Bulu, Koray Aydin, Humeyra Caglayan, K. Bora Alici, and Kaan Guven, "Highly Directive Radiation and Negative Refraction Using Photonic Crystals," Laser Physics Journal **15**, 217 (2005).
5. Humeyra Caglayan, Irfan Bulu, and Ekmel Ozbay "Extraordinary grating-coupled microwave transmission through a subwavelength annular aperture," Optics Express **13**, 1666 (2005).
6. Irfan Bulu, Humeyra Caglayan, and Ekmel Ozbay, "Negative refraction and focusing of electromagnetic waves by metallodielectric photonic crystals," Physical Review B **71**, 045124 (2005).
7. Humeyra Caglayan, Irfan Bulu, and Ekmel Ozbay "Highly directional enhanced radiation from sources embedded inside three-dimensional photonic crystals," Optics Express **13**, 7645 (2005).

8. Irfan Bulu, Humeyra Caglayan, and Ekmel Ozbay, "Beaming of Light and Enhanced Transmission via Surface Modes of Photonic Crystals," Optics Letters 30, 3078 (2005).
9. Irfan Bulu, Humeyra Caglayan, Koray Aydin and Ekmel Ozbay "Compact size highly directive antennas based on the SRR metamaterial medium," New Journal of Physics **7**, 223 (2005).
10. Irfan Bulu, Humeyra Caglayan, and Ekmel Ozbay, "Experimental demonstration of labyrinth-based left-handed metamaterials," Optics Express **13**, 10238 (2005).
11. Humeyra Caglayan, Irfan Bulu, and Ekmel Ozbay, "Beaming of electromagnetic waves emitted through a subwavelength annular aperture," Journal of Optical Society of America B **23**, 419 (2006).
12. Irfan Bulu, Humeyra Caglayan, and Ekmel Ozbay, "Experimental demonstration of subwavelength focusing of electromagnetic waves by labyrinth-based two-dimensional metamaterials," Optics Letters **31**, 814 (2006).
13. (INVITED) Ekmel Ozbay, Irfan Bulu, Kaan Guven, Humeyra Caglayan, and Koray Aydin, "Observation of Negative Refraction and Focusing in Two-Dimensional Photonic Crystals," Japanese Journal of Applied Physics **45**, 6064 (2006).
14. Humeyra Caglayan, Irfan Bulu, and Ekmel Ozbay, "Plasmonic structures with extraordinary transmission and highly directional beaming properties," IEEE Microwave and Optical Technology Letters **48**, 2491(2006).
15. Irfan Bulu, Humeyra Caglayan, and Ekmel Ozbay, "Designing materials with desired electromagnetic properties," IEEE Microwave and Optical Technology Letters **48**, 2611(2006).

16. Ekmel Ozbay, Irfan Bulu, and Humeyra Caglayan, "Transmission, refraction, and focusing properties of labyrinth based left-handed metamaterials," Physica Status Solidi B **244**, 1202 (2007).
17. Irfan Bulu, Humeyra Caglayan, Koray Aydin, and E. Ozbay "Study of the field emitted by a source placed inside a two-dimensional left-handed metamaterial," Optics Letters **32**, 850 (2007).
18. Zhaofeng Li, Humeyra Caglayan, Evrim Colak, and Ekmel Ozbay "Enhanced transmission and directivity from metallic subwavelength apertures with nonuniform and nonperiodic grooves," Applied Physics Letters **92**, 011128 (2008).
19. Humeyra Caglayan, Irfan Bulu, and Ekmel Ozbay "Focusing surface plasmons via changing the incident angle," Journal of Applied Physics **103**, 053105 (2008).
20. Humeyra Caglayan, Irfan Bulu, and Ekmel Ozbay "Off-axis directional beaming via photonic crystal surface modes," Applied Physics Letters **92**, 092114 (2008).
21. Humeyra Caglayan, Irfan Bulu, Marko Loncar, and Ekmel Ozbay "Experimental observation of cavity formation in composite metamaterials," Optics Express **16**, 11132 (2008).
22. Humeyra Caglayan, Irfan Bulu, Marko Loncar, and Ekmel Ozbay, "Observation of Coupled Cavity Structures in Metamaterials," Applied Physics Letters **93**,121910 (2008).
23. Humeyra Caglayan, Irfan Bulu, and Ekmel Ozbay, "Off-axis beaming from subwavelength apertures," Journal of Applied Physics **104**, 073108 (2008).
24. Humeyra Caglayan and Ekmel Ozbay, "Surface wave splitter based on metallic gratings with sub-wavelength aperture," Optics Express **16**, 19091–19096 (2008).

25. Hamza Kurt, Evrim Colak, Ozgur Cakmak, Humeyra Caglayan, and Ekmel Ozbay, "The focusing effect of graded index photonic crystals," Applied Physics Letters **93**, 171108 (2008).
26. Humeyra Caglayan, Irfan Bulu, Marko Loncar, and Ekmel Ozbay, "Cavity formation in Split Ring Resonators," Photonics and Nanostructures – Fundamentals and Applications **6**, 200–204 (2008).
27. Humeyra Caglayan, Irfan Bulu, Marko Loncar, and Ekmel Ozbay, "Experimental Observation of Subwavelength Localization Using Metamaterial Based Cavities," Optics Letters **34**, 88 (2009)
28. Humeyra Caglayan, Irfan Bulu, and Ekmel Ozbay, "Observation of off-axis directional beaming via subwavelength asymmetric metallic gratings," Journal of Physics D **42**, 045105 (2009)
29. Zhaofeng Li, Kamil Boratay Alici, Humeyra Caglayan and Ekmel Ozbay "Generation of an Axially Asymmetric Bessel-Like Beam from a Metallic Subwavelength Aperture," Physics Review Letters **92**, 011128 (2008).
30. Atilla Ozgur Cakmak, Evrim Colak, Humeyra Caglayan, Hamza Kurt, and Ekmel Ozbay "High efficiency of graded index photonic crystal as an input coupler," Journal of Applied Physics **105**, 103708 (2009).
31. Evrim Colak, Humeyra Caglayan, Atilla Ozgur Cakmak, Alessandro Della Villa, Filippo Capolino, and Ekmel Ozbay "Frequency dependent steering with backward leaky waves via photonic crystal interface layer," Optics Express **17**, 9879 -9890 (2009).
32. Zhaofeng Li, Humeyra Caglayan, Evrim Colak, Jiangfeng Zhou, Costas M. Soukoulis, and Ekmel Ozbay, "Coupling effect between two adjacent chiral structure layers," Optics Express **18**, 5375 -5383 (2010).
33. Humeyra Caglayan and Ekmel Ozbay, "Observation of Cavity Structures in Left-Handed Metamaterials" accepted to *Journal of Nano Photonics*
34. Zhaofeng Li, Rongkuo Zhao, Thomas Koschny, Evrim Colak, Humeyra Caglayan, Ekmel Ozbay and C. M. Soukoulis, "Chiral metamaterials with

negative refractive index based on Four-U-SRRs resonators" accepted to *Applied Physics Letters*

35. Semih Cakmakyapan, Humeyra Caglayan, Andriy Serebryannikov, and Ekmel Ozbay, "One-way transmission through the subwavelength slit in non-symmetric metallic gratings" submitted to *Optics Letters*
36. Sarah A. Addae, Melissa A. Pinard, Humeyra Caglayan, Semih Cakmakyapan, Deniz Caliskan, Ekmel Ozbay, and Kadir Aslan, "Rapid and Sensitive Colorimetric ELISA using Silver Nanoparticles, Microwaves and Split Ring Resonator Structures" submitted to *Analytical Chemistry*
37. Humeyra Caglayan, Semih Cakmakyapan, Sarah A. Addae, Melissa A. Pinard, Deniz Caliskan, Kadir Aslan, and Ekmel Ozbay, "Ultrafast and and sensitive bioassay using SRR structures and microwave heating" submitted to *Applied Physics Letters*